ON STANDING WAVES AND MODELS OF SHEAR DISPERSION

by

Geoffry Norman Mercer, B.Sc.(Hons.) (Maths.Sc.)

Thesis submitted for the degree of
Doctor of Philosophy
in the Department of Applied Mathematics,
University of Adelaide,

May 1992.

CONTENTS

SUMMARY

This thesis is concerned with two topics; standing waves on water of finite and infinite depth and models of shear dispersion in channels and pipes.

In the first part standing waves are considered. A stable and accurate numerical method for the calculation of the motion of an interface between two fluids is used to calculate two-dimensional standing waves on deep water. Extremely steep standing waves are determined, significantly steeper than has been previously reported. The peak crest acceleration is used as the determining parameter rather than the wave steepness as the wave steepness is found to have a maximum short of the most extreme wave. Profiles with crest accelerations up to 99% of gravity are calculated and the shape of these extreme standing wave profiles are discussed.

The method is extended to water of finite depth and standing waves are calculated. The effect of the harmonic resonances on the standing waves are investigated and some properties of finite depth standing waves are presented.

The stability of the standing waves on deep water is examined and growth rates of the unstable modes are calculated. It is found that all but very steep standing waves are generally stable to harmonic perturbations. However, standing waves in deep water are typically unstable to subharmonic perturbations via a side-band type instability.

In the second part of this thesis shear dispersion in channels and pipes is considered. High order models of the longitudinal dispersion of a passive contaminant in Poiseuille channel flow and Poiseuille pipe flow are derived and their validity discussed. The derivation is done using centre manifold theory which provides a systematic and consistent approach to calculating each successive approximation. For the case of channel flow, models are also derived when the cross–section, flux and diffusivity all vary; the resultant modifications to the advection velocity and the effective dispersion coefficient are calculated.

In the case of pipe flow, a stable, non–negative finite difference scheme is

formulated which matches the evolution equation to a predetermined order. The limitations imposed by this matching is investigated. The appropriate initial condition to use for the Taylor model of shear dispersion in pipes is derived. It is shown that the commonly used initial condition of simply taking the cross–sectional average is only a first approximation to the correct initial condition. In a similar manner the correct boundary conditions to be used at the inlet and outlet of a finite length pipe are derived. The modifications of the Taylor model to use for a pipe with varying cross–section and varying flow properties is also studied.

SIGNED STATEMENT

This thesis contains no material which has been accepted for the award of any other degree or diploma in any University.

To the best of my knowledge and belief, this thesis contains no material previously published or written by another person, except where due reference is made in the text of the thesis.

I consent to this thesis being made available for photocopying and loan.

Geoffry Norman Mercer

ACKNOWLEDGEMENTS

I would like to express my deepest thanks to my supervisor Dr. A. J. Roberts, Department of Applied Mathematics, University of Adelaide for his guidance and encouragement throughout the duration of my Ph.D. candidature.

PART ONE

STANDING WATER WAVES

CHAPTER 1
INTRODUCTION

In this part a stable and accurate numerical method to calculate the motion of an interface between two fluids is used to calculate two-dimensional standing waves on both finite and infinite depth water. Extremely steep standing waves are determined, significantly steeper than has been previously reported. The stability of the standing waves is examined and growth rates of the unstable modes are calculated. The majority of the work presented here has been published in Mercer and Roberts (1992a). Extensions to the published work include calculations to a higher crest acceleration using $N = 256$ mesh points and the calculation of standing waves on water of a finite depth.

Two-dimensional standing waves at an interface of two fluids of different densities are defined to be fluid motions that are periodic in both space and time. It is this time dependence that makes the mathematical analysis of standing waves more difficult than that of steady wave motion. To date there is no formal proof of the existence of standing waves although there are approximate solutions for standing waves of small amplitude. The work of Amick and Toland (1987) has gone some way towards a formal proof but more work needs to be done in this area. Standing waves occur in many physical situations. Reflection of a progressive wave will result in standing waves near the reflecting object. This is important in applications such as standing waves at sea walls or at moored structures such as oil platforms. Standing waves can also occur in confined areas such as mixing tanks or road tankers where the sloshing of fluid can result in standing waves. Furthermore, standing waves are a proto-type of complex time–dependent free–surface flows, and their simulation provides valuable experience for the simulation of directly relevant time–dependent free–surface dynamics. It is therefore important to be able to accurately calculate standing waves.

In contrast to the progressive wave case the limiting profile for standing

waves is not understood in any detail. Here I calculate standing wave profiles which appear to be close to the limiting case and show that the profiles are of a different shape than previously conjectured. The numerical approach is to directly simulate the dynamics of standing waves and consequently it is also easy to investigate the stability of the calculated waves.

Standing waves in deep water were first studied by Rayleigh (1915) who calculated a perturbation series to third order using the wave amplitude as the small parameter. Penny and Price (1952) generalised this perturbation series approach to fifth order. They noted that at no time is the interface ever flat. Saffman and Yuen (1979) used a numerical method to investigate standing waves although the waves they studied were not pure standing waves as they did not repeat exactly. Aoki (1980) extended the perturbation series of Penny and Price to eighth order correcting their algebraic error in the fifth order calculation. Schwartz and Whitney (1981) used a conformal mapping method to simplify the perturbation series which they then calculated to 25^{th} order for the infinite depth case. Rottman (1982) calculated high order perturbation series solutions for the infinite depth case allowing for different density ratios between the upper and lower fluids. Considerably less work has been done for the case of standing waves on an interface where either fluid is of a finite depth. Tabjbakhsh and Keller (1960) calculated a perturbation series to third order for free–surface standing waves in water of finite depth. This work was generalised by Concus (1962) to include the effects of surface tension. Goda (1967) extended the work of Tabjbakhsh and Keller to fourth order and calculated the pressure field due to the standing waves. More recently, Vanden-Broeck and Schwartz (1981) devised a numerical scheme for the calculation of standing waves. Their method consists of truncating an infinite series for the surface elevation and velocity potential and then using a collocation method to obtain a system of nonlinear algebraic equations which can be solved using Newton's method. This method was used for both the finite and infinite depth cases

but is inadequate for extreme waves due to the slow decay of the series coefficients. A similar method was used by Tsai and Yue (1987) to calculate standing waves in a circular basin. Marchant and Roberts (1987) calculated a perturbation series to 35^{th} order for finite depth short-crested waves of which standing waves are a limiting case.

Presented here is a stable and accurate numerical method for the calculation of standing waves on the interface between two fluids of different densities. This method is based on the semi-Lagrangian approach which has been used for periodic waves by Longuet-Higgins and Cokelet (1976). Vinge and Brevig (1981) and Baker, Merion and Orszag (1982) have also developed algorithms to numerically calculate free–surface flows. Pullin (1982) used a similar algorithm to investigate some of the instabilities that occur on an interface. More recently similar boundary–integral methods have been extensively used in the calculation of many different surface flow problems, for example the flow in front of and behind a moving barge, Davidson (1990).

This part of the thesis is organised as follows. Chapter 2 deals with standing waves on deep water. The problem is formulated and the numerical scheme described in detail. The results of the numerical method are presented and discussed with particular emphasis on extreme standing waves. A generalisation of this to standing waves on water of finite depth is given in Chapter 3. A method for determining the stability of standing waves is presented in Chapter 4 and the stability of standing waves in infinite depth water to harmonic and subharmonic perturbations are calculated.

Throughout this thesis figures are located at the end of each chapter for ease of reference.

CHAPTER 2

EXTREME STANDING WAVES ON DEEP WATER

2.1 A formulation of interfacial motion

2.1.1 Derivation of equations

I consider the general two-dimensional motion, under the influence of gravity, of a sharp interface between two fluids of different densities. All quantities relating to the upper or lower fluid are denoted by the subscripts 2 and 1 respectively. Both fluids are assumed to be inviscid and incompressible and the motion in each fluid is assumed to be irrotational. Both fluids are considered to be confined in the horizontal by two vertical plates and to extend indefinitely in the vertical. See Figure 2.1 for a schematic diagram of the interface.

Define Cartesian coordinates such that the x-axis is along the undisturbed interface and the y-axis is perpendicular to the undisturbed interface and in the opposite direction to gravity. Following Roberts (1983a) I non-dimensionalise by scaling quantities with respect to the reference length $L/2\pi$, the reference time $g(2\pi/L)\sqrt{(\rho_1-\rho_2)/(\rho_1+\rho_2)}$ and the reference density ρ_1. The lower fluid therefore has a scaled density of unity and I denote the scaled density of the upper fluid (ρ_2/ρ_1) by ρ. Interfacial tension may be included in the formalism but this will not be done here. The analysis is initially carried out for arbitrary ρ in the range $0 \leq \rho < 1$, but for clarity and comparison with previous results all the results presented here will use the value of ρ which is appropriate for a free surface (that is $\rho = 0$). Preliminary tests have shown that there is no visible difference in the profiles for the air-water case ($\rho = 0.001$) and the free surface case ($\rho = 0$), the maximum difference being less than 0.1%. The effect of variations in ρ and surface tension are areas of possible future research.

The numerical method I employ is that described by Roberts (1983a) for periodic two–dimensional motion of an interface between two inviscid, irrotational, incompressible and infinitely deep fluids, with modifications for the standing wave

configuration. I will therefore use a similar notation to Roberts (1983a). Begin by defining the operator

$$\frac{D}{Dt} = \frac{\partial}{\partial t} + \mathbf{q}_1 \cdot \nabla, \tag{2.1.1}$$

which gives the derivative following the motion of a particle of the lower fluid, where $\mathbf{q}_1$ is the velocity in the lower fluid. On the interface we could follow an arbitrary combination of the velocities of the upper and lower fluids but it is shown in Roberts (1983a) that the algorithm is generally made numerically stable if a particle in either fluid is followed but not a combination of both. This choice, properly implemented, removes the need for error inducing smoothing techniques as has been used in some numerical methods, see Longuet-Higgins and Cokelet (1976) for example. Represent the interface parametrically by $(X(j,t), Y(j,t))$ where the wave is periodic in j with period N (later j will be chosen to be integral in the discretisation) then, as it is required that the interface follows the motion of the particles of the lower fluid on the interface, I obtain

$$\frac{\partial X}{\partial t} = \frac{Dx}{Dt} = u_1 \quad \text{and} \quad \frac{\partial Y}{\partial t} = \frac{Dy}{Dt} = v_1 \quad \text{on} \quad S(t), \tag{2.1.2}$$

where

$$(u_1, v_1) = \mathbf{q}_1, \tag{2.1.3}$$

and $S(t)$ denotes the interface. The motion is assumed irrotational so the velocities can be expressed in terms of velocity potentials ϕ_1 and ϕ_2 for the lower and upper fluid respectively. The two fluids do not cross or separate which gives the constraint

$$\frac{\partial \phi_1}{\partial n} = \frac{\partial \phi_2}{\partial n} \quad \text{on} \quad S(t), \tag{2.1.4}$$

where n is a measure of distance normal to the interface. In the absence of surface tension, continuity in the pressure across the interface gives

$$p_2 = p_1, \tag{2.1.5}$$

where p_1 and p_2 are the pressures given by Bernoulli's Equation as

$$\begin{aligned} p_1 &= -\frac{\partial \phi_1}{\partial t} - \left(\frac{1+\rho}{1-\rho}\right) y - \frac{1}{2}\mathbf{q}_1^2 \\ p_2 &= -\frac{\partial \phi_2}{\partial t} - \left(\frac{1+\rho}{1-\rho}\right) y - \frac{1}{2}\mathbf{q}_2^2, \end{aligned} \tag{2.1.6}$$

in the lower and upper fluids respectively, where $\mathbf{q}_2$ is the velocity in the upper fluid. Define

$$\phi(j,t) = \phi_1 - \rho\phi_2 \quad \text{on} \quad S(t), \tag{2.1.7}$$

use (2.1.6) to rearrange (2.1.5) and obtain

$$\frac{\partial \phi}{\partial t} = -(1+\rho)Y + \frac{1}{2}\mathbf{q}_1^2 + \frac{1}{2}\mathbf{q}_2^2 - \rho\mathbf{q}_1 \cdot \mathbf{q}_2. \tag{2.1.8}$$

Equations (2.1.2) and (2.1.8) are formulae for calculating the time derivatives of $X(j,t)$, $Y(j,t)$ and $\phi(j,t)$ from their values and the velocities of the fluids at the interface. The remaining task is to find the velocities at the interface given values for X, Y and ϕ.

Define the complex potential $f(z)$ in the upper and lower fluid such that ϕ_1 and ϕ_2 are the real part of $f(z)$ in their respective domains. The function $f(z)$ is defined by a distribution of vortices on the interface. The vorticity strength per unit j is to be given by a_j and so using the periodicity of the motion the velocity of the fluids can be written as

$$\frac{\partial f}{\partial z} = u - iv = \frac{-i}{4\pi}\int_0^N a_j \cot\left(\frac{z - Z_j}{2}\right) dj, \tag{2.1.9}$$

where $Z_j = X_j + iY_j$. Let z tend to Z_k from the upper or lower fluid and obtain that the velocities at the interface are

$$\left(\frac{\partial f}{\partial z}\right)_k = \frac{-i}{4\pi}\fint_0^N a_j \cot\left(\frac{Z_k - Z_j}{2}\right) dj \mp \frac{a_k}{2Z_k'}, \tag{2.1.10}$$

where this integral is a Cauchy principle value integral, the negative alternative gives the upper fluid's velocity and the positive the lower fluid's velocity and where $'$ is defined as $\frac{\partial}{\partial j}$.

Calculating $\frac{\partial f}{\partial j}$ via the chain rule and taking the real part gives an equation involving ϕ', namely

$$\phi'_k = \frac{1}{2}(1+\rho)a_k + \frac{1-\rho}{4\pi}\int_0^N a_j \Im\left\{Z'_k \cot\left(\frac{Z_k - Z_j}{2}\right)\right\} dj. \qquad (2.1.11)$$

This is an integral equation for the vortex strength a_j given values of ϕ_j, X_j and Y_j at any time. Once this is solved (2.1.10) can be used to calculate the velocities of the fluid and then the time rate of change of X_j, Y_j and ϕ_j can be calculated from equations (2.1.2) and (2.1.8).

2.1.2 Integral invariants

There are several integral properties of the flow that should remain invariant with time provided the interface $S(t)$ remains intact; for instance the completion of wave breaking is excluded. These integral invariants prove to be a very useful check on the numerical procedure. I shall use the results given by Roberts (1983a) for the kinetic energy $T(t)$ and gravitational potential energy $V(t)$. The total energy, the sum of these energies is a conserved quantity. Also the mean vertical position of the interface must be invariant, and should in fact be zero from the definition of the reference axes. Also defined in Roberts (1983a) is the average volume flux across the interface which should be zero.

2.2 The numerical method

2.2.1 Outline

There are essentially three parts to calculating standing wave profiles. The first is to calculate the time derivatives of X_j, Y_j and ϕ_j at discrete points given their values at any time, the second is to integrate these quantities forward in time, and the third is to find a profile that replicates itself after an unknown period τ and hence is a standing wave profile. I consider the time integration of a finite set of ordinary differential equations to be a solved problem and so use either the NAG routine D02CAF, which uses a variable-order variable-step Adams method to integrate forward in time, or a Runge-Kutta method which was found to perform

more reliably for the near extreme waves.

2.2.2 Time and space derivatives

The first problem is then to accurately calculate the time derivatives given in equations (2.1.2) and (2.1.8). The method of images is used to enforce the boundary conditions on the vertical plates and the periodic extension of figure 2.1. The interface is discretised by defining N mesh points per wavelength on the interface, at integral values of j, and representing all functions by their values at these mesh points. To calculate the time derivatives one must first evaluate the integrals given in (2.1.10) and (2.1.11). These integrals are all periodic and hence they can be accurately calculated (with an error which decreases exponentially in N) by simply summing the values of the integrand at the mesh points. The integrand of the integral in (2.1.10) is singular at the point $j = k$. As described in Roberts (1983a) this singularity can be removed by subtracting an integral which has a value of zero and exactly the same singularity. Doing this I find the integrand of this integral takes the value

$$\frac{Z_k'' a_k}{Z_k'^2} - \frac{2a_k'}{Z_k'} \quad \text{at} \quad j = k. \tag{2.2.1}$$

At first glance the integrand of the integral in (2.1.11) appears to be singular as well, but it can be shown that

$$\Im\left\{Z_k' \cot\left(\frac{Z_k - Z_j}{2}\right)\right\} \to \Im\left\{\frac{Z_k''}{Z_k'}\right\} \quad \text{as} \quad j \to k, \tag{2.2.2}$$

and hence this integral is non-singular and is easily calculated.

Accurate spatial derivatives of all quantities are obtained by taking the finite Fourier transform of the quantities, differentiating this and then inverting the Fourier transform. This is possible as all quantities are periodic plus, in some instances, a known linear part which can be subtracted off before taking the transform and then compensated for after the inversion. Throughout this problem N is chosen as a power of 2 and hence fast Fourier transforms can be used, this

substantially reduces the computational effort required to calculate the spatial derivatives.

The above describes a numerical scheme which enables the integration forward in time of any given spatially periodic interfacial wave profile between two fluids. This has many applications some of which include wave breaking and the calculation of progressive interfacial waves of permanent form, see Roberts (1983a).

2.2.3 Standing wave configuration

Due to the symmetry of standing wave profiles I insist that the interface be symmetric about the vertical lines $x = n\pi$, where n is an integer. This symmetry enables the number of mesh points to be reduced from N to $\frac{N}{2}+1$ since $\frac{N}{2}-1$ mesh points and their function values are obtained by reflection in the line $x = \pi$. The mesh points are chosen so that mesh points lie on the lines $x = 0$ and $x = \pi$.

Rewriting the integral in equation (2.1.10) as a sum (as described above) and allowing for the symmetry I obtain equations for the velocity of the lower fluid at the interface at each mesh point

$$\begin{aligned}(u_1 - iv_1)_k = \frac{-i}{4\pi}\sum_{j=0,j\neq k}^{\frac{N}{2}+1} a_j \cot\left(\frac{Z_k - Z_j}{2}\right) + \frac{i}{4\pi}\sum_{j=1}^{\frac{N}{2}} a_j \cot\left(\frac{Z_k + \overline{Z_j}}{2}\right) \\ + \frac{a_k}{2Z'_k} + \frac{Z''_k a_k}{Z'^2_k} - \frac{2a'_k}{Z'_k}.\end{aligned} \tag{2.2.3}$$

Performing a similar analysis on equation (2.1.11) to obtain an equation involving ϕ' and a_j, namely

$$\begin{aligned}\phi'_k = \frac{1}{2}(1+\rho)a_k + \frac{1-\rho}{4\pi}\sum_{j=0,j\neq k}^{\frac{N}{2}+1} a_j \Im\left\{Z'_k \cot\left(\frac{Z_k - Z_j}{2}\right)\right\} \\ - \frac{1-\rho}{4\pi}\sum_{j=1}^{\frac{N}{2}} a_j \Im\left\{Z'_k \cot\left(\frac{Z_k + \overline{Z_j}}{2}\right)\right\} + \frac{1-\rho}{4\pi}\Im\left\{\frac{Z''_k}{Z'_k}\right\}.\end{aligned} \tag{2.2.4}$$

The numerical scheme consists of solving (2.2.4) for the a_j's then finding the fluid velocities at the interface at each mesh point from (2.2.3) and the time derivatives of the potential function from (2.1.8). It is therefore possible to integrate forward

in time any given interfacial profile which is bounded by walls at $x = 0$ and $x = \pi$, and hence ascertain how it evolves. This has applications to the sloshing of fluids in tanks and containers which is an area for subsequent research.

The problem of standing waves is to calculate a profile which replicates itself after an unknown period τ; two approaches were used. The first was to fix the fluid to be stationary at time $t = 0$ and then half a period later, $t = \tau/2$, the fluid must be stationary again. This gives us $\frac{N}{2} + 1$ equations

$$\phi_j(\tau/2) = 0 \quad , \quad j = 1, \ldots, \frac{N}{2} + 1, \tag{2.2.5}$$

to be solved for the $\frac{N}{2} + 2$ unknowns $Y_1, \ldots, Y_{\frac{N}{2}+1}$ and period τ. This approach could conceivably give rise to an asymmetric solution, one where the profile at the half–period is not the mirror image of the initial; however this was never observed to happen. The second approach was to start with a stationary profile and integrate for a quarter period, $t = \tau/4$, and insist that the profile then be symmetric (about $x = \pi/2$) and the velocity profile be asymmetric. This approach was: more efficient as I only integrated for half the time; ensured the standing wave was symmetric; and made it easier to vary the spacing of the vortices on the free-surface as I could insist on a symmetric and numerically desirable point spacing at the quarter-period. This approach gives N equations

$$\begin{aligned}
X_i(\tau/2) &= \frac{2\pi(i-1)}{N} + B\sin(\frac{4\pi(i-1)}{N}) \quad && i = 2, \ldots, \frac{N}{2} \\
Y_i(\tau/2) &= Y_{\frac{N}{2}+2-i}(\tau/2) && i = 1, \ldots, \frac{N}{4} \\
\phi_i(\tau/2) &= -\phi_{\frac{N}{2}+2-i}(\tau/2) && i = 1, \ldots, \frac{N}{4} + 1
\end{aligned} \tag{2.2.6}$$

in $N+1$ unknowns $X_2, \ldots, X_{\frac{N}{2}}, Y_1, \ldots, Y_{\frac{N}{2}+1}$, and τ. The parameter B is used to control the mesh point distribution. For $B = 0$ the mesh points are equispaced in x at $t = \tau/4$ and for positive B the mesh points are clustered nearer the walls. This was found to be useful as a higher point concentration near the walls meant the wave profile and its dynamics could be determined more reliably. This is because

the most extreme dynamics occur near the walls especially when the wave is at its most extreme shape.

In previous research the wave steepness, defined as half the crest to trough height, is the determining parameter and thereby specifies the necessary additional equation. For waves not near the limiting profile this was found to be adequate and results in agreement to others (Schwartz and Whitney (1981), Rottman (1982)) were obtained. However, the wave steepness attains a maximum short of the limiting profile, and so I choose to use the initial crest acceleration, A_c,

$$\frac{\partial v_1}{\partial t} = -A_c \quad \text{at} \quad t = 0, x = 0, \tag{2.2.7}$$

as the determining parameter. Note that the acceleration due to gravity has been scaled to 1. The introduction of the crest acceleration parameter rather than the usual wave steepness parameter enables the calculation of more extreme wave profiles than previously possible.

This system of nonlinear algebraic equation is solved by a generalisation of Newton's method as given by Powell (1972). As an initial estimate for small acceleration I use the linear standing wave solution (a cosine profile) and then for subsequent estimates, as the crest acceleration is increased, I use an appropriate extrapolation of the previously determined profiles.

The reason for choosing the above approach is that it involves relatively few nonlinear equations, namely $\frac{N}{2} + 2$ or $N + 1$ of them, hence making the method reasonably fast and reliable. The time integration is done via the NAG routine D02CAF for waves not near the limiting profile. For waves near the limiting profile a Runge-Kutta method was found to perform better. Using this approach it is also easy to study the stability of the standing wave profiles. More complicated aperiodic flows and simulations may be calculated with only minor alterations to the basic algorithm.

2.3 Results

2.3.1 Accuracy and integral invariants

The case of standing waves in infinite depth has been studied using a variety of methods. Penny and Price, Aoki, Schwartz and Whitney, and Rottman have used a perturbation series approach to calculate the standing wave profile, the latter two calculating their series to high orders and using Padé approximants to sum the resultant series. Using the method described above I am able to calculate more extreme profiles than any of these previous methods. These previous results provide a useful check on this numerical procedure for the less extreme waves and were found to agree with the method used here.

For small crest accelerations a small number of points, $N = 16$ or 32, is sufficient to calculate the standing wave profile accurately. It is only when more extreme waves with large initial crest accelerations are calculated that I need to increase the number of points. For consistency all results given here will use $N = 64$ unless stated otherwise. Calculations using $N = 16$, 32 were performed on a Pyramid 9820 and a Sun 3/60. The $N = 64$ and $N = 128$ calculations were carried out on a SPARCstation 1+ and using the Fujitsu VP100 of the Australian National University Supercomputer Facility. $N = 256$ calculations were carried out using a suite of SPARCstation 1+ working in parallel using the C-Linda programming system. Calculations using $N = 128$ and $N = 256$ were in general only used for very extreme profiles and as a check on the profiles determined with $N = 64$.

Where possible the profiles were calculated with different number of mesh points per wavelength to detect any discretisation or integration errors. All profiles were found to be consistent. Profiles up to $A_c = 0.9700$ were calculated with both $N = 64$ and $N = 128$. However very extreme profiles could only be calculated with a large number of mesh points due to the more complex nature of the profile shape and the motion involved. Profiles with a crest acceleration in the range 0.9700 to 0.9800 were calculated using $N = 128$ and $N = 256$ and those with a

crest acceleration above 0.9800 using $N = 256$ only. As a check on these extreme profiles various different mesh point distributions and integration time steps were used to determine if the discretisation was affecting the shape of the standing wave profiles calculated. The point distribution was determined by the parameter B defined in (2.2.6). Using $N = 128$ for B ranging from 0 to 0.25 the extreme profiles differed by no more than 0.014% and the period by less than 0.007% (a value of $B = 0.25$ corresponds to approximately twice as many points near the initial crest of the wave as compared to $B = 0$). For the extreme waves where a Runge-Kutta method was used for the time integration, time steps ranging between 0.005 and 0.04 were used to independently calculate the profiles. The largest difference found was 0.003% for the profile and 0.002% for the period. All profiles were found to be consistent and I am confident the profiles are accurate to at least four significant digits.

The integral invariants are a further measure of the accuracy of the numerical approximation and hence an indicator of the accuracy of the standing wave profile calculated. I was able to accurately calculate profiles with an initial crest acceleration of up to $A_c = 0.9900$, that is 99.0% of gravity. Up to this value of A_c the largest error in the integral invariants was 4.1×10^{-10} which compares well with the integration tolerance used. I am therefore confident that the time integration is performed accurately and contributes little error to the calculations.

The solution to the nonlinear equations was considered to have converged when the sum of the squares of the residuals was less than 1×10^{-16}. In all cases considered the sum of the squares of the residues was considerably less than this. Thus the profiles calculated here replicate themselves after a period τ with a negligible relative error of less than 10^{-8}, and hence they form standing waves.

2.3.2 Properties of steep standing waves

Shown in Figure 2.2 is a plot of the wave steepness, h, versus the crest acceleration. The important feature to note is that there is a maximum wave steepness,

$h = 0.6202$ at $A_c = 0.9264$, which is short of the most extreme profile. This would explain why previous perturbation methods using the wave steepness as the perturbation parameter (e.g. Schwartz and Whitney) could not obtain convergence past $h \approx 0.62$. Previous estimates of the maximum wave steepness are therefore not a reliable estimator of the most extreme wave due to the non-monotonic nature of the wave steepness. Extreme standing waves should be referred to in terms of the crest acceleration, the crest angle or the crest curvature rather than the wave steepness as has been done previously. As the crest acceleration increases the crest height above the mean level also increases, but very slowly for large crest accelerations, while the downwards displacement at the trough attains a maximum at $A_c = 0.8464$ and then decreases as the crest acceleration increases. This is possible because as the crest acceleration increases the crest becomes sharper and narrower. This is highlighted by Figure 2.3 which is a plot of two profiles with the same wave steepness, $h = 0.6163$, but very different shapes. The solid line is the most extreme (reliable) profile calculated with $A_c = 0.9900$, and the dashed line a less extreme profile with $A_c = 0.8870$. Due to the sharper crest in the more extreme profile it is lower than the less extreme profile over the range $x \approx 0.05$ to $x \approx 0.86$ and higher elsewhere. The overall effect of this is for the more extreme profile to have less fluid above the mean level than the less extreme profile and hence is a lower energy solution. Figure 2.4 is a plot of the total energy versus the crest acceleration. There is a maximum in the energy, $E_{max} = 0.07775$ at $A_c = 0.8886$ ($h = 0.6167$), a wave steepness which is just less than the maximum.

Figure 2.5 shows the period of the standing wave profiles minus 2π versus A_c. The period has a maximum of $\tau_{max} = 2\pi + 0.2605$ at $A_c = 0.8893$ corresponding to a wave steepness of $h = 0.6168$. This is the same maximum Schwartz and Whitney found using a perturbation series approach. The period appears to have only a single extremum; this is in contrast with the steady progressive wave case where there is a succession of maxima and minima as the highest wave is approached.

Profiles up to the limiting profile would need to be calculated to verify this.

2.3.3 Extreme profiles

The most extreme profile I have calculated, that shown in Figure 2.3 as the solid line, has some interesting features to note. This profile has qualitative similarities with Taylor's (1953a) experimental findings close to the physical instability he found in the wave profile (his figures 16 and 17 in particular). Quantitatively these profiles differ due to the presence of surface tension, the difficulties of experimental work and the fact that Taylor's experiments were carried out in a finite depth tank (see §3.2.4 for a discussion of the changes to the extreme profile due to a finite depth lower fluid). As first noted by Schwartz and Whitney standing wave profiles above a certain wave steepness have more than one inflexion point. The plot of the surface inclination for the most extreme wave calculated, the solid line in Figure 2.6, clearly shows this. For this extreme profile there are 5 local maxima in the surface inclination (with an indication of more developing at higher A_c). The maximum inclination of $\theta = 50.4°$ occurs at $x = 0.0273$. As the crest acceleration is increased the number of inflexion points in the surface profile increases. The surface inclination for both $A_c = 0.2284$ ($h = 0.2000$) and $A_c = 0.5390$ ($h = 0.4000$) have one maximum whereas for $A_c = 0.8870$ ($h = 0.6163$) there are two local maxima in the surface inclination.

The shape of the limiting free surface standing wave profile, conjectured to be the profile having an initial crest acceleration equivalent to that of gravity, $A_c = 1$, has been of interest for many years. Previous workers, Schwartz and Whitney for example, have conjectured that the limiting profile has a cusped crest with an enclosed crest angle of 90°, although no formal proof exists to verify this. The work of Saffman and Yuen (1979) put the conjecture of a 90° crest angle in some doubt but their conclusions were unclear as they did not consider pure standing waves. They used two different approximations; firstly they prescribed an external pressure to an initially flat surface for a finite time before allowing the wave to

oscillate freely and secondly they used the fifth order expansions due to Penny and Price. Neither of these approximations repeated exactly and hence are not pure standing waves. The calculations performed here are in some respects a refinement of the work of Saffman and Yuen as I calculate numerically pure standing waves that repeat every period. My calculations indicate that the limiting profile is not a simple shape with an enclosed crest angle of 90°. As mentioned earlier there seems to be an increasing number of inflexion points in the profile as the crest acceleration is increased. Figure 2.7 is a plot of the maximum surface inclination versus the initial crest acceleration; note that a surface inclination of 45° corresponds to an enclosed angle of 90°. Clearly the maximum surface inclination does not tend to 45° as A_c tends to 1. Extrapolating the graph to $A_c = 1$ (the dashed line in Figure 2.7) I obtain a surface inclination between 60° and 65° which corresponds to an enclosed crest angle between 50° and 60°. However, the shape of the curve in Figure 2.7 suggests that this extrapolation is at best only indicative. Indeed it is conceivable that there is a maximum value for A_c less than 1 and standing waves with even larger surface inclinations than calculated here may exist. Previous estimates of the enclosed crest angle have extrapolated from considerably lower crest accelerations, at best from the wave steepness maximum at $A_c = 0.9264$, and hence have been erroneous in their estimates.

I have not yet been able to calculate standing wave profiles with a crest acceleration significantly larger than 0.9900 with sufficient degree of accuracy. The inability of a finite number of mesh points to accurately describe the sharp crest and the computational expense in increasing the number of mesh points being the limiting factors. The exact nature of the limiting profile is still an open question that needs addressing in the future. What is clear is that the limiting profile is not a simple curve with a sharply peaked crest. The increasing number of inflexion points in the profiles as the crest acceleration increases leads me to believe that the limiting profile has a complicated structure probably with many

small corrugations in the profile near the crest. The determination of the limiting profile is an obvious area of further research. Although the method has only been used here to calculate free–surface standing waves it has been formulated for an arbitrary density ratio in the range $0 \leq \rho < 1$. This method could therefore be used to calculate standing waves for other density ratios thereby clarifying and extending previous results in this area many of which have been inconclusive, for example see Rottman (1982).

2.3.4 Uniqueness

Another consideration when calculating standing waves is whether the profiles calculated are unique and, if not, where are the other solution branches. Resonant interactions are known to lead to multiple solutions in water waves. Short–crested waves, in which standing waves appear as a limiting case, were studied by Roberts (1983b) and many harmonic resonances were found. These resonant interactions give rise to zero divisors in a perturbation series approach which can be largely bypassed by using Padé summation. Linearly, deep–water standing waves resonate with an infinite number of harmonics, $\cos(n^2 x)\cos(nt)$. Schwartz and Whitney avoided zero–divisors by requiring that the secular terms in their series expansions be suppressed and then Padé summation was used to sum the resultant series. Rottman showed that even with suppression of the secular terms in the work of Schwartz and Whitney multiple solutions exist in the free-surface case although no examples were given. Combination waves such as those studied by Chen and Saffman (1979) in steady gravity-capillary waves could occur for standing waves but I saw no sign of them. In all the calculations of standing waves I performed I had no difficulty following the reported solution branch up to $A_c = 0.9900$. Globally, alternative profiles with the same crest acceleration do exist; the scaling analysis used later in Chapter 4 is a simple example of how to construct a profile that will have a crest acceleration equivalent to a different profile. The question that remains is: are there bifurcations that give rise to local multiple

solutions? From the superharmonic analysis given in §4.2 I obtain, in Figures 4.1a and 4.1b, plots of the eigenfrequency of the modes versus the crest acceleration. Local bifurcations in the solution are possible when the eigenfrequency of a particular mode passes through zero. Over the range of waveheights considered there are two resolved mode–pairs (mode 4 and mode 24) that have an eigenfrequency passing through zero. The mode 4 crossing is at the energy maximum and leads to an instability which is discussed in Chapter 4. No multiple solutions were observed in the vicinity of the mode 24 crossing. This does not say that bifurcations do not exist though. Harmonic stability calculations for larger crest accelerations than that calculated in Chapter 4 may well indicate the existence of local bifurcations. This is an area of further research. Chapter 4 also includes a subharmonic stability analysis which shows the existence of subharmonic bifurcations. Th is will be discussed in §4.3.

2.4 Conclusion and further work

2.4.1 Conclusion

The wave steepness of the standing wave profiles was found to have a maximum value short of the most extreme profile which explains why previous methods based on the wave steepness have been unable to obtain solutions close to the extreme profiles calculated and presented here. Previous attempts at estimating the limiting profile have incorrectly used wave steepnesses past this maximum and have hence been erroneous in their prediction of the limiting profile. By using the initial crest acceleration as the determining factor I have been able to accurately obtain standing wave profiles with an initial crest acceleration up to 99% that of gravity. This leads to new conjectures on the shape and dynamics of the limiting profile.

2.4.2 Further work

The exact nature of the limiting standing wave profile is clearly an area still open to further research. Although the numerical method used here cannot

be used to determine the limiting profile (due to the supposed singularity at the initial crest) it has certainly given insights into the limiting profile and reopened this area of study. Further work is necessary to fully understand the dynamics of the standing waves in this extreme case.

Using this method it is possible to determine standing waves with different density ratios between the two fluids. I expect this would clarify some previous work in this area which used a perturbation series approach to the problem and were inconclusive for some density ratios.

The numerical method used here has wider application than just studying standing waves. Aperiodic motion such as the sloshing of fluids in a tank can be studied by directly simulating the fluid dynamics. Also as an idealisation of the forced response of a water tank, periodically excited standing waves can be studied. These forced standing waves can exhibit chaotic behaviour in much the same way as a forced pendulum does, Tsai *et al* (1990). It is expected that this method could be used to model this behaviour.

The method can easily be adapted to study axisymmetric free-surface problems including axisymmetric free-surface standing waves and waves generated by a circular wavemaker. Extensions to the work of Tsai and Yue (1987) are expected to be possible in much the same manner as extensions were possible to the work of Vanden–Broeck and Schwartz (1981) for the two–dimensional case.

In Chapter 3 this method is extended to calculate standing waves on water of a finite depth and in Chapter 4 the stability of deep water standing waves is discussed.

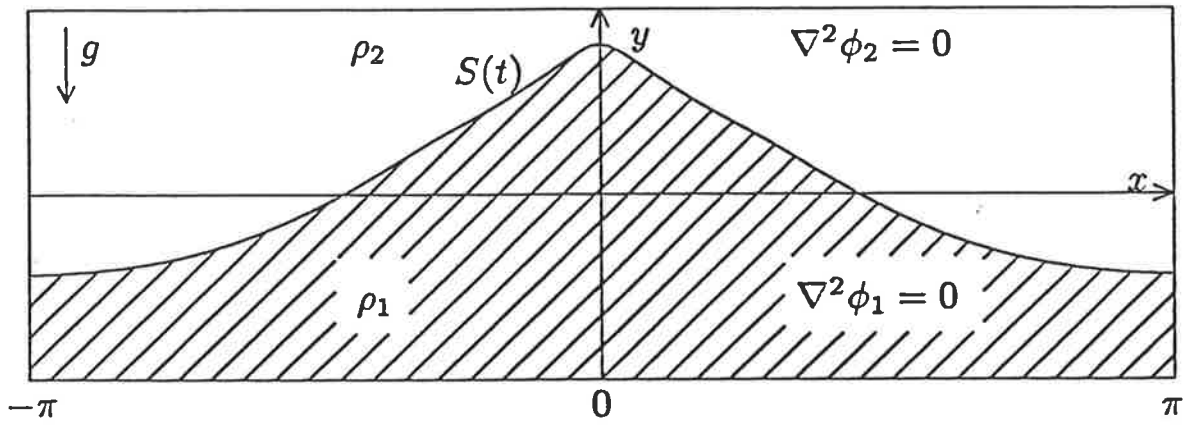

Figure 2.1: A schematic representation of interfacial standing waves, illustrating the co-ordinate system and nomenclature used in the text.

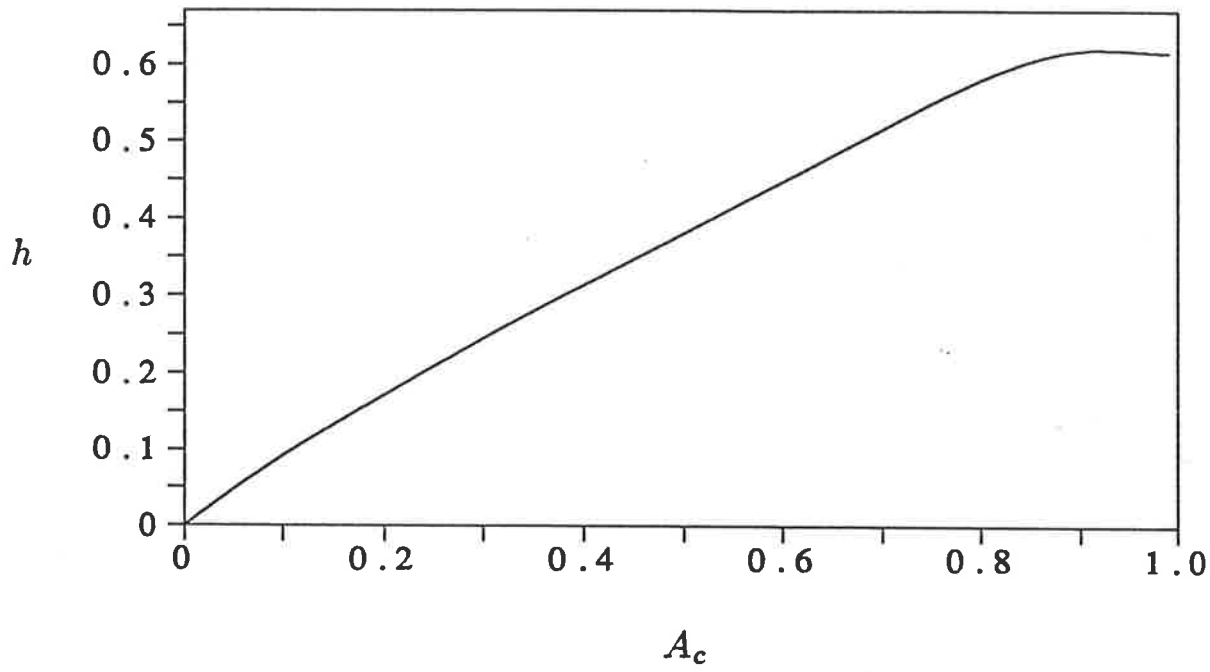

Figure 2.2: Wave steepness, h, versus initial crest acceleration, A_c, showing the maximum of $h = 0.6202$ at $A_c = 0.9264$.

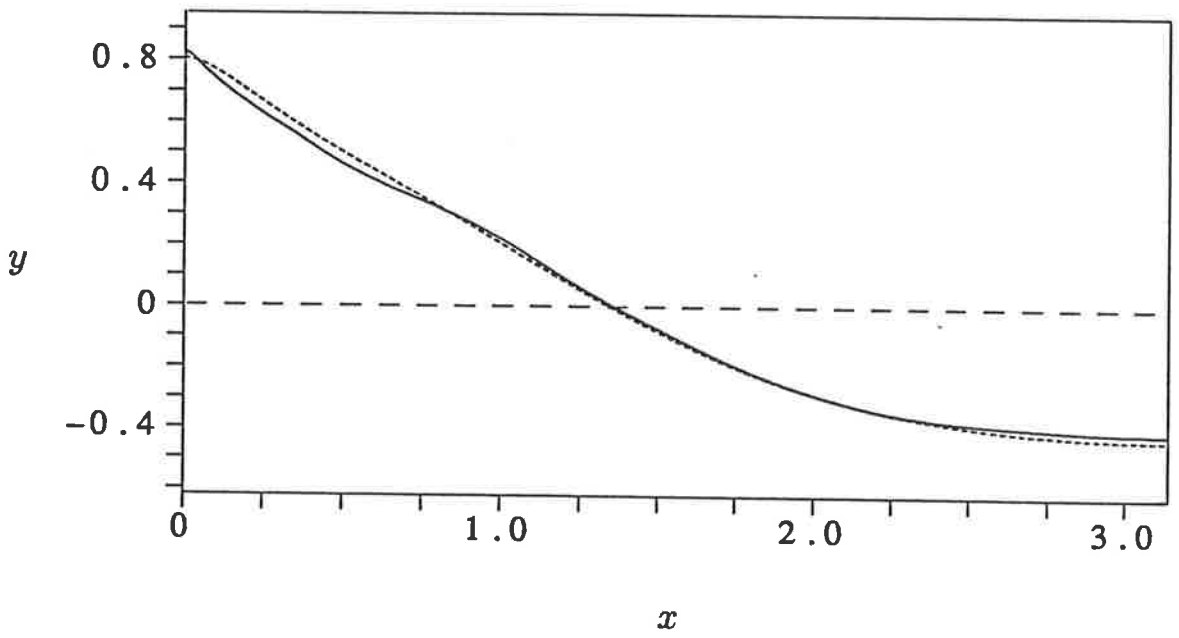

Figure 2.3: Two profiles with the same wave steepness, $h = 0.6163$, but different crest accelerations, $A_c = 0.9900$ (———) and $A_c = 0.8870$ (- - - -).

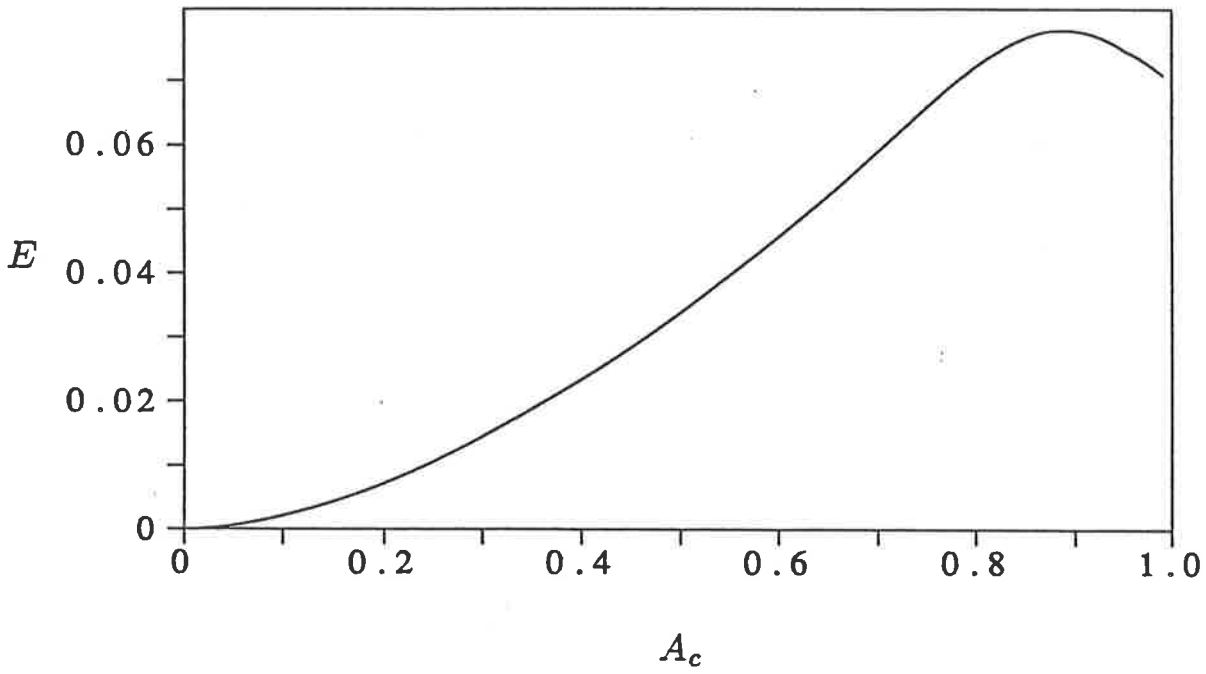

Figure 2.4: Total energy of the standing waves, E, versus the initial crest acceleration showing the maximum of $E_{max} = 0.07775$ at $A_c = 0.8886$ ($h = 0.6167$).

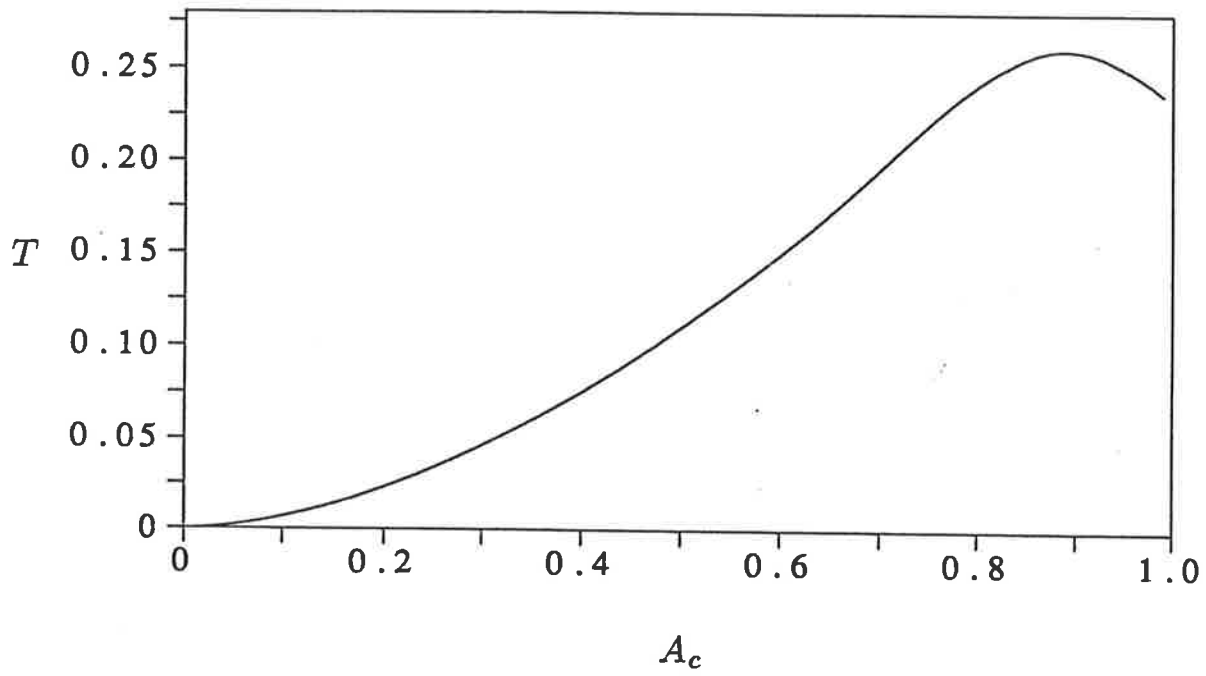

Figure 2.5: Period of the standing waves is $\tau = 2\pi + T$ where T is plotted as a function of the initial crest acceleration, showing the maximum of $T = 0.2605$ at $A_c = 0.8893$ ($h = 0.6168$).

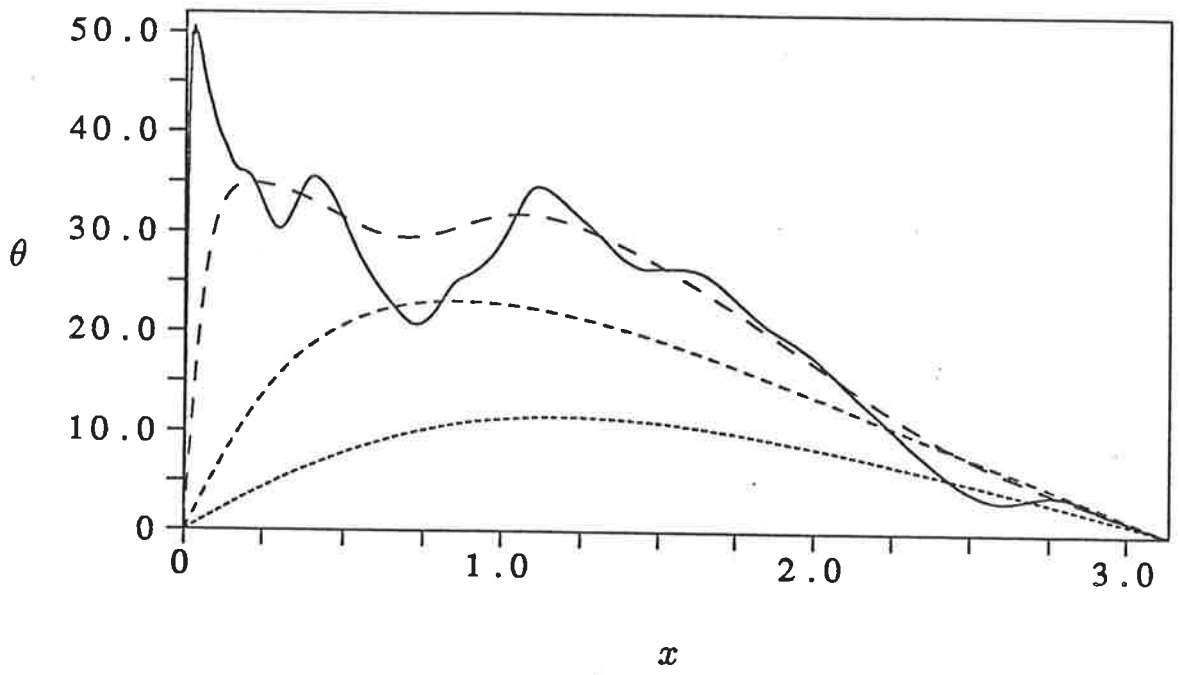

Figure 2.6: Surface inclination, θ, at $t = 0$ for four different values of the crest acceleration, $A_c = 0.9900$ ($h = 0.6163$) (———), $A_c = 0.8870$ ($h = 0.6163$) (– – –), $A_c = 0.5390$ ($h = 0.4000$) (- - - -), $A_c = 0.2384$ ($h = 0.2000$) (· · · · · ·), showing the increase in the number of inflexion points as the crest acceleration is increased.

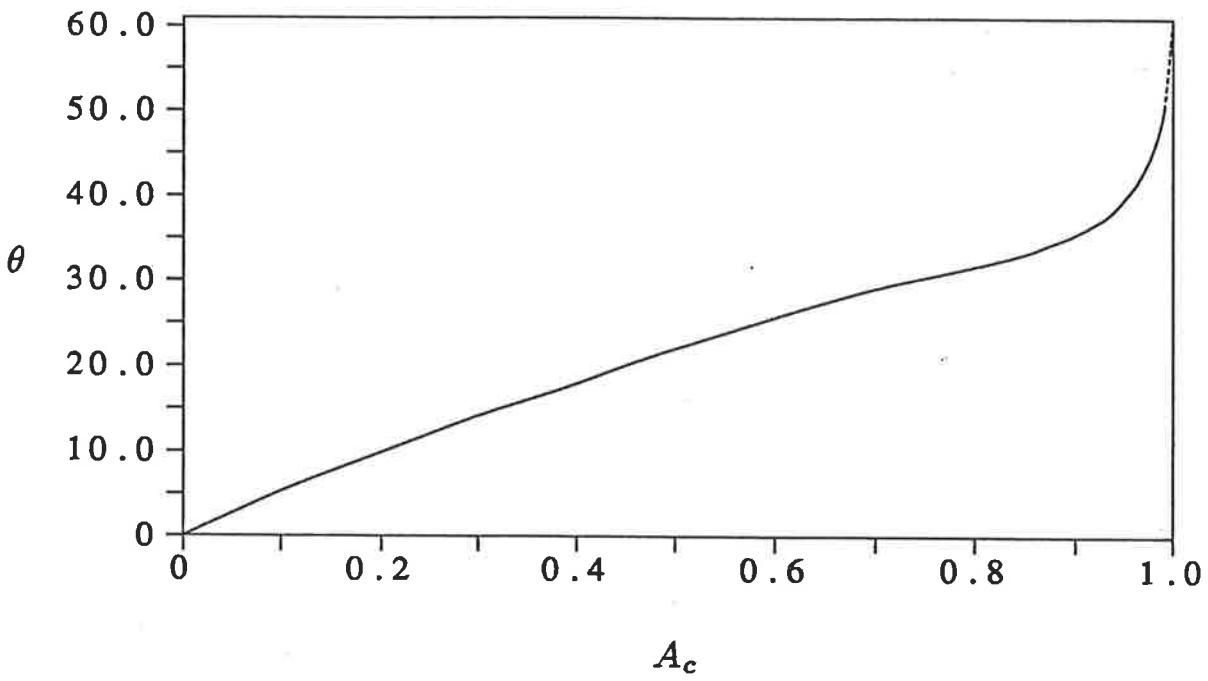

Figure 2.7: Maximum surface inclination, θ, versus initial crest acceleration at $t = 0$. The dashed section shows a possible extrapolation to $A_c = 1$.

CHAPTER 3

STANDING WAVES ON WATER OF FINITE DEPTH

3.1 Formulation and numerical method

3.1.1 Outline

The accurate calculation of the motion of a finite depth fluid has many practical uses. For example the sloshing of a fluid in a mixing tank or road tanker. Here I will use a generalisation of the method described in §2.1 and §2.2 to determine the motion of an interface between two fluids. The lower fluid being constrained by two vertical plates and a flat bottom and the upper fluid constrained by the same two vertical plates but of an infinite vertical extend above the interface. This general method is then used to calculate standing waves on water of finite depth. The method is formulated for an arbitrary density ratio between the fluids (ρ) but results are only presented for the free surface case ($\rho = 0$).

3.1.2 Finite depth changes

The same frame of reference as used in Chapter 2 is used here. The flat bottom is defined to be a depth d from the undisturbed interface (the x-axis). The bottom is a rigid impermeable boundary and hence we require the additional constraint that there is no flow through the boundary $y = -d$. This is incorporated into the scheme described in Chapter 2 using the method of images by including vortices below $y = -d$ which are the mirror image of those above $y = -d$. This forces the bottom ($y = -d$) to be an impermeable boundary. The same imaging as used in Chapter 2 for the side walls is also used here. See Figure 3.1 for a schematic diagram of the vortices and their images. The analysis follows exactly that used in Chapter 2 except for the inclusion of the additional image vortices. For this finite depth case equation (2.1.10) is modified to be

$$\left(\frac{\partial f}{\partial z}\right)_k = \frac{-i}{4\pi} \int\!\!\!\!\!\!- _0^N a_j \left[\cot\left(\frac{Z_k - Z_j}{2}\right) - \cot\left(\frac{Z_k - \overline{Z_j} + 2id}{2}\right)\right] dj \mp \frac{a_k}{2Z'_k}, \quad (3.1.1)$$

where this integral is a Cauchy principle value integral, the negative alternative gives the upper fluid's velocity and the positive the lower fluid's velocity. The

overbars denote complex conjugation. Equation (2.1.11) becomes

$$\phi_k' = \frac{1-\rho}{4\pi}\int_0^N a_j \Im\left\{Z_k' \cot\left(\frac{Z_k - Z_j}{2}\right) - Z_k' \cot\left(\frac{Z_k - \overline{Z_j} + 2id}{2}\right)\right\} dj + \frac{1}{2}(1+\rho)a_k. \tag{3.1.2}$$

Discretising (3.1.1) and (3.1.2) as described in §2.2 and allowing for the singularity at $j = k$, I obtain an equation for the velocity of the lower fluid particles on the interface to be

$$\begin{aligned}(u_1 - iv_1)_k = \frac{-i}{4\pi}\Bigg[&\sum_{j=0, j\neq k}^{\frac{N}{2}+1} a_j \cot\left(\frac{Z_k - Z_j}{2}\right) \\ &- \sum_{j=0}^{\frac{N}{2}+1} a_j \cot\left(\frac{Z_k - \overline{Z_j} + 2id}{2}\right) \\ &- \sum_{j=1}^{\frac{N}{2}} a_j \left[\cot\left(\frac{Z_k + \overline{Z_j}}{2}\right) - \cot\left(\frac{Z_k + Z_j + 2id}{2}\right)\right]\Bigg] \\ &+ \frac{a_k}{2Z_k'} + \frac{Z_k'' a_k}{Z_k'^2} - \frac{2a_k'}{Z_k'},\end{aligned} \tag{3.1.3}$$

and an equation involving ϕ' and a_j

$$\begin{aligned}\phi_k' = \frac{1-\rho}{4\pi}\Bigg[&\sum_{j=0, j\neq k}^{\frac{N}{2}+1} a_j \Im\left\{Z_k' \cot\left(\frac{Z_k - Z_j}{2}\right)\right\} \\ &- \sum_{j=0}^{\frac{N}{2}+1} a_j \Im\left\{Z_k' \cot\left(\frac{Z_k - \overline{Z_j} + 2id}{2}\right)\right\} \\ &- \sum_{j=1}^{\frac{N}{2}} a_j \Im\left\{Z_k' \cot\left(\frac{Z_k + \overline{Z_j}}{2}\right) - Z_k' \cot\left(\frac{Z_k + Z_j + 2id}{2}\right)\right\} \\ &+ \Im\left\{\frac{Z_k''}{Z_k'}\right\}\Bigg] + \frac{1}{2}(1+\rho)a_k.\end{aligned} \tag{3.1.4}$$

To determine the motion of a fluid interface where the fluid is bounded by the vertical walls $x = 0$, $x = \pi$ and the rigid bottom $y = -d$, solve (3.1.4) for the vortex strength a_j and then substitute into (3.1.3) to calculate the surface

velocities. Equations (2.1.2) and (2.1.8) can then be used to integrate forward in time and determine how the profile evolves. Exactly the same method as used in Chapter 2 is then used to calculate standing waves on finite depth water.

3.2 Results

3.2.1 Accuracy and integral invariants

For consistency all results presented here were calculated using 64 mesh points per wavelength unless stated otherwise. All calculations were carried out on a SPARCstation 1+. As described in §2.3.1 for the infinite depth standing waves, a variety of integration time steps and point distributions were used to ascertain any discretisation or integration errors. For integration time steps between 0.02 and 0.08 and point distribution parameter B between 0 (points equispaced at the quarter period) and 0.25 the profiles were found to be consistent.

The integral invariants described in §2.1.2 were used as a further measure of the accuracy of the standing wave profiles calculated. For all the different depths and crest accelerations used the largest error in the integral invariants was 2.5×10^{-6}. Most errors in the integral invariants were considerably less than this. The integral invariants are a good measure of the accuracy of the time integration and so I am confident there is little contribution to the error from the time integration. Better accuracy can be obtained by increasing the number of mesh points, but this comes at the expenses of increased computational time.

3.2.2 Comparison to previous methods

The work of Vanden–Broeck and Schwartz (1981) provides a useful check on the coding of the method presented here. Table 3.1 shows values of ω/ω_0 for $d = 3.0$ with $N = 8, 16, 32, 64$ for various waveheights from 0.1 to 0.27 where ω is the frequency of the wave and ω_0 is defined by

$$\omega_0^2 = \tanh(d) \tag{3.2.1}$$

and is the frequency of the corresponding linear wave. Also included in Table 3.1

are the results of Vanden–Broeck and Schwartz for $N = 8, 12, 16$ where M is the order of truncation of their summations.

The present method has converged to five decimal places for all the values of the waveheight considered whereas Vanden–Broeck and Schwartz's results have converged to four decimal places for $h \leq 0.2$ and to three decimal places for $h > 0.2$. The close agreement with the results of Vanden–Broeck and Schwartz and the convergence of the method presented here indicate that the method is indeed coded correctly and accurately calculates standing waves.

	Present Method				Vanden-Broeck & Schwartz		
h	N=8	N=16	N=32	N=64	M=8	M=12	M=16
0.1	0.99878	0.99877	0.99876	0.99876	0.99877	0.99876	0.99876
0.15	0.99725	0.99724	0.99724	0.99724	0.99727	0.99724	0.99722
0.2	0.99514	0.99512	0.99512	0.99512	0.99520	0.99511	0.99505
0.25	0.99248	0.99243	0.99243	0.99243	0.99262	0.99241	0.99228
0.27	0.99126	0.99121	0.99120	0.99120	0.99143	0.99117	0.99096

Table 3.1: *Values of ω/ω_0 for $0.1 \leq h \leq 0.27$ and various N comparing the present method to the work of Vanden–Broeck and Schwartz.*

3.2.3 Harmonic resonances

As first noted by Tadjbakhsh and Keller (1960) there are certain depths at which the linear theory does not have a unique solution. This is due to harmonic resonance between the fundamental wave and its higher harmonics. This was extended by Marchant and Roberts (1987) to the case of short–crested waves in finite depth of which standing waves are a limiting case. I will use the notation of Marchant and Roberts and so the resonance due to the $(m,n)^{\text{th}}$ harmonic

$$\sin(m\omega t)\cos(nx)\frac{\cosh(n(y+d))}{\cosh(nd)} \tag{3.2.2}$$

occurs at depths given by

$$n \tanh(nd) = m^2 \tanh(d) \tag{3.2.3}$$

where m, n are integers, such that their sum is even and $n < m^2$. As first argued by Concus (1964) and extended to short–crested waves by Marchant and Roberts (1987) the set of depths defined in (3.2.3) is everywhere dense in $(0, \infty)$. Therefore any perturbation series based on the harmonics will have an everywhere zero radius of convergence. Due to these harmonic resonances the standing wave profile is not unique but, as described in Roberts (1981), the "distance" between different solution branches in the region of the resonance is typically very small being of the order of $h^{\max(m,n)/3}$ where h is the waveheight. Most of these resonances are therefore extremely weak and do not affect the numerical method outlined here for the calculation of standing waves in finite depth. The dominant resonances and hence the the ones where multiple solutions are most likely to be observed are ones for which m and n are small; for instance $(3,5)$, $(3,7)$, $(4,6)$, $(4,8)$ which correspond to the depths $d = 0.624, 1.040, 0.386, 0.550$. The depths at which these harmonic resonances occur are derived from the linear theory and hence are only accurate for small wave amplitudes. For larger wave amplitudes the harmonic resonances still exists but the depths at which they occur will differ from that predicted by the linear theory.

The effect of the harmonic resonance can be seen in some of the wave properties, for instance the frequency or wave energy. Figure 3.2 is a plot of the scaled frequency, ω/ω_0, for various fixed crest accelerations, $A_c = 0.05$, 0.10, 0.15, 0.20, 0.25 versus the depth d. The depths at which the dominant harmonic resonances occur for the linear theory are also plotted. For small crest accelerations (and hence small waveheights) the "width" of the influence of the harmonic resonance is very small and hence only the strong harmonic resonances have any noticeable effect; for instance the effect of the $(3,5)$ harmonic resonance can be seen for $A_c = 0.05$ and the $(4,10)$ and $(3,5)$ for $A_c = 0.10$. For larger crest accelerations the harmonic

resonance has a wider effect and becomes quite noticeable, for instance the $(3,7)$ and $(4,10)$ for $A_c = 0.15$; the $(4,14)$ and $(3,7)$ for $A_c = 0.20$ and $A_c = 0.25$. I was unable to follow solution branches lower in depth than those shown in Figure 3.2 for a fixed crest acceleration, the jump across the resonance was too large to use the previous depth solution as a useful estimate for a lower depth. Instead, to complete the calculation of profiles in both the depth and crest acceleration parameter ranges, it was necessary to choose a depth, calculate the profile for a small crest acceleration (say $A_c = 0.05$) which will not differ much from the linear theory and then use this as an estimate to increase the crest acceleration. This too is subject to a similar problem as that encountered for a fixed crest acceleration and variable depth as the depths at which harmonic resonances occur are not fixed but vary with the crest accelerations, although in general this method has a lot fewer resonances to contend with. Figure 3.3 is a plot of the scaled frequency, ω/ω_0, versus the crest acceleration, A_c, for fixed depths $d = 0.562$, 0.693, 0.799, 1.204, 2.207, ∞. Note that a similar scaling for the depth as used by Cokelet (1977) has been used here : hence $e^{-d} = 0.57$, 0.50, 0.45, 0.30, 0.11, 0. The graph for $d = 0.562$ has two solution branches in the range $A_c = 0.17$ to 0.29 which is due to the $(5,13)$ resonance which occurs at a depth $d = 0.577$ in the linear theory. The graphs for the other depths shown may well have similar features but the resonances are too weak to have a noticeable effect.

Due to these harmonic resonances there is not necessarily a unique profile for a given value of the parameters. For example, Figure 3.4 show plots of two different profiles for the same depth $d = 0.562$ with the same crest acceleration $A_c = 0.18$. This is in the range mentioned previously where the influence of the (5,13) harmonic resonance is felt, the effect of the harmonic resonance is obvious in the dashed profile.

3.2.4 Properties

As shown in Figure 3.2 the general trend for small crest accelerations, ignor-

ing any local effects due to harmonic resonances, is that for a given crest acceleration the scaled frequency of a standing wave increases as the depth decreases. This is not true for large crest accelerations though, as is shown in Figure 3.3 where for large crest accelerations (that is crest accelerations near unity) the scaled frequency for the infinite depth case is greater than that for $d = 2.207$. Indeed, as expected, for relatively deep water there is little difference in the infinite depth profiles and the deep water profiles until the crest acceleration is near that due to gravity, for example the plots of the scaled frequency for the infinite depth case and $d = 2.207$ differ very little for $A_c \leq 0.7$, it is only for $A_c > 0.7$ that there is any appreciable difference. This is a further reason why the work of Taylor (1953a) incorrectly predicted the maximum waveheight for infinite depth standing waves. He was using a finite depth tank with a depth in the present non–dimensional units of approximately $d = 1.48$. For extreme standing waves this finite depth will have an effect on the standing wave profile.

An interesting feature to note is that for crest accelerations near unity (when it was possible to calculate standing wave profiles with large crest accelerations for the given depth) each plot of ω/ω_0 has an extremum. For crest accelerations near these frequency extrema there are also energy maxima in a similar manner to the infinite depth case. From the theory of Saffman (1985) it is expected that these finite depth standing waves would have instabilities associated with these energy maxima (see Chapter 4 for a discussion on the stability of standing waves in deep water).

To second order Tabjbakhsh and Keller found that there is a critical depth, $d^\star \approx 1.07$, such that "for depths greater than $d^\star$, the fluid behaves like a soft spring, its free vibration frequency decreasing with increasing amplitude. For depths shallower than $d^\star$, the fluid behaves like a hard spring, its free vibration increasing with increasing amplitude." Using the high order perturbation series of Marchant and Roberts (1987) an improvement on this was found to be $d^\star \approx 1.058$,

Marchant (1988). Although this is valid in the limit as the waveheight, and hence the crest acceleration, tends to zero, there is no single depth at which the behaviour of the frequency changes for all waveheights (crest accelerations). From Figure 3.2, for crest accelerations in the range $A_c = 0.05$ to 0.15, this critical depth is in the range $d = 0.96$ to 1.01. This is in agreement with the experimental work of Virnig *et al* (1988) who found, once their work is non–dimensionalised in the manner used here, that the critical depth occurred in the range 0.907 to 1.027. Their inability to obtain frequency response curves within this range could be due to the relatively strong $(3, 7)$ and $(4, 12)$ harmonic resonances that occur at depths predicted by the linear theory of $d = 1.040$ and 0.973 respectively.

Now choosing a particular depth, $d = 0.562$, I will report on some of the specific properties of the standing wave profiles in this depth. Figure 3.5 is a plot of the standing wave profiles for four different crest accelerations, $A_c = 0.20$, 0.40, 0.60, 0.80, for the fundamental wave, that is the profiles that are least affected by the harmonic resonances. As the crest acceleration increases the crests heighten and steepen and the troughs broaden. Similar to the infinite depth case the most extreme profile calculated at this depth with a crest acceleration $A_c = 0.95$, has a humped appearance and a complex structure. The intricacies of which are evident in Figure 3.6a a plot of the standing wave profile and Figure 3.6b a plot of the corresponding surface inclination. The profile can be divided in roughly three sections, a definite steep sharp crest for $0 \leq x < 0.25$, a broad hump for $0.25 < x < 1.25$ and a wide trough for $1.25 < x \leq \pi$. The broad hump and the trough have a very detailed structure with the trough having a local maxima. This detailed structure is necessary to obtain the correct crest shape at the half period.

This standing wave profile maintains a definite crest as the wave moves across the tank. This is shown in Figure 3.7 which is a plot of surface particle trajectories from $t = 0$ to $t = \tau/2$. The surface particles which are initially between the crest and the trough rise and fall and are moved across the tank as the crest moves

through. This is clearly seen in Figures 3.8 which are plots of the velocity field for $t = \tau/20,\ 2\tau/20, \ldots, 9\tau/20$. For times near the quarter period there is a pronounced central crest moving across the tank with an almost constant velocity in a vertical cross–section below the crest. It is only near the half period where the effect of the side wall forces this crest to rise and there is a pronounced vertical velocity near the wall. This phenomenon of a pronounced crest moving across the tank becomes more pronounced as the depth decreases. In the limit as the depth approaches zero the standing wave can be interpreted as simply a solitary wave bouncing between two walls.

3.3 Conclusion and further work

3.3.1 Conclusion

The method outlined in Chapter 2 has been extended to allow for a finite depth lower fluid. Standing waves on water have been calculated for various depths and over a range of crest accelerations. Particular attention has been paid to harmonic resonances and how these affect the standing wave profile. Multiple solutions were found to exist near the resonant depths.

3.3.2 Further work

An obvious area for extensions to this work is to calculate standing waves in shallower fluids than that considered here and to calculate more extreme profiles. To accurately model these more extreme cases the number of mesh points used needs to be increased which can become computationally expensive if implemented over a wide parameter range. As mentioned in Chapter 2 for standing waves on infinite depth water, different density ratios and surface tension effects could also be included.

Further analysis is possible in the vicinity of the depths at which harmonic resonances occur to fully investigate the behaviour of the standing waves near these resonances and how they effect the stability of the standing waves.

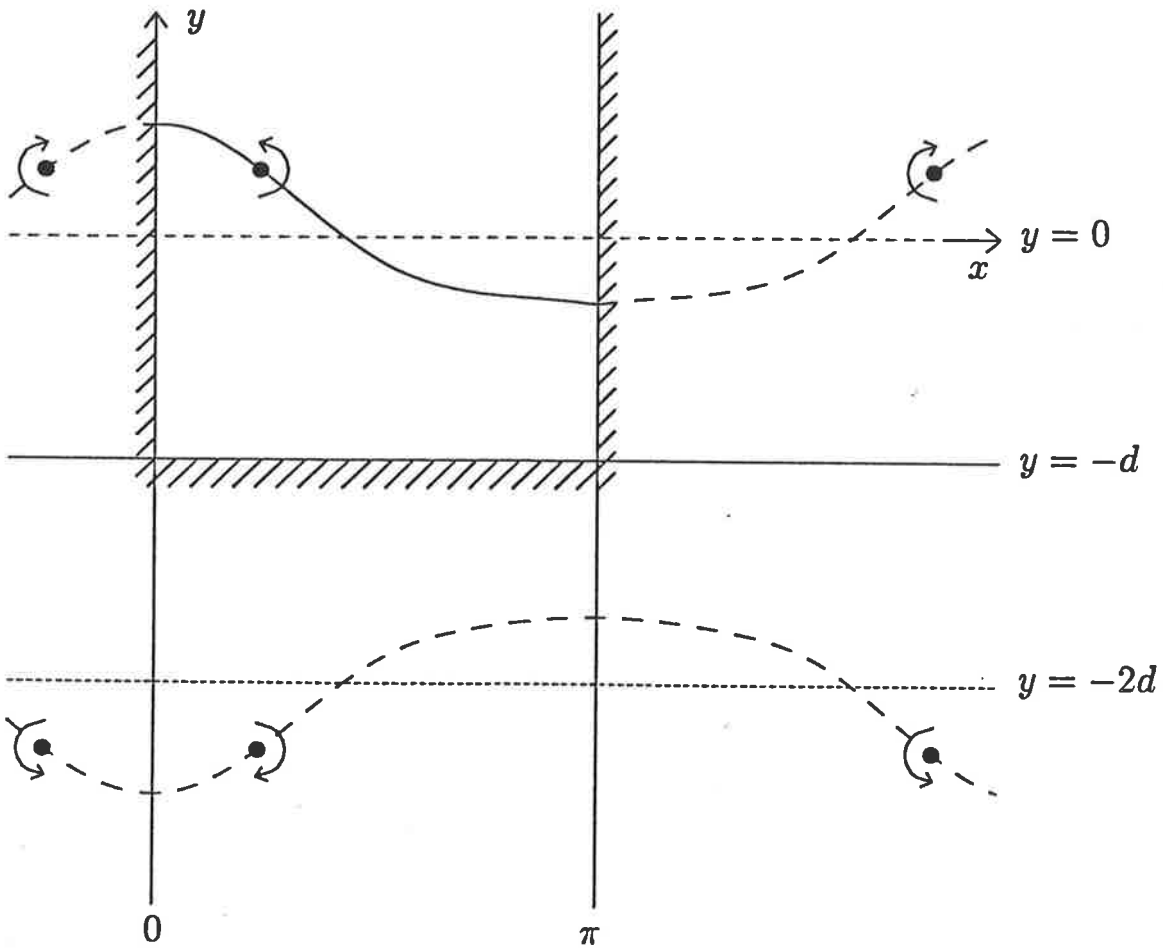

Figure 3.1: A schematic representation of the vortices and their images in the side walls ($x = 0, \pi$) and the bottom ($y = -d$).

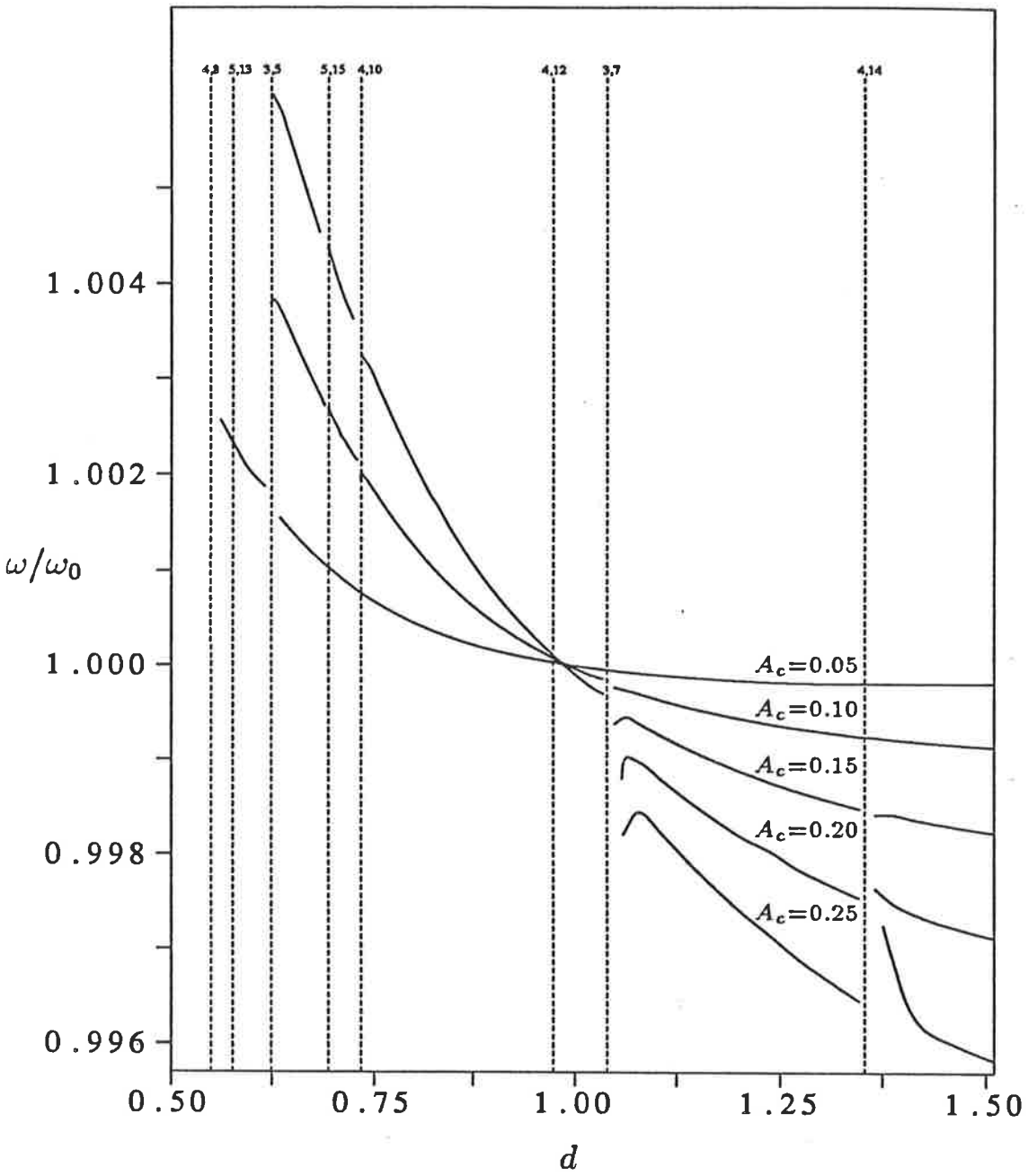

Figure 3.2: Scaled frequency, ω/ω_0, versus depth, d, for five values of the crest acceleration, $A_c = 0.05$, 0.10, 0.15, 0.20, 0.25, showing the discontinuities due to the harmonic resonances. The depths at which the harmonic resonances occur from the linear theory are shown as the dashed lines.

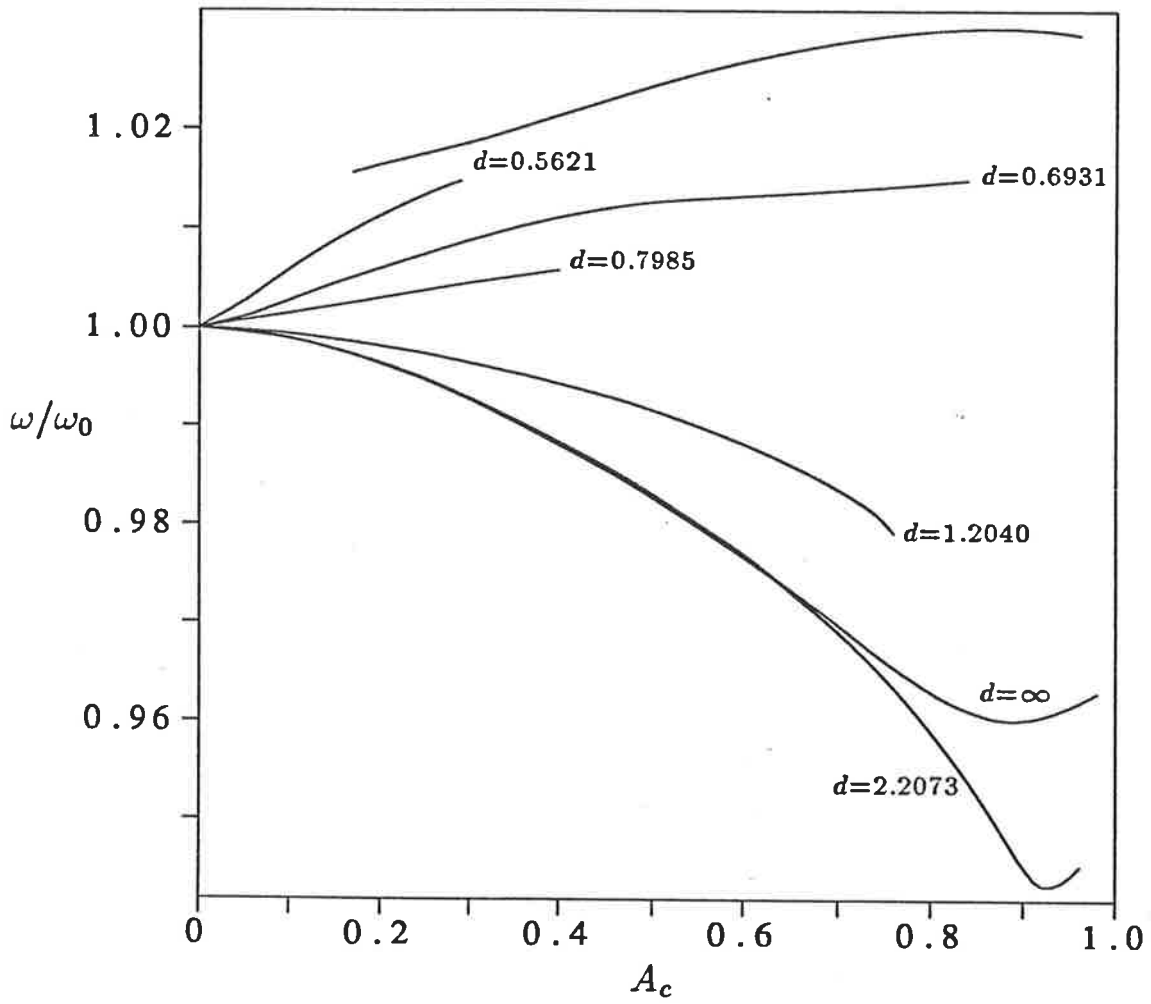

Figure 3.3: Scaled frequency, ω/ω_0, versus the crest acceleration for six values of the depth $d = 0.562, 0.693, 0.799, 1.204, 2.207, \infty$.

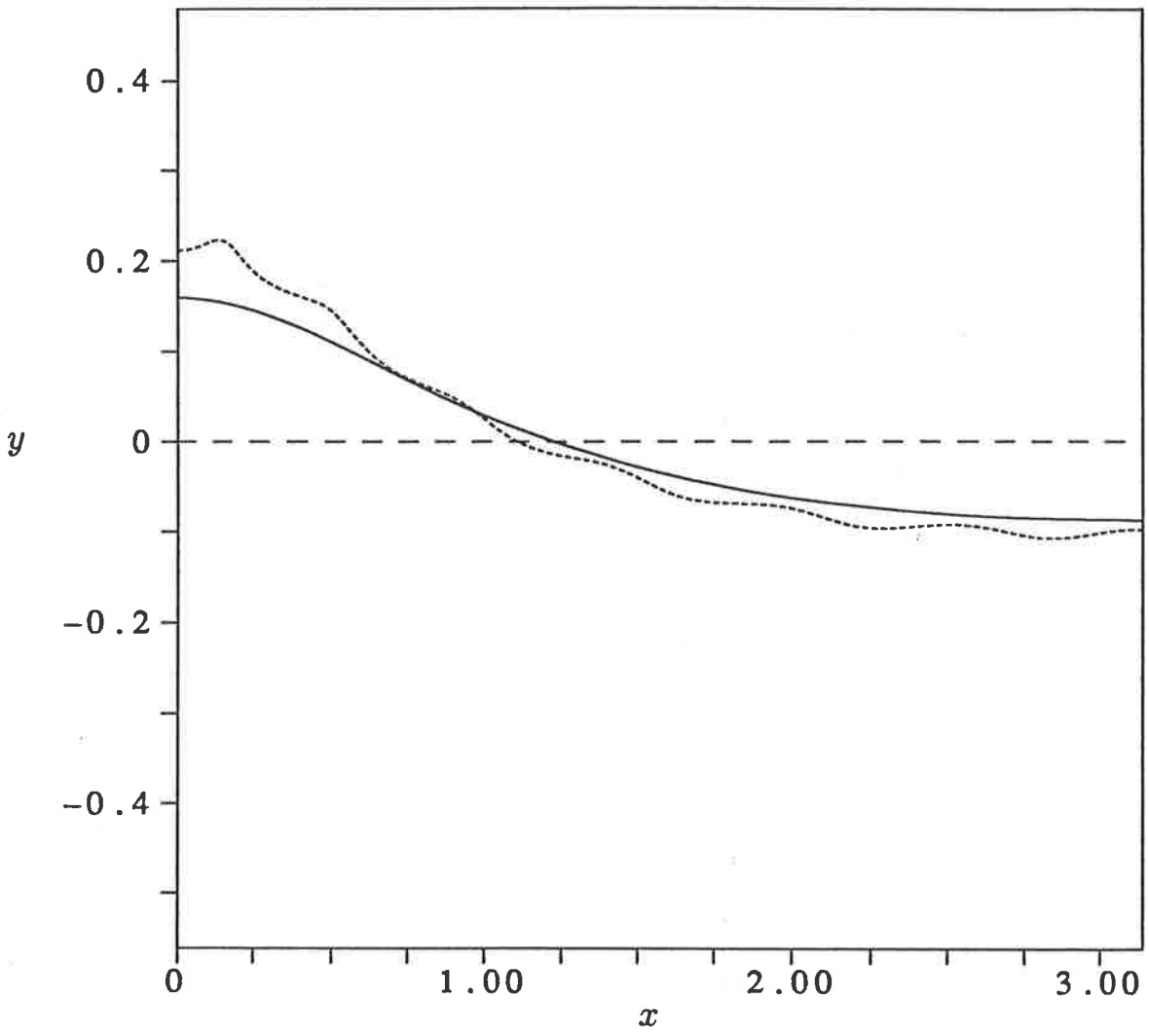

Figure 3.4: Two different profiles for the same value of the depth ($d = 0.562$) and the crest acceleration ($A_c = 0.18$). The dashed curve is a profile showing the effect of the $(5, 13)$ harmonic resonance. Note that the vertical scale has been exaggerated by a factor of three.

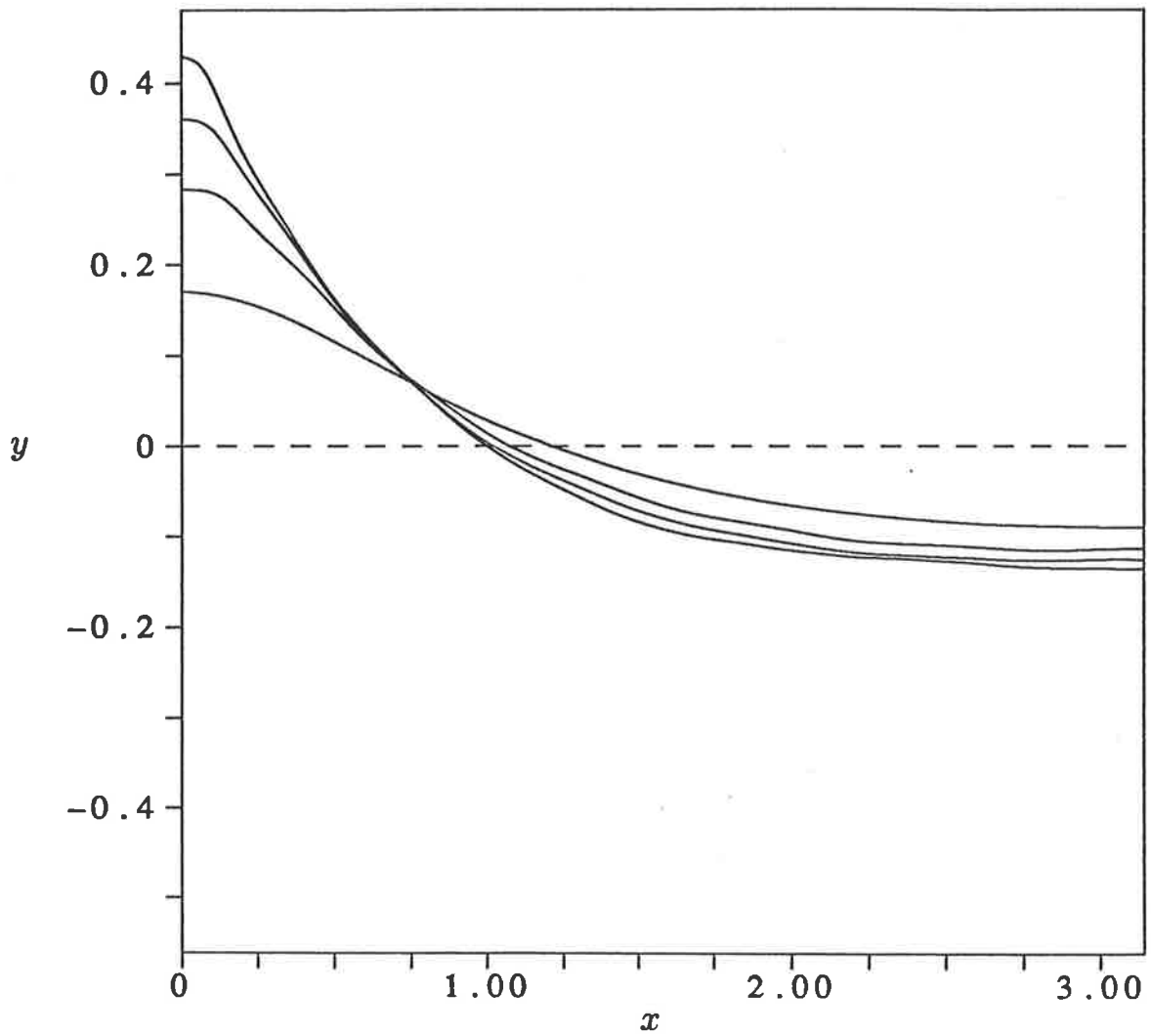

Figure 3.5: Profiles with $A_c = 0.20, 0.40, 0.60, 0.80$ for $d = 0.562$ showing the effect of higher crest acceleration which is to steepen and narrow the crest and broaden the trough. The vertical scale has been exaggerated by a factor of three. On the left-hand side the crest acceleration increases bottom to top.

(a)

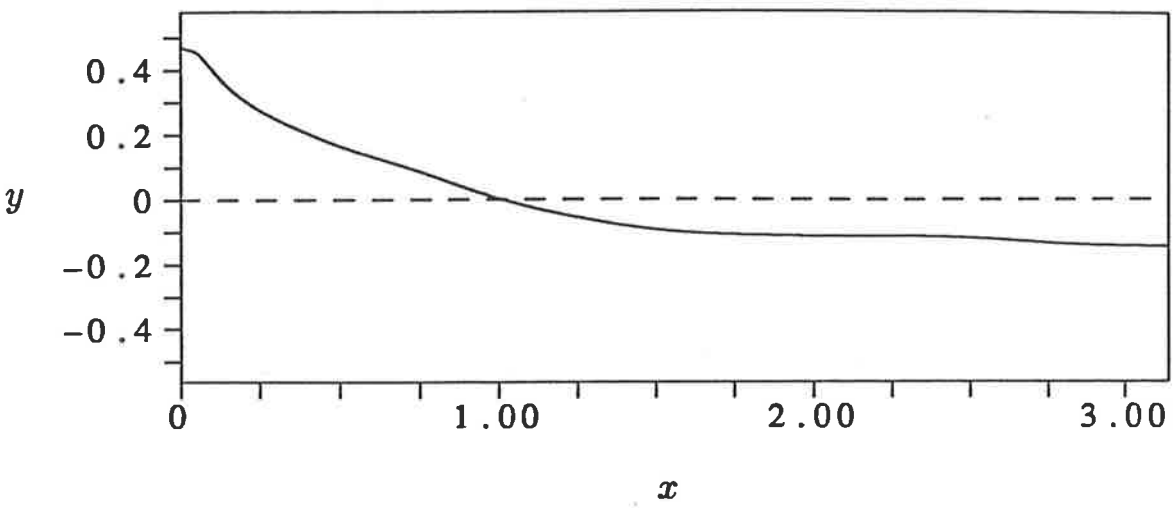

(b)

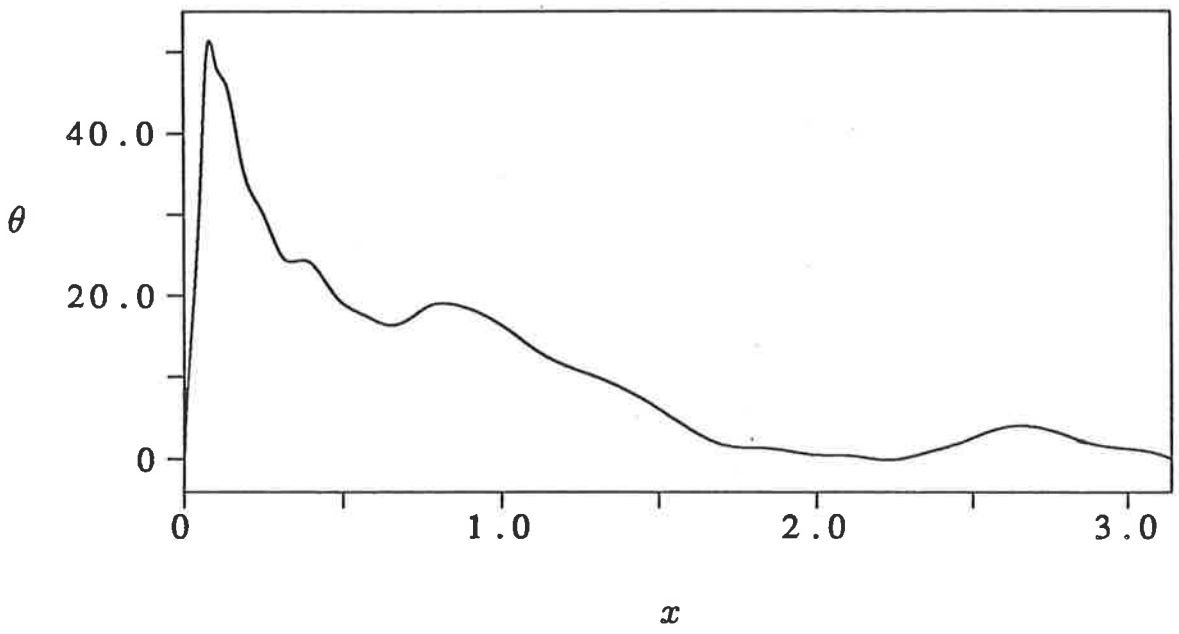

Figure 3.6: (a) Profile for $A_c = 0.95$ and $d = 0.562$, to scale; (b) the corresponding surface inclination, θ.

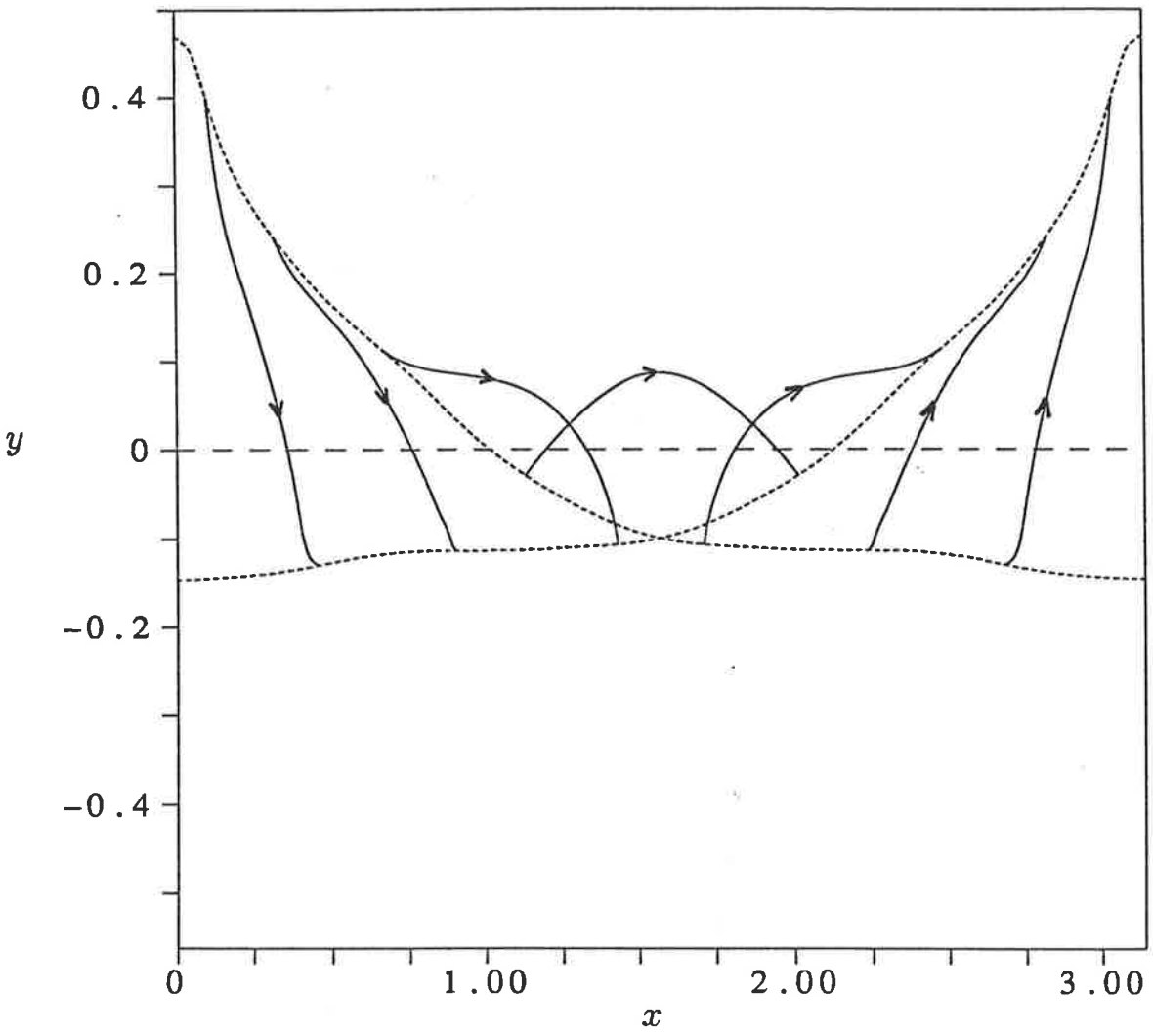

Figure 3.7: Surface particle trajectories for $t = 0$ to $t = \tau/2$ and the profile at $t = 0$ and $t = \tau/2$ (- - - - -). The vertical scale has been exaggerated by a factor of three.

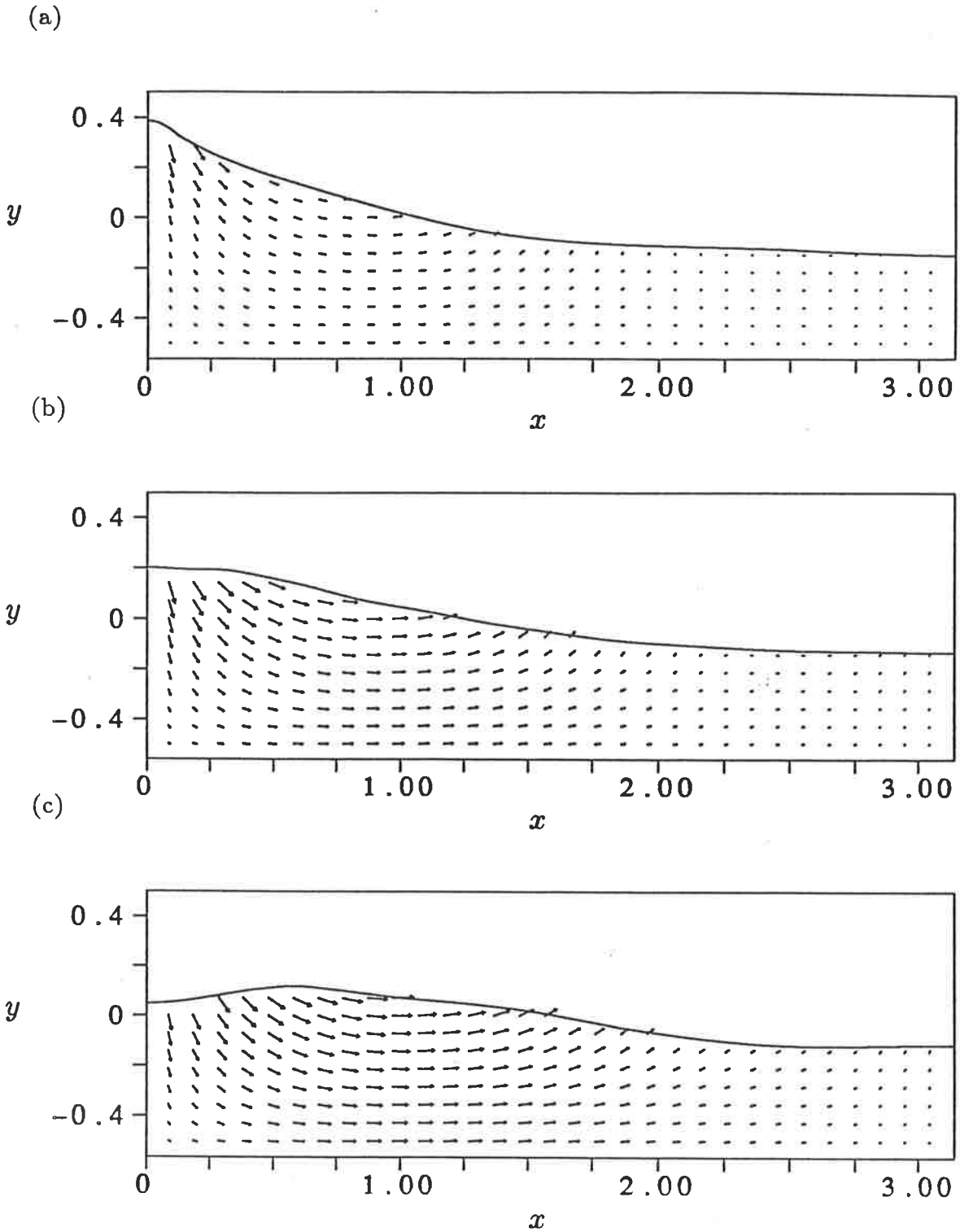

Figure 3.8: (a)–(i) Velocity fields at $t = \tau/20 \ldots 9\tau/20$ respectively for $A_c = 0.95$, $d = 0.562$, to scale.

(d)

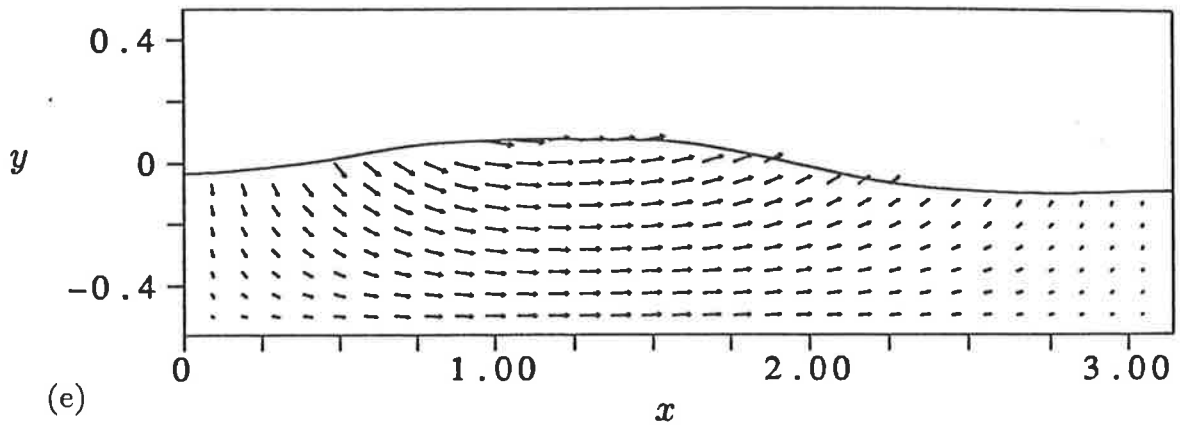
0.4
0
-0.4
y
0
1.00
2.00
3.00
x

(e)

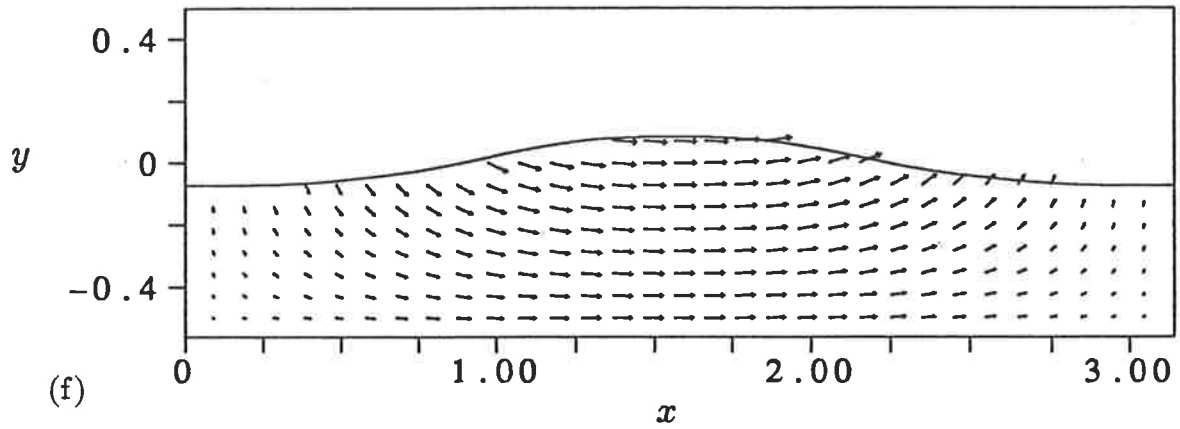
0.4
0
-0.4
y
0
1.00
2.00
3.00
x

(f)

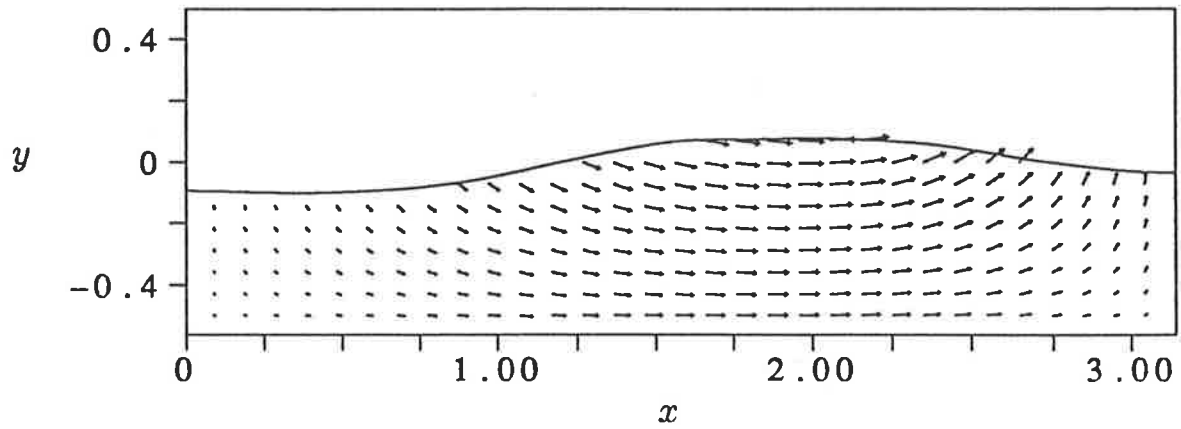
0.4
0
-0.4
y
0
1.00
2.00
3.00
x

(g)

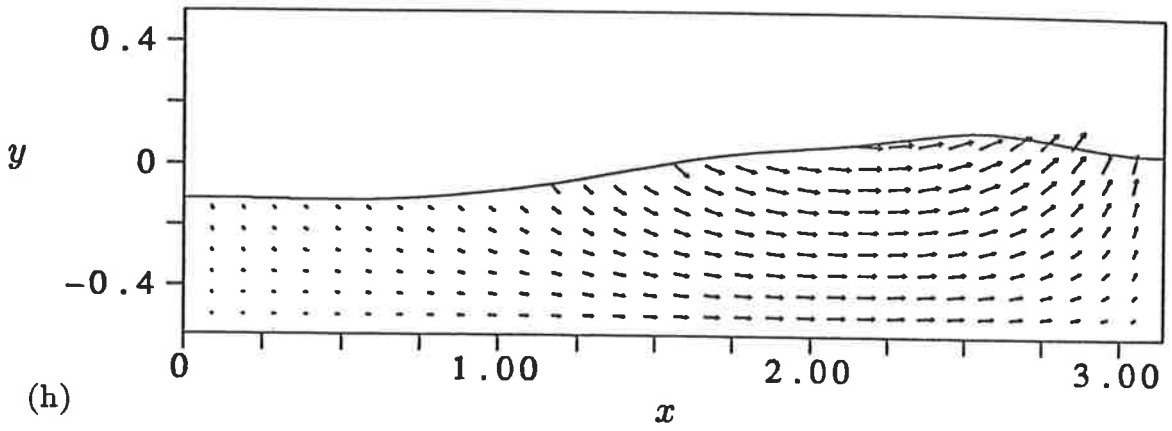
0.4
y
0
-0.4
0
1.00
2.00
3.00
x

(h)

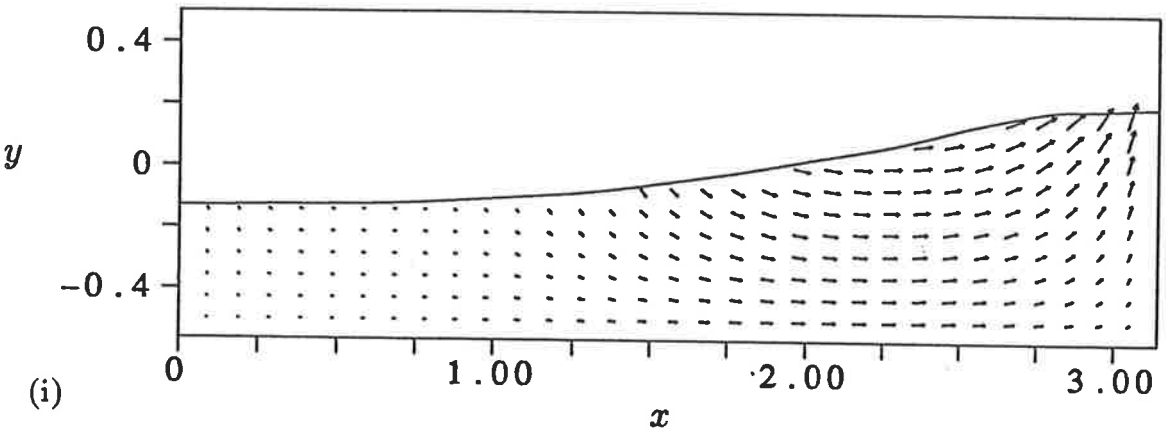
0.4
y
0
-0.4
0
1.00
2.00
3.00
x

(i)

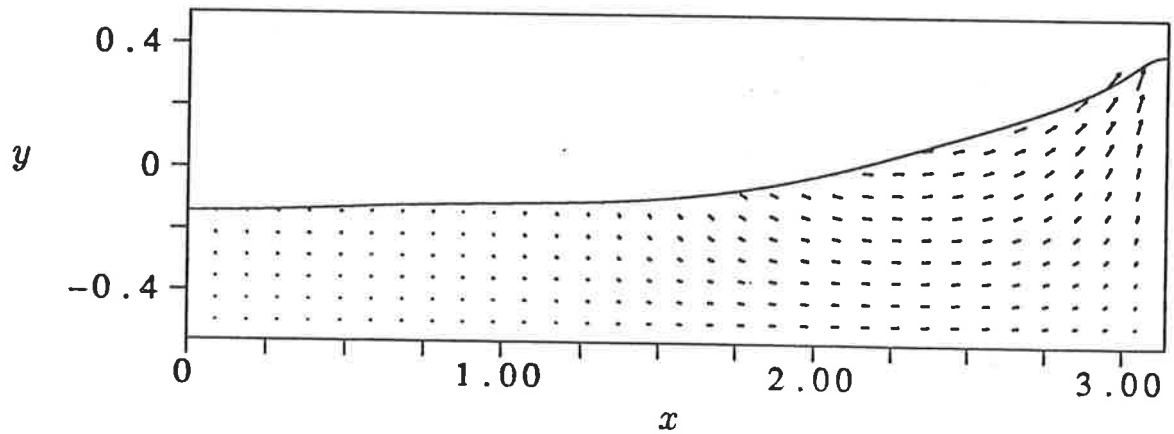
0.4
y
0
-0.4
0
1.00
2.00
3.00
x

CHAPTER 4

THE STABILITY OF STANDING WAVES ON DEEP WATER

4.1 General method

4.1.1 Introduction

The stability of travelling water waves has been extensively studied. Longuet-Higgins (1978a, 1978b) analysed numerically both the harmonic and subharmonic stability from the exact water wave equations. Although the analysis is restricted to discrete perturbation wavenumbers it does have the advantage that it uses the exact equations. Crawford *et al* (1981) used an approximation due to Zakharov (1968) to study the stability of weakly nonlinear waves. McLean (1982) used a numerical method based on a truncation of the Fourier modes to investigate the stability of Stokes waves in infinite depth water. Since then much has been done in the field of stability of travelling waves, see Tanaka (1985), Saffman (1985), Mackay and Saffman (1986) and Kharif and Ramamonjiarisoa (1988, 1990) for just some of the more recent contributions in this area. In contrast, very little has been done on the stability of two-dimensional standing waves. Okamura (1984) calculated the instability of weakly nonlinear standing waves using the Zakharov equation which is only valid for small amplitude standing waves. Here I will analyse the two-dimensional stability of standing waves in infinite depth water numerically for both harmonic and subharmonic stability.

One method of analysing the stability is to perturb the standing wave, integrate forward in time and observe how each perturbation affects the fluid motion. This is done systematically using a semi-analytic approach which is valid for small disturbances of the standing wave.

4.1.2 The stability analysis

The standing wave profiles satisfy a nonlinear system of differential equations which can be written abstractly as

$$\frac{\partial \underset{\sim}{u}}{\partial t} = \mathcal{N}(\underset{\sim}{u}), \tag{4.1.1}$$

where $\underset{\sim}{u}$ comprises the unknowns $\underset{\sim}{x}$, $\underset{\sim}{y}$ and $\underset{\sim}{\phi}$ and where $\mathcal{N}$ is a known nonlinear operator (its numerical approximation is described in the earlier chapters). To investigate the behaviour of perturbations to the known numerically-calculated exactly periodic solution $\underset{\sim}{u}^e$ begin by defining

$$\underset{\sim}{u} = \underset{\sim}{u}^e + \underset{\sim}{u}', \tag{4.1.2}$$

where $\underset{\sim}{u}'$ is a small perturbation. Substitute this into (4.1.1), linearising, and using the fact that $\underset{\sim}{u}^e$ satisfies (4.1.1) exactly to obtain

$$\frac{\partial \underset{\sim}{u}'}{\partial t} = \mathcal{L}\underset{\sim}{u}', \tag{4.1.3}$$

where $\mathcal{L}$ is the Jacobian of $\mathcal{N}$ with respect to $\underset{\sim}{u}$. This is a system of linear differential equations, with time dependent but periodic coefficients contained in $\mathcal{L}$, governing the evolution of any perturbation $\underset{\sim}{u}'$. Their behaviour will describe the dynamics of all motion which is nearly the standing waves.

Now use Floquet theory to determine how the perturbations develop in time (for an elementary introduction see Bender and Orszag (1978) §11.8). Let $\underset{\sim}{u}_i'(t)$ be a complete set of linearly independent solutions to (4.1.3). The general solution to (4.1.3) can be written as a linear combination of these linearly independent solutions, namely

$$\underset{\sim}{u}'(t) = \sum_i c_i \underset{\sim}{u}_i'(t). \tag{4.1.4}$$

After one period τ these linearly independent solutions at time $t+\tau$ must be able to be written as a linear combination of the solutions at time t, that is

$$\underset{\sim}{u}_i'(t+\tau) = \sum_j \alpha_{ij} \underset{\sim}{u}_j'(t). \tag{4.1.5}$$

The matrix then formed from the coefficients α_{ij}, $\mathcal{J} = [\alpha_{ij}]$, governs the evolution of all perturbations and so the eigenvalues of $\mathcal{J}$ gives the growth/decay multipliers of the perturbations and the eigenvectors corresponding to the unstable eigenvalues will give the unstable modes. If μ_i is the i^{th} eigenvalue of $\mathcal{J}$ then

$$\lambda_i = \frac{\log \mu_i}{\tau}, \tag{4.1.6}$$

is the average growth rate of the i^{th} eigenmode. Thus it is easy to determine the growth and decay of the perturbations to the standing wave: if the real part of λ_i is positive then the perturbations grow exponentially in time and hence are unstable; if it is zero then the perturbations are purely oscillatory; and if it is negative then the perturbations decay exponentially.

By defining the linearly independent solutions of (4.1.3) to be such that they are proportional to delta functions at time $t = 0$, that is

$$\left(\underset{\sim}{u}_i'(0)\right)_j = \epsilon\delta_{ij}, \tag{4.1.7}$$

where ϵ is a small number, then each column of the matrix $\mathcal{J}$ is found to be

$$\alpha_{ki} = \frac{1}{\epsilon}\left(\underset{\sim}{u}_i'(\tau)\right)_k, \tag{4.1.8}$$

where $\underset{\sim}{u}_i'(\tau)$ is found by numerically integrating (4.1.1) for one period starting with the perturbation given by (4.1.7).

4.2 Harmonic stability

Using the above method the harmonic stability of the previously calculated fundamental waves is investigated. It is ascertained whether or not the standing wave profile is stable or unstable to perturbations with a length scale the same as or less than the wavelength of the fundamental standing wave.

For all wave profiles with a crest acceleration less than 0.8886 ($h = 0.6167$) no harmonic instabilities were found. That is not to say they do not exist though, there may well be bubbles of instability for $A_c < 0.8886$ but the range of crest accelerations is expected to be narrow and the growth rates small. See Mackay and Saffman (1986), their crossing (ii), for a discussion of this type of instability for travelling waves. A more detailed investigation in the vicinity of any eigenvalue crossings would need to be performed to ascertain the exact nature and strength of any such instability. At $A_c = 0.8886$ there is a resonance between the fundamental wave and mode 4 harmonic leading to an instability. See Figures 4.1a (low modes)

and 4.1b (high modes) for plots of the eigenfrequency of each mode (the imaginary part of λ_i) versus the crest acceleration. The onset of this instability occurs at the energy maximum found earlier. This instability is expected as, from the theory of Saffman (1985), there will be an instability at the energy extrema.

Both $N = 64$ and $N = 128$ were used for the stability analysis. For all but large crest accelerations both the $N = 64$ and $N = 128$ calculations were in agreement. For large crest accelerations there were discrepancies between the calculations for the very high modes. Although the linearisation assumption of the analysis is still valid for large crest accelerations, as there are only small perturbations to the standing wave profile, for large crest accelerations the nonlinearity of the wave profile and the inability of a finite number of mesh points to accurately describe the wave profile leads to some computational error in the high modes. For large crest accelerations the $N = 128$ results were used and checked using $N = 256$ calculations for specific crest accelerations. The stability analysis was stopped at $A_c = 0.92$ due to discrepancies in the $N = 128$ and $N = 256$ calculations. To perform a stability analysis for larger crest accelerations $N = 256$ would have to be used and checked using $N = 512$. Clearly a different method for calculating the dynamics and stability of standing waves is needed close to the limiting profile.

4.3 Subharmonic stability

4.3.1 General analysis

Here the stability of standing waves to perturbations with a horizontal scale greater than the wavelength of the fundamental wave is investigated — the subharmonic stability. There exists precisely similar standing waves to those calculated in the previous section in which the waveheight and length are each reduced by a factor of m and the period by a factor of $\sqrt{m}$. I use m suitably scaled profiles over $[0, 2\pi]$ and perform precisely the same numerical analysis as for harmonic stability. This enables the determination of how small perturbations can interact among neighbouring waves and lead to instabilities. Using this analysis it is pos-

sible to calculate the stability of waves to perturbations which have a length scale up to m times that of the base wave. This technique is similar to that used by Longuet-Higgins (1978b) when studying the subharmonic stability of progressive gravity waves.

4.3.2 Side–band instabilities

Choosing $m = 8$ scaled replicas of the original profile, each with a wavelength $\frac{1}{8}^{th}$ of the original, it is possible to study perturbations with a length scale up to 8 times the wavelength of the fundamental wave. All calculations were performed with 64 mesh points per 8 scaled wavelengths for all wave steepnesses considered. That is 64 mesh points over $[0, 2\pi]$ which has 8 waves each with a wavelength $\frac{1}{8}^{th}$ of the original. They were checked using 32 mesh points and for specific wave steepnesses using 128 mesh points per 8 scaled wavelengths. Plotted in Figures 4.2a and 4.2b is the eigenfrequency of each mode versus the wave steepness. Figure 4.2a shows the long wavelength modes, the low wavenumber modes, labelled 1–15 and Figure 4.2b shows the shorter wavelength modes, the high wavenumber modes, labelled 16–31. The labelling is similar to Longuet-Higgins (1978b) Figure 5, where for example mode 7 corresponds to a perturbation with a wavelength $(8/7)^{th}$ of the fundamental wavelength. Figure 4.3 shows the real part of λ_i, the average growth rate of each of the unstable modes, versus h, the wave steepness. At $h = 0.093$ modes 7 and 9 coalesce to form an unstable mode which, with increasing wave steepness, restabilises at $h = 0.382$. Similarly modes 6 and 10 coalesce at $h = 0.199$ as do modes 5 and 11 at $h = 0.335$. There is evidence that the $(6, 10)$ instability will restabilise, as the $(7, 9)$ instability does, since the growth rate of the instability has reached its maximum for the wave steepnesses calculated here. The destabilisation of modes 7 and 9 near $h = 0.43$ is discussed later. These three instabilities are all side–band instabilities resulting from the interaction of the base wave, mode $m = 8$, with modes $m \pm \ell$, where ℓ is integral. It is expected that for higher wave steepness more of these side–band instabilities

will occur. For example the eigenfrequencies of modes 4 and 12 are nearing as the wave steepness is increasing and these will probably coalesce to form an unstable mode for a wave steepness higher than that examined here. The unstable region, resulting from these side–band instabilities, is shown in Figure 4.2a as the shaded region. The small amplitude shape could be given some asymptotic analysis. For any given wave steepness there appears to always be some unstable subharmonic mode.

4.3.3 Other instabilities

A different instability from this side-band instability is evident in the coalescence of modes 14 and 22. This gives rise to a short lived (in wave steepness) instability with an overall growth rate lower than the side-band instabilities. The $(14, 22)$ instability is a resonant triad interaction due to the integral linear combination of the mode numbers, $8+14 = 22$, coinciding with the same linear combination of the eigenfrequencies. This is a relatively strong instability. There are many apparent crossings of eigenfrequencies not all of which lead to instability. These crossings fall into the three categories as defined by MacKay and Saffman (1986): avoided crossings where the eigenfrequencies do not actually cross but avoid each other; bubbles of instability where the eigenvalues coalesce and move off the imaginary axis resulting in an instability; and crossings that do not interact. The exact nature of all the crossings here could be determined using the signature method as described by MacKay and Saffman. Some of the crossings may well be bubbles of instability but the range of wave steepnesses that they are unstable over must be very narrow except for the shown $(14, 22)$ bubble instability. The side–band instability is the dominant instability for all wave steepnesses considered.

4.3.4 Accuracy of calculations

Also plotted in Figure 4.2b are the eigenfrequencies for modes 2 and 3 from the harmonic stability analysis. These modes correspond to modes $16 = 2 \times 8$ and $24 = 3 \times 8$ respectively for the subharmonic stability analysis. For the

harmonic stability analysis 64 mesh points per wavelength were used whereas for this subharmonic stability analysis 8 mesh points per scaled wavelength were used. Therefore the subharmonic stability analysis is subject to a larger computational error than that found in the harmonic stability analysis as the wave profile is less well represented when using this fewer number of points. The discrepancy of the subharmonic mode 24 and the harmonic mode 3 for large steepnesses is a measure of this error. The computational error manifests itself as a non-physical instability in the short wavelength (high wavenumber) modes which is apparent in figure 4.2b. As the wave steepness is increased these high modes become unstable after their eigenfrequencies go to zero. The lower modes are still accurate even though there is this computational error leading to high mode instability. The maximum difference in the eigenfrequency of the subharmonic mode 16 and the harmonic mode 2 is less than 0.2% for $h = 0.5$. All modes less than 16 are well represented by this analysis for all the steepnesses considered. An exception to this is in the brief interaction of mode 25 with mode 7 near $h = 0.43$. This is thought to be due to computational error in mode 25 enabling it to interact with modes 7 and 9 and is not a physical destabilisation of modes 7 or 9. These modes restabilise once the eigenfrequency of mode 25 has reached zero.

Calculation was stopped at $h = 0.53$ due to the poor resolution of higher waves when using 8 mesh points per scaled wavelength. To calculate the subharmonic stability of higher (more extreme) profiles more mesh points would need to be used to accurately represent the 8 scaled replica profiles used over $[0, 2\pi]$. Computational power was a limiting factor here. These calculations were checked using 128 mesh points for specific wave steepnesses and found to be consistent. Shown on figure 4.3 are the growth rates of the corresponding unstable modes using $N = 128$, $h = 0.25$.

4.4 Conclusion and further work

4.4.1 Conclusion

The stability of standing waves to both harmonic and subharmonic perturbations was discussed. There are similarities between the stability of standing waves and that of progressive waves. Both are stable to harmonic perturbations except for steep waves, with possible narrow bubbles of instability and both are unstable to subharmonic perturbations. In accordance with the theory of Saffman (1985) there is a harmonic instability at the energy maximum. For any given wave steepness there is always some unstable subharmonic mode. In general the growth rate of the instability increases as the wave steepness increases.

4.4.2 Further work

An obvious area for extension is to increase the number of mesh points used over $[0, 2\pi]$, thereby reducing the computational errors in both the harmonic and subharmonic stability analyses. This of course comes at the expense of an increase in computational effort. For the subharmonic case increasing the number of mesh points used allows two areas of extension. Firstly, the same number of scaled replicas can be used ($m = 8$ in this case) with more points used per replica enabling the subharmonic stability of more extreme standing waves to be determined. The second is to increase the number of replicas used and therefore allowing more modes and their interactions to be calculated. It is expected that more of the side–band instabilities would be found and probably more interactions like the $(14, 22)$ instability. Using the signature method of Mackay and Saffman (1986) and a more detailed analysis near the eigenvalue crossings, the type of crossing could be determined. Whether they are avoided crossings or bubbles of instability would be of interest.

It would be straightforward to use this method to calculate the stability of standing waves on water of a finite depth as calculated in Chapter 3, the major constraints being the large parameter space and computational time. It is expected

that standing waves on finite depth water would exhibit similar properties to standing waves on infinite depth water but modified by the resonant depths. A stability analysis near the depths at which the dominant harmonic resonances occur may well give new insight into the dynamics of the standing waves near these resonant depths.

The stability analysis used here is restricted to two-dimensional perturbations. In a similar manner to travelling waves, McLean (1982), it is expected that the dominant instability for extreme standing waves would be three-dimensional. The experimental work of Taylor (1953a), his figures 19 and 20 in particular, certainly suggests that this is the case. A three-dimensional stability analysis of the extreme standing waves would need to be performed to clarify the nature of any instabilities and to determine the associated growth rates.

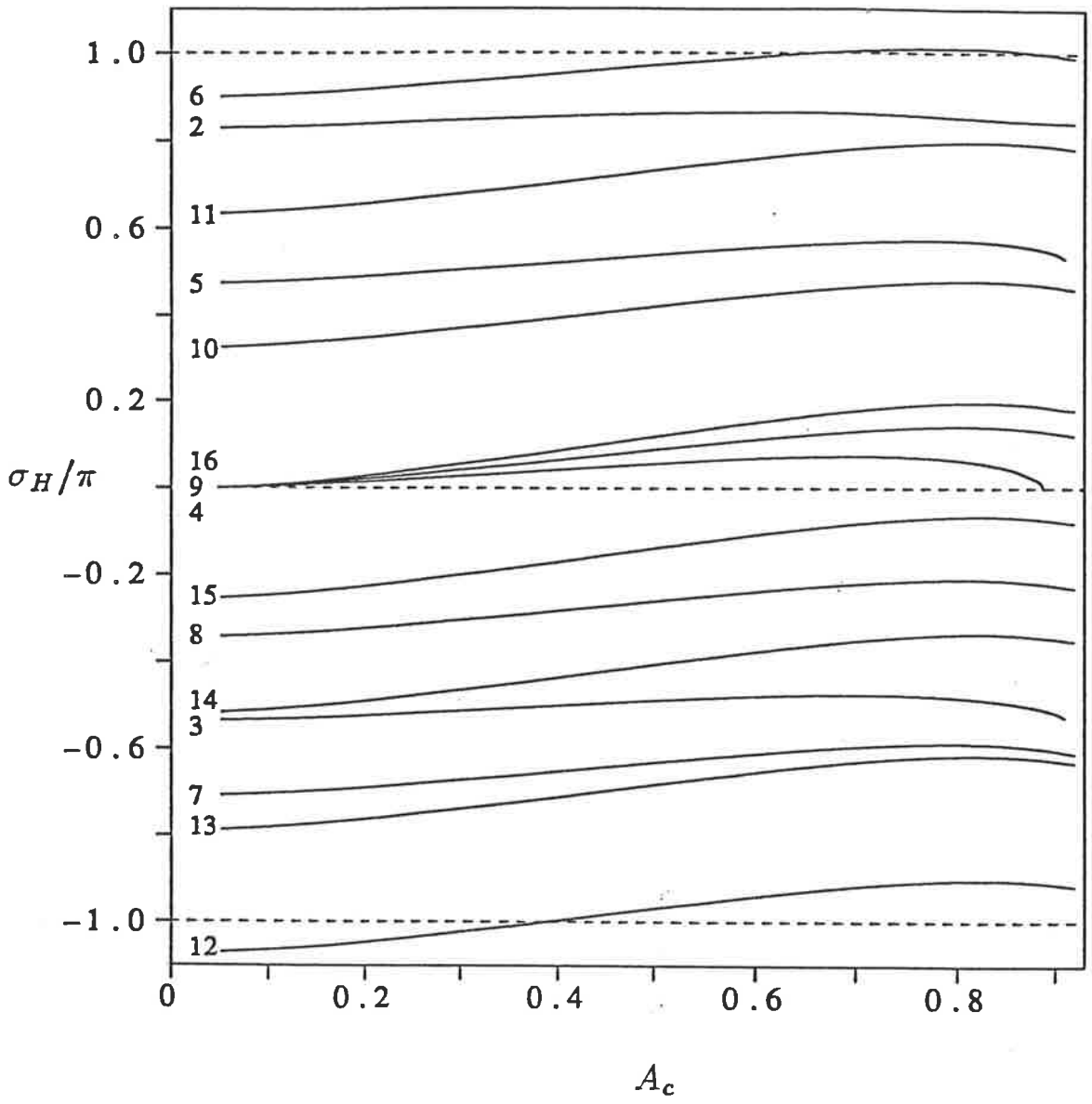

Figure 4.1: (a) Harmonic stability analysis, eigenfrequencies, σ_H, of the low wavenumber modes versus crest acceleration, showing the instability at $A_c = 0.8886$ (mode 4).

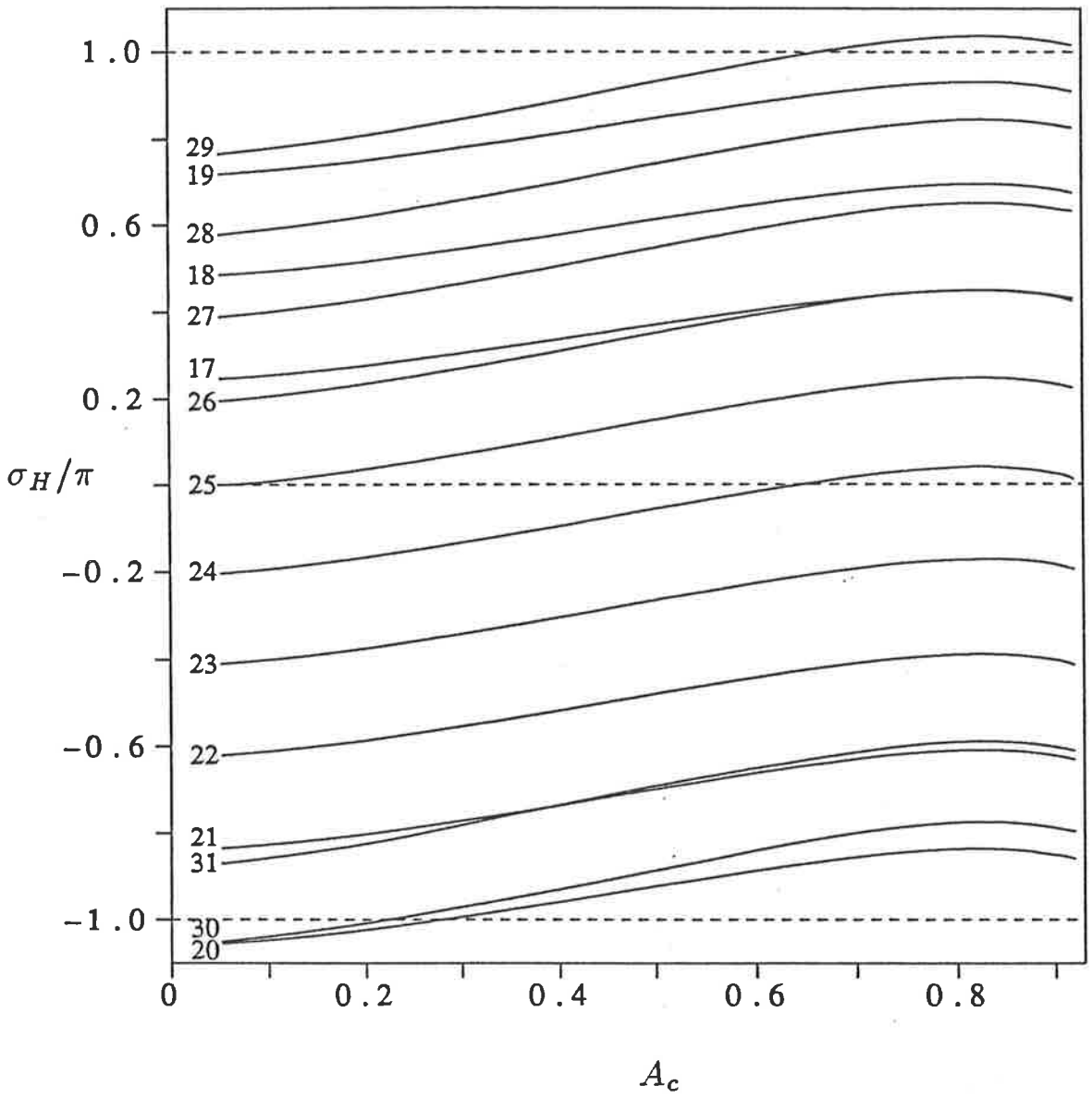

Figure 4.1: (b) Eigenfrequencies of the high wavenumber modes versus crest acceleration. Showing mode 24 crossing zero.

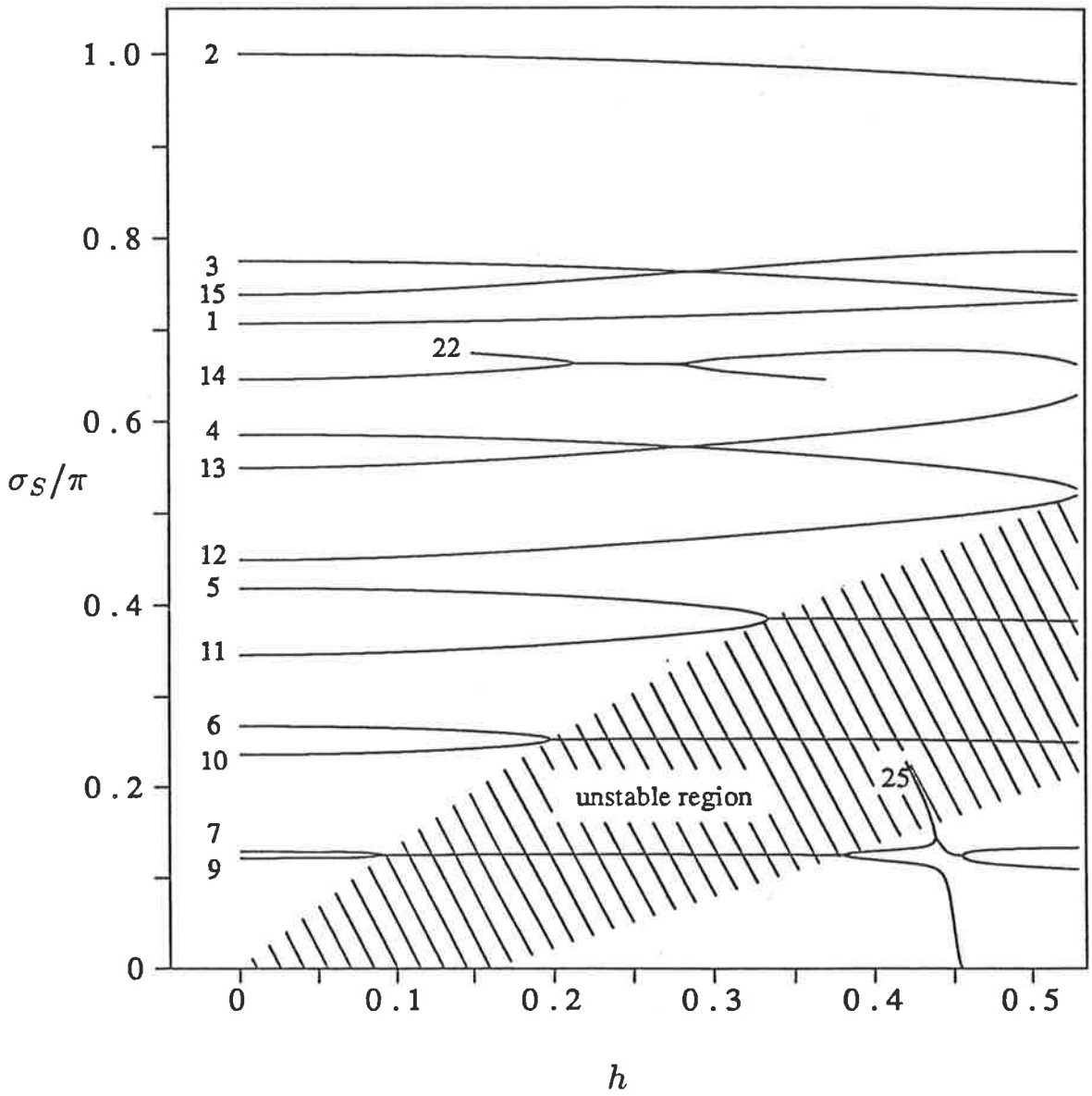

Figure 4.2: (a) Subharmonic stability analysis, eigenfrequencies, σ_S, of the low wavenumber modes versus wave steepness of the fundamental wave, using $N = 64$, $m = 8$. The shaded region is the unstable region due to side–band instabilities.

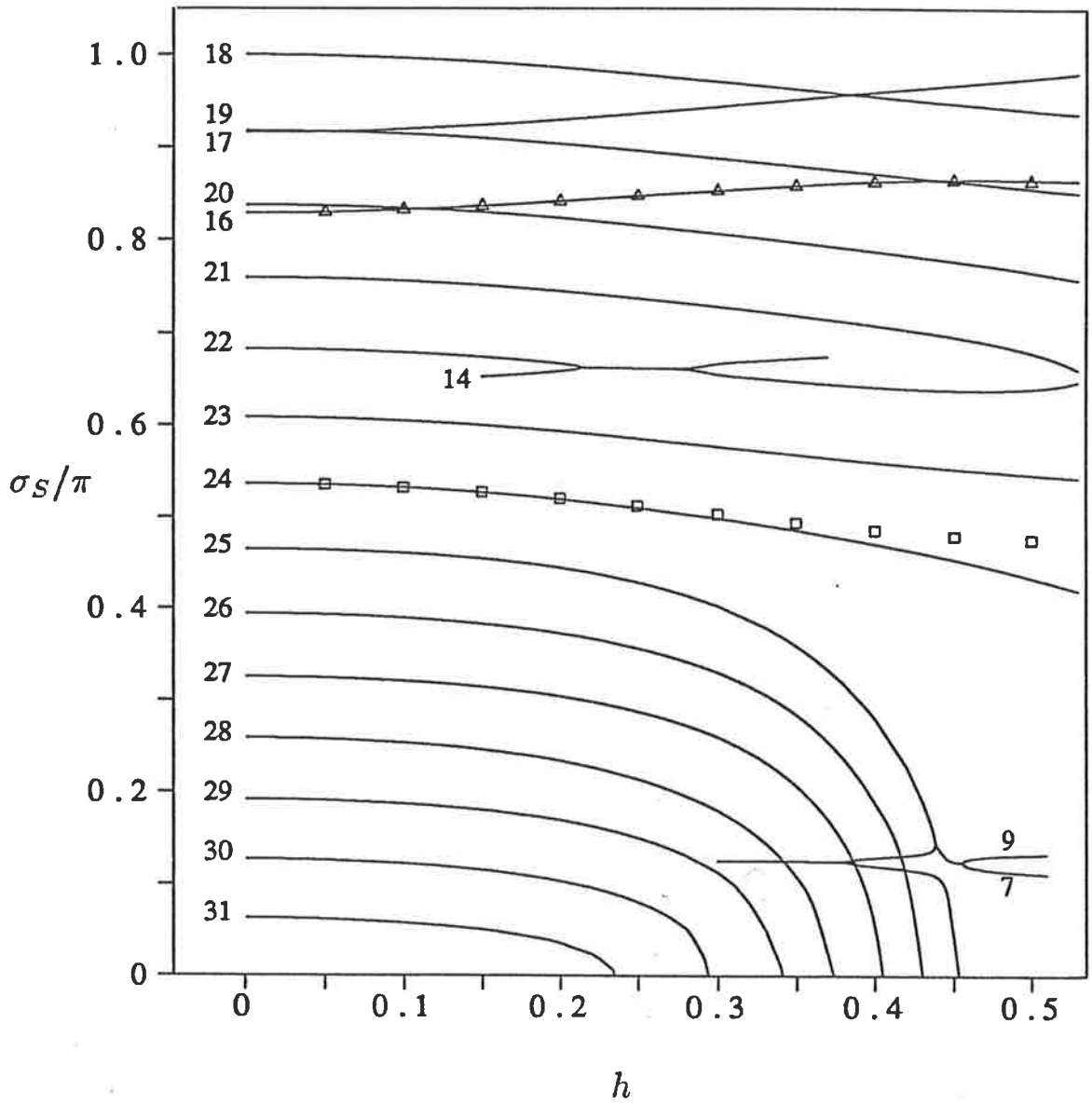

Figure 4.2: (b) Eigenfrequencies of the high wavenumber modes versus wave steepness of the fundamental wave. Also shown are two modes from the harmonic stability analysis $\triangle$: $N = 64$ harmonic mode 2; $\square$: $N = 64$ harmonic mode 3.

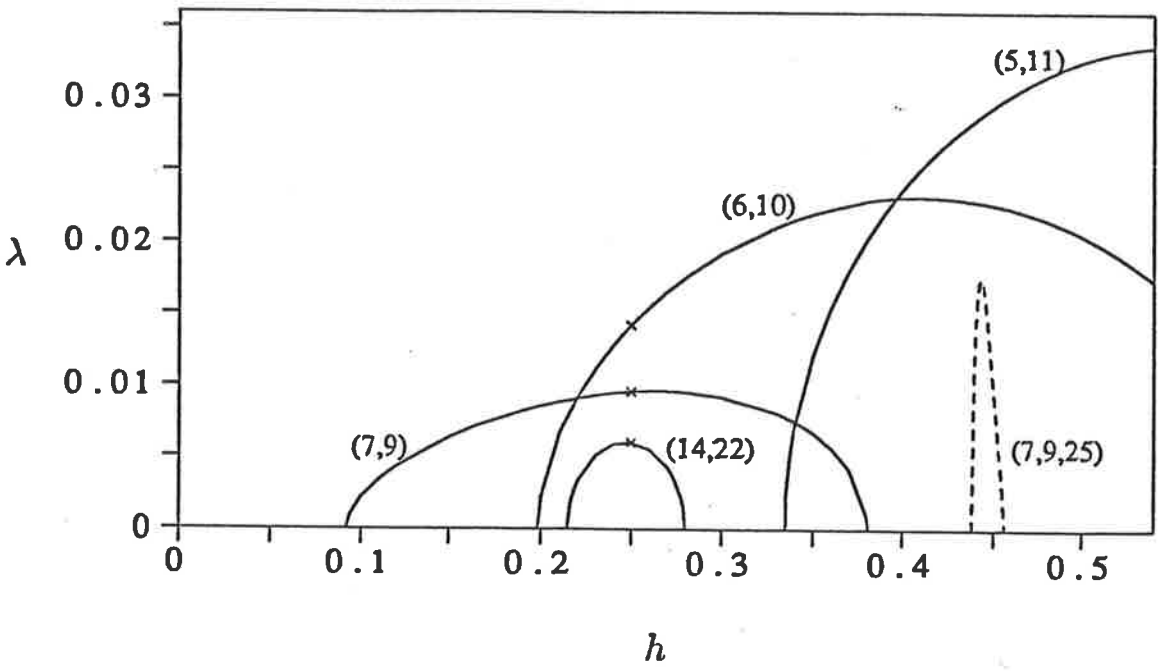

Figure 4.3: Average growth rate, λ, of the unstable modes versus the wave steepness of the fundamental wave $N = 64$. $\times$ are for $N = 128$, $h = 0.25$. The $(7, 9, 25)$ instability is shown dashed as it is unphysical.

PART TWO

SHEAR DISPERSION

CHAPTER 5
INTRODUCTION

In this second part of this thesis I will consider the dispersion of a passive contaminant in channels and pipes. The majority of the work presented here has been published in Mercer and Roberts (1990) for the channel case and presented in Mercer and Roberts (1992b, 1992c) for the pipe case. When a contaminant is first released into a channel or pipe it spreads across the channel or pipe and is advected downstream at the different rates of the velocity profile. This ensures that the distribution of contaminant is soon relatively smooth. Once the contaminant has reached a smooth state downstream of the pollutant source its concentration evolves relatively slowly. The long–term evolution of a passive contaminant released into a straight channel or pipe will eventually be governed by an appropriate advection–diffusion equation, where the effective diffusion coefficient is obtained from the addition of the longitudinal dispersion and shear dispersion coefficients. This slow evolution is precisely the type of situation to which centre manifold theory may be applied. I will not provide a synopsis of centre manifold theory here, see Carr (1981) for an excellent introduction.

Centre manifold theory, and the related invariant manifold theory, have been used in a variety of other areas in mechanics including: the instabilities and chaos which occur in Couette-Taylor flow, see Chossat and Iooss (1985) and Laure and Demay (1988); the dynamics of convection, see Roberts (1991a); the dynamics of viscous fluid flow, see Chang and Chen (1986), Chang (1989), Hwang and Chang (1989) and Renardy (1989); the analysis of the Kuramoto–Sivashinsky equation which is used to model flame fronts, directional solidification and weak two–dimensional turbulence, see Armbruster *et al.* (1989), Foias *et al.* (1985, 1988) and Oats and Roberts (1992); elasticity of beams and rigid bodies, see Mielke (1988, 1991) and Roberts (1992) to name but a few of the many and varied applications of this theory.

Initially for both the channel and pipe cases I will derive high order models of the longitudinal dispersion of a passive contaminant in Poiseuille flow using centre manifold theory. Similar approximations for either the channel or pipe cases can be obtained by using the integral moments, see Aris (1956), or an asymptotic series analysis, as given by Chatwin (1970). A multiple scales approach has been used by Pagitsas, Nadim and Brenner (1986) while Gupta and Bhattacharya (1983) used a probabilistic approach. More recently Stokes and Barton (1990) used an eigenvalue method incorporating Laplace and Fourier transforms. One advantage of this centre manifold approach is the ease with which these high order approximations are derived, as once the problem has been formulated in a centre manifold framework it is a purely mechanistic process to obtain approximations to any desired order of accuracy — limited only by computational power.

In Chapter 6 shear dispersion in channels is considered. I study the dispersion of a contaminant in a two–dimensional channel and so the governing equation is the two–dimensional advection–diffusion equation. The two–dimensional channel serves as a model of the depth–averaged equations for dispersion in flowing water bodies that are relatively shallow, such as flow in rivers or estuaries. The basic assumption is that the solution is slowly varying in x, that is, the small parameter of the problem is $\partial/\partial x$ or, equivalently, the wavenumber k. I derive a 24^{th} order model for the evolution of the mean concentration of contaminant and indicate the range of validity of the approximation by showing the sequence of asymptotic approximations actually converge.

One of the powers of this centre manifold approach is the ease with which generalisations can be incorporated into the centre manifold framework. I consider the problem of dispersion in a varying channel flow with a plane Poiseuille velocity profile (which is appropriate if the diffusion of momentum is significantly faster than the diffusion of contaminant, and in any case serves as a model for other velocity profiles). I let the sides of the channel be a slowly varying function along

the stream, the flux of the fluid be a slowly varying function of time and the diffusivity be a slowly varying function of both space and time. The effects of the space– and time–variable diffusivity can be used to model swirl flow associated with bends in channels and pipes or areas of turbulence. I investigate the effect that such varying flow properties have upon the asymptotic equation describing the long–term dispersion of the contaminant. In particular I address the outstanding problem, as noted by Chatwin and Allen (1985), of what modifications should be made to the advection–diffusion equation when the cross–sectional area and flow properties are not constant. By rewriting the evolution equation in a conservative form the memory effect of the dispersion process is also highlighted.

Chapter 7 is concerned with shear dispersion in pipes. The initial analysis is similar to the channel case except the three-dimensional non–axisymmetric advection–diffusion equation is used with an axisymmetric Poiseuille velocity profile. Again a 24^{th} order model is derived and its validity is discussed. A quantitative limit of resolution for high order Taylor models of shear dispersion in pipes is derived.

I formulate a conservative, non–negative finite difference scheme which matches the evolution equation to a predetermined order of accuracy. The limitations imposed on such a numerical scheme by considering the higher order approximations to the evolution equation are discussed.

The appropriate initial condition to be used for the Taylor model of shear dispersion in a pipe is determined within a centre manifold framework. The commonly used initial condition, which consists of simply taking the cross–sectional average of the exact initial condition, is shown to be just a first approximation to the correct initial condition. Corrections are found which have to be used so that the model partial differential equation accurately models the evolution of the exact solution. Using the correct initial condition it is possible to predict the observed phenomena of centroid displacement and variance deficit. This was previously not

possible within the Taylor model.

Centre manifold theory also provides a framework for the derivation of asymptotically correct boundary conditions for these simplified models of dispersion. I calculate the appropriate inlet and outlet boundary conditions for a pipe of finite length. The outlet boundary condition is compatible with the exit boundary condition derived by Smith (1988). These boundary conditions at the inlet and outlet may be derived such that the solution of the model differential equation is consistent with the exact solution to an arbitrarily high order of accuracy.

In a similar manner as in Chapter 6 for the channel case, I generalise within the centre manifold framework to include a slowly varying pipe radius along the stream and a flux which varies slowly with time. These generalisations are easily incorporated into the centre manifold framework whereas previous methods cannot accommodate such generalisations. The resultant modifications to the advection velocity and effective dispersion coefficient are calculated.

CHAPTER 6

SHEAR DISPERSION IN CHANNELS

6.1 Constant cross–section

6.1.1 Formulation

I begin by studying the dispersion of solute in a constant width channel which has boundaries given by $y = \pm b$. See Figure 6.1 for a schematic diagram. As the starting point for the analysis take the two–dimensional advection–diffusion equation

$$\frac{\partial c}{\partial t} + \nabla \cdot (\mathbf{q}c) = \nabla \cdot (\kappa \nabla c). \tag{6.1.1}$$

Here κ is the diffusivity (assumed constant in this section but this restriction will later be relaxed), c is the concentration of solute and $\mathbf{q}$ is a given velocity profile. The fluid is assumed incompressible and the advection velocity is taken to be solely in the the x direction (along the channel) but varying with y (across the channel); that is, the velocity field is

$$\mathbf{q} = u(y)\mathbf{i}. \tag{6.1.2}$$

This is subject to the condition that there is no flux of solute through the boundaries which for a straight channel just gives

$$\frac{\partial c}{\partial y} = 0 \quad \text{on} \quad y = \pm b. \tag{6.1.3}$$

By noting that the dominant mechanism of cross–channel diffusion in equation (6.1.1) is represented by the $\partial^2 c/\partial y^2$ term I can rewrite equation (6.1.1) in the form

$$\mathcal{L}c = \frac{\partial c}{\partial t} + u(y)\frac{\partial c}{\partial x} - \kappa \frac{\partial^2 c}{\partial x^2}, \tag{6.1.4}$$

where $\mathcal{L}$ is the operator defined by

$$\mathcal{L}c = \kappa \frac{\partial^2 c}{\partial y^2}. \tag{6.1.5}$$

As is well known (Taylor (1953b)), the combined effects of advection and diffusion smooth the concentration c until it reaches a stage where it is nearly

constant across the channel at any station x and slowly varying along the channel. The concentration then evolves relatively slowly as the contaminant spreads along the channel while maintaining a state of near constant concentration across the channel. This is a relatively simple state of the full system and a good measure of the detailed distribution of the contaminant is simply its cross–sectionally averaged concentration. Thus the long term evolution of the contaminant is primarily given by the evolution of this averaged concentration. This is precisely the sort of situation to which centre manifold theory may be applied, see Carr (1981).

6.1.2 The rigorous centre manifold approach

Centre manifold theory cannot yet be applied both rigorously and directly to the above equations. However, if I take the Fourier transform of the equations with respect to x, then the state of having only slow variations with respect to x corresponds to small wavenumber k. The wavenumber thus turns out to be the small parameter in this problem.

Taking the Fourier transform of (6.1.4) and denoting transformed quantities by $\hat{}$ I find

$$\mathcal{L}\hat{c} = \frac{\partial \hat{c}}{\partial t} + iku(y)\hat{c} + \kappa k^2 \hat{c}. \tag{6.1.6}$$

Now I am only interested in small wavenumbers k, that is, slowly varying solutions so I adjoin the equation

$$\frac{\partial k}{\partial t} = 0 \tag{6.1.7}$$

to equation (6.1.6). This allows the application of centre manifold theory to the system (6.1.6) and (6.1.7) by treating the terms $k\hat{c}$ and $k^2\hat{c}$ as "nonlinear" terms.

It has been shown, Mercer and Roberts (1990) §2.1, that this system is now in a form where centre manifold theory can be applied directly. Rather than follow this rigorous approach I choose not to transform to Fourier space. Hence the following derivation is not directly rigorous though it can be made so by transforming into Fourier space. The benefit of not transforming into Fourier space is that I will always deal with familiar physical variables and it can be more

easily generalised to cope with practical complexities which are discussed in later sections.

From Mercer and Roberts (1990) the centre manifold is reached exponentially quickly in a time which is estimated by the least negative eigenvalue of $\mathcal{L}$ which is $\gamma = \kappa\pi^2/(4b^2)$. Therefore the state of balance of being on the centre manifold is attained in a cross–channel diffusion time b^2/κ.

6.1.3 The formal centre manifold approach

Applying the formal centre manifold procedure, see Roberts (1988), I assume that the concentration c may be described by

$$c = V[y, C], \tag{6.1.8}$$

where C is the cross–sectionally averaged concentration of solute and its evolution in time, and indirectly that of c, is described by

$$\frac{\partial C}{\partial t} = G[C]. \tag{6.1.9}$$

In (6.1.8) and (6.1.9) the square brackets are used to denote a functional dependence in x upon not only the argument C but also upon its slow derivatives with respect to x. For example: $G[C]$ indicates that G depends upon C, $\partial C/\partial x$, $\partial^2 C/\partial x^2$, ...

I substitute the asymptotic expansion

$$c = V[y, C] \sim \sum_{n=0}^{\infty} v_n(y)\frac{\partial^n C}{\partial x^n} \quad \text{such that} \quad \frac{\partial C}{\partial t} = G[C] \sim \sum_{n=1}^{\infty} g_n \frac{\partial^n C}{\partial x^n} \tag{6.1.10}$$

into (6.1.4) and equating all terms of the same order obtain the sequence of equations

$$\begin{aligned} \mathcal{L}v_0 &= 0 \\ \mathcal{L}v_1 &= v_0 g_1 + u(y)v_0 \\ \mathcal{L}v_n &= \sum_{\ell=1}^{n} v_{n-\ell} g_\ell + u(y)v_{n-1} - \kappa v_{n-2}, \quad n = 2, 3, \cdots. \end{aligned} \tag{6.1.11}$$

Observe that the expansion in (6.1.10) is linear in C, this is consistent as the original problem (6.1.1)–(6.1.3) is linear. If there were nonlinear reactions involving the contaminant, for instance chemical reactions, then the asymptotic expansions would have to be of a more general form.

Solving the first equation of (6.1.11), subject to the boundary conditions, I obtain

$$v_0 = 1. \tag{6.1.12}$$

Substituting (6.1.12) into the second equation of (6.1.11) I obtain the equation

$$\mathcal{L}v_1 = g_1 + u(y). \tag{6.1.13}$$

Integrating this across the channel and using the boundary conditions $\frac{\partial v_1}{\partial y} = 0$ on $y = \pm b$ I find

$$g_1 = -U, \tag{6.1.14}$$

where U is the cross–sectionally averaged advection velocity.

Substituting this into (6.1.8) and (6.1.9) I then obtain the first approximation

$$c(x, y, t) = C(x, t) \quad \text{where } \frac{\partial C}{\partial t} + U\frac{\partial C}{\partial x} = 0. \tag{6.1.15}$$

The evolution of C is thus governed by just the simple advection equation giving that the cross–sectionally averaged concentration advects with the mean velocity of the fluid flow. This is of course the commonly used first approximation for channel flows of this type. One of the failings of the pure advection model (6.1.15) is that it is structurally unstable; that is any small change to the equation may (in time) produce a large change to the solution. Taylor (1953b) derived an appropriate diffusive correction to (6.1.15) via heuristic arguments to obtain a structurally stable approximation.

To proceed further by the centre manifold approach it is simply a matter of solving the equations (6.1.11) in succession, using the boundary conditions and the additional constraint that the cross–sectional averages of the v_n's must be zero (for

$n = 1, 2, \ldots$). The right–hand side of (6.1.11) incorporates all the other physical mechanisms of the full problem. These interact through the hierarchy of the equations and hence the heuristic arguments of Taylor are not needed in deriving this approximation. It is simpler to calculate the higher order approximations if I fix upon a particular velocity profile. As a simple model for actual velocity profiles that occur in rivers and channels I will choose the plane Poiseuille flow

$$u(y) = \frac{3}{2}U\left(1 - Y^2\right), \tag{6.1.16}$$

where $Y = y/b$ is a nondimensional distance from the mid–channel. Proceeding as prescribed above I find successive asymptotic contributions to V and G by solving (6.1.11) and obtain

$$\begin{aligned} v_1 &= -\frac{Ub^2}{120\kappa}\left(15Y^4 - 30Y^2 + 7\right) \\ g_2 &= \kappa + \frac{2U^2b^2}{105\kappa} \\ v_2 &= \frac{U^2b^4}{201600\kappa^2}\left(675Y^8 - 2940Y^6 + 3570Y^4 - 1020Y^2 - 29\right). \end{aligned} \tag{6.1.17}$$

So to second order I find that the evolution of the mean concentration is approximated by

$$\frac{\partial C}{\partial t} \sim -UC' + \left(\kappa + \frac{2U^2b^2}{105\kappa}\right)C''. \tag{6.1.18}$$

Comparing these to the work of Smith (1981) in his Section 8 where he studies shear dispersion of plane Poiseuille flow between plates of separation $2d$, I see that these second order approximations are exactly the ones he derives in his equations (8.8) and (8.9) for the shape function and dispersion coefficient. The functions $v_1(y)$ and $v_2(y)$ given in (6.1.17) show how the details of the concentration distribution are modified by the large–scale gradients along the channel.

6.1.4 High order approximations

I now wish to ascertain the range of validity of the approximations for Poiseuille flow and determine whether or not a finite truncation of the evolution equation is justified. This is relevant as (6.1.18) is frequently used to predict

contaminant dispersion in rivers and channels. It is therefore important to be able to estimate over what length–scale such truncation of the full equations is valid. The evolution equation can be written in the form

$$\frac{\partial C}{\partial t} = -U\frac{\partial C}{\partial x} + D\frac{\partial^2 C}{\partial x^2} + \frac{\kappa}{b^2}\sum_{n=3}^{\infty} A_n (bP_e)^n \frac{\partial^n C}{\partial x^n}, \tag{6.1.19}$$

where

$$D = \kappa + \frac{2U^2 b^2}{105\kappa}, \tag{6.1.20}$$

is the effective dispersion coefficient, the A_n's are the numerical coefficients obtained from the g_n's, and $P_e = Ub/\kappa$ is a Peclet number. This is a higher order Taylor model of shear dispersion. It has been derived by a number of workers, but usually in a more complicated form involving time dependent coefficients, see Gill and Sankarasubramanian (1970, 1971) and De Gance and Johns (1978) for example. The time–dependent coefficients appearing in the above papers are primarily needed to predict physical features in the dispersion which, from a centre manifold point of view, can be predicted by supplying the evolution equation (6.1.19) with the appropriate initial condition. This will not be discussed here, see Mercer and Roberts (1990) §2.3 for a detailed discussion of the appropriate initial condition for the Taylor model of dispersion in channels. The initial condition for models of dispersion in pipes is discussed in Chapter 7.

Taking the Fourier transform of this equation with respect to x I obtain

$$\frac{\partial \hat{C}}{\partial t} = \left(-Uik + D(ik)^2 + \frac{\kappa}{b^2}\sum_{n=3}^{\infty} A_n \left(P_e\, ikb\right)^n\right)\hat{C}, \tag{6.1.21}$$

where $\hat{C}$ is the Fourier transform of C. What is of interest is the convergence or otherwise of the power series with coefficients A_n. If this power series is divergent then I will have shown that a finite truncation of the evolution equation can at best be an asymptotic description of the evolution of the system. Alternatively, if the power series converges then the evolution equation (6.1.19) is convergent for sufficiently smooth distributions of contaminant and hence a useful approximation

to the evolution can be obtain by truncating this equation at some finite order. Also, from the radius of convergence, some idea of the length–scale in which the original assumption, that $\frac{\partial}{\partial x}$ is a "small quantity", is valid can be obtained.

Calculating the coefficients A_n up to the 24^{th} order, using the computer algebra package REDUCE, I find that they approximately follow the pattern of signs $++--+--\ldots$ which indicates that the radius limiting singularity is close to the imaginary axis. The first seven coefficients are

$$A_3 = 2.3088 \times 10^{-4},$$

$$A_4 = -2.8416 \times 10^{-5},$$

$$A_5 = -1.0523 \times 10^{-6},$$

$$A_6 = 8.3626 \times 10^{-8},$$

$$A_7 = 5.6525 \times 10^{-9},$$

$$A_8 = -2.7333 \times 10^{-10},$$

$$A_9 = -3.1659 \times 10^{-11}.$$

By examining a model function whose power series has a similar behaviour, and hence a similar singularity, it is possible to determine the position in the complex (ik)-plane of the convergence limiting singularity. The details of this are described in the appendix of Mercer and Roberts (1990). Figures 6.2(a), (b) show the results of this comparison. From these plots the radius of convergence in the $(ikbP_e)$–plane is $R_c = 11.8$ and the angle from the real axis of the conjugate pair of singularities is $\theta = \pm 82°$.

The power series (6.1.21) will converge if the only non-zero Fourier components satisfy

$$|bP_e k| < R_c. \tag{6.1.22}$$

Recognizing that k is equivalent to $2\pi/L$ where L is a typical small longitudinal length in the original problem rearrange (6.1.22) to obtain

$$L > \frac{2\pi P_e}{R_c} \simeq \left(\frac{P_e}{1.9}\right) b. \tag{6.1.23}$$

So, provided the smallest longitudinal length–scale of the problem satisfies (6.1.23), the asymptotic series (6.1.19) is convergent and a finite truncation of this equation is justified. It should be noted that because the convergence limiting singularity is in the complex plane it has no direct physical significance to the original problem. Also, the convergence of the series does not guarantee that a given truncation of (6.1.19) will lead to a concentration that is always nonnegative.

For the approximations to be valid, flows with large Peclet number need to vary over a large length–scale. The smaller the Peclet number, the faster the solution can evolve over the same length of channel. The limitation given by (6.1.23) should be recognized by practitioners working in the field of contaminant dispersion. A *qualitative* version of this limitation has been known for a long time, see Taylor (1953b, 1954). However, this is the first *quantitative* estimate for the length–scales in this sort of problem. For length–scales not satisfying (6.1.23), a finite truncation of the evolution equation does not necessarily model features of the contaminant dispersion. Care must be taken when considering these types of dispersion problems that the resolved length–scales are not too small.

6.2 Varying properties

6.2.1 The asymptotic scheme

As noted by Chatwin (1980) the often used Taylor approximation for dispersion problems does not hold when the channel is not of a constant cross–section. I will systematically derive approximate equations that are valid when the cross–section, flux and diffusivity all vary. This centre manifold approach thus provides the methodology to appropriately model dispersion with such variations, an outstanding problem according to Chatwin and Allen (1985).

Whereas previously the sides of the channel were parallel, I will now let them be $y = \pm b(x)$ where $b(x)$ is a slowly varying function of x; that is, a derivative of b with respect to x is also considered to be a "small quantity". The flow flux is allowed to be a slowly varying function of time and hence a derivative of the flux

with respect to t is likewise considered to be a "small quantity". The previous restriction of constant diffusivity κ is also relaxed, and κ is now considered a slowly varying function of space and time, although constant across the channel. These are collectively called "variations in the media", as in essence they are variations in the coefficients of the problem. I am interested in the effect that such variations in the media have upon the centre manifold and the evolution on it, and hence in the effect of such variations upon the long–term dispersion of the contaminant. I will primarily restrict my attention to the effect the media variations have upon the mean advection and shear dispersion of the contaminant as these are the dominant processes modelled in many applications.

The dispersion of a contaminant in an estuary is one example where the effects of the varying media are very important. An estuary has a varying cross–section due to the widening or narrowing of the estuary. Tidal fluctuations also introduce a flux variation which will alter the dispersion of any contaminant. Changes in the velocity of the flow also alters the local turbulence which will in turn alter the turbulent diffusivity. To be able to accurately model dispersion of a contaminant in an estuary all these factors should be taken into account. Here I derive the necessary approximations to be used for the case of channel flow; in practical calculations the overall approach will be the same, it will just be the details which will differ.

To simplify the analysis I choose to exclude the longitudinal diffusion terms and retain only the cross–stream diffusion term represented in equation (6.1.1) by $\kappa \frac{\partial^2 c}{\partial y^2}$. The velocity profile is no longer solely longitudinal, but has a transverse component due to the effect of the varying width of the channel. I will consider quasi–Poiseuille flow in the channel, the stream function for the velocity profile is given by

$$\psi = \frac{F(t)}{4}\left(3Y - Y^3\right), \tag{6.2.1}$$

where $F(t)$ is the flux of the advecting fluid, and $Y = y/b(x)$ is a scaled cross–

stream coordinate. For the case of a constant width channel and constant flux, this reduces to exactly the plane Poiseuille flow considered in the previous section with the flux $F = 2Ub$.

Equation (6.1.1) now becomes

$$\mathcal{L}c = \frac{\partial c}{\partial t} + u\frac{\partial c}{\partial x} + v\frac{\partial c}{\partial y}. \tag{6.2.2}$$

Where $\mathcal{L}$ is again defined by (6.1.5) and u and v are the velocity components in, respectively, the x and y directions, which from the stream function are

$$u = \frac{3F}{4b}\left(1 - Y^2\right) \quad ; \quad v = -\frac{3Fb'}{4b}\left(Y - Y^3\right). \tag{6.2.3}$$

In the general case, where longitudinal diffusion is included, the boundary condition would be

$$\frac{\partial c}{\partial \mathbf{n}} = 0 \quad \text{on} \quad y = \pm b(x), \tag{6.2.4}$$

where $\mathbf{n}$ is the outward normal to the boundary. However, since I have chosen to ignore the x component of diffusion in order to conserve contaminant, the boundary condition remains (6.1.3).

As I am dealing with quantities assumed to be varying slowly in space and time, I now assume that $\frac{\partial}{\partial x}$ and $\frac{\partial}{\partial t}$ are "small quantities". I apply the centre manifold ansatz (6.1.8) and (6.1.9) including the variations in the media, and seek an asymptotic approximation of the form

$$c = V[y, C] \sim \sum_{n=0}^{\infty} V^n[y, C] \quad \text{such that} \quad \frac{\partial C}{\partial t} = G[C] \sim \sum_{n=1}^{\infty} G^n[C]. \tag{6.2.5}$$

In these asymptotic sums each term V^n and G^n contains all the terms of order n; that is, it contains all terms that have a total of precisely n space–time derivatives.

Substituting (6.2.5) into the governing equation (6.2.2) and equating terms of the same order, I obtain the system of equations

$$\begin{aligned} \mathcal{L}V^0 &= 0 \\ \mathcal{L}V^n &= \sum_{\ell=0}^{n} \frac{\partial V^{n-\ell}}{\partial C} G^\ell + u\frac{\partial V^{n-1}}{\partial x} + v\frac{\partial V^{n-1}}{\partial y} \quad n = 1, 2, \cdots, \end{aligned} \tag{6.2.6}$$

where $\frac{\partial}{\partial C}$ is a Frechet derivative which depends not only on C but also its derivatives with respect to x. These equations can be solved in succession to obtain V^n and G^n to any desired order.

6.2.2 Correction to the advection velocity

Solving these equations for the first correction I obtain the centre manifold to be

$$\begin{aligned} c &\sim V^0 + V^1 + V^2 \\ &= C - \frac{\xi}{120}\left(15Y^4 - 30Y^2 + 7\right)C' \\ &\quad + \frac{\left(\xi^2\right)'}{403200}\left(675Y^8 - 3780Y^6 + 7770Y^4 - 6900Y^2 + 1211\right)C' \\ &\quad - \frac{\tau\dot{\xi}}{5040}\left(21Y^6 - 105Y^4 + 147Y^2 - 31\right)C' \\ &\quad - \frac{\xi^2}{201600}\left(675Y^8 - 2940Y^6 + 3570Y^4 - 1020Y^2 - 29\right)C'' \end{aligned} \tag{6.2.7}$$

where

$$\tau = \frac{b^2}{\kappa} \quad \text{and} \quad \xi = \frac{Fb}{2\kappa}, \tag{6.2.8}$$

and where differentiation with respect to time is denoted by an overdot and spatial derivatives by a prime. τ is a cross–channel diffusion time and ξ is a downstream advection distance in a cross–channel diffusion time. These two quantities are the basic variables of shear dispersion and most of the results will be expressed in terms of them. The first two terms and the last term of (6.2.7) are just the non-varying terms calculated in Section 6.1. The effects of the variations in the media on the concentration of the contaminant can be seen in the third and fourth terms of the right–hand side of (6.2.7).

The evolution of the cross–sectionally averaged concentration along this centre manifold is found to be given by

$$\begin{aligned} \frac{\partial C}{\partial t} &\sim G^1 + G^2 \\ &= -\frac{F}{2b}C' + \frac{F^2}{210\kappa}C'' + \left[\frac{b'F^2}{210b\kappa} - \frac{F^2\kappa'}{210\kappa^2}\right]C', \end{aligned} \tag{6.2.9}$$

where $F/2b = U$ the cross–sectionally averaged velocity. This equation can be rewritten as

$$\frac{\partial C}{\partial t} \sim -\frac{\xi}{\tau}\left(1 - \frac{2}{105}\xi'\right)C' + \frac{2}{105}\frac{\xi^2}{\tau}C''. \tag{6.2.10}$$

Here the main effect which the varying cross–section and diffusivity has upon the advection of the cross–sectionally averaged concentration can be seen. (This provides information on how the averaged concentration of the contaminant evolves along the channel, but in its present form does not directly indicate how the actual contaminant material is evolving. This is treated in Section 6.2.4 where I consider the conservative form of the equations and investigate how the density of the contaminant evolves along the channel.) The advection velocity, $U = \xi/\tau$, is modified by the factor $(1-(2/105)\xi') = [1-(F/105)(b/\kappa)']$, so that if the channel is slowly widening downstream then the effective advection velocity is less than the local mean velocity; and if it is slowly narrowing then the effective advection velocity is higher than the local mean. However, this is a little misleading as in Section 6.2.4 the opposite effect in the conservative form of the evolution equation is observed.

The effect of varying diffusivity is opposite to this; for example, if the cross–stream diffusivity κ is increasing along the channel then the effective advection velocity is heightened. This may be expected, since an increasing longitudinal diffusivity will spread the front of any contaminant pulse faster and hence heighten the average velocity of the contaminant. No time variation in the flux of the advecting fluid will affect the evolution to this order.

6.2.3 Correction to the dispersion coefficient

Changes to the shear dispersion coefficient, and higher order corrections to the advection velocity, can be obtained by calculating the next correction to the

evolution, namely G^3. On doing this I obtain

$$\frac{\partial C}{\partial t} \sim -\frac{\xi}{\tau}\left[1-\frac{2}{105}\xi'+\frac{1}{17325}\left(33\left(\xi^2(\log\tau)'\right)'-4\left(\xi\xi'\right)'+33(\tau\dot{\xi})'\right)\right]C' + \frac{2\xi^2}{105\tau}\left[1+\frac{1}{110}\left(11\tau(\xi/\tau)'-7\xi'-11\tau(\log\xi)^{\bullet}\right)\right]C''+\frac{4\xi^3}{17325\tau}C'''. \tag{6.2.11}$$

From this it can be seen that the evolution on the centre manifold has been further refined, with the effects of the varying flux and diffusivity evident in the advection velocity of the mean concentration and the shear dispersion coefficient through their dependence upon the derivatives of ξ and τ. To this order the local shear dispersion coefficient, which to leading order is $2\xi^2/105\tau$, is lessened if the channel is widening and heightened if the channel is narrowing. This effect occurs in all the shear dispersion coefficients which I have found and may be explained as follows: in a narrowing channel, for example, consider a line release of contaminant at the left end of a length of channel. If there were no cross–stream diffusion then the contaminant near the bank travels slowly, stays near the left end for a long time, experiences a slower net velocity there when compared to a channel of the same average width, and hence lingers at the left longer (in this comparison). The converse is true for the contaminant released near the channel centre. Hence, the concentration in the tails of the contaminant distribution is higher, and thus the shear dispersion coefficient is larger than that for a straight channel.

Once again the effect of the variable diffusivity, this time on the effective diffusion coefficient, is opposite to that of the breadth variations. This can be seen to be reasonable by again considering a line release in a straight channel where the cross–stream diffusivity $\kappa(x,t)$ decreases downstream. Over a shear–dispersion time–scale τ and length–scale ξ the contaminant cloud, especially in the initial stages, experiences more of the larger κ near the release than the smaller κ downstream. Thus the shear dispersion, which is inversely proportional to the cross–stream diffusivity κ, is lessened if κ is decreasing.

Time variations also have an effect upon the coefficients of the evolution

equation (6.2.11) but it is difficult to explain, from a physical point of view, how these arise. The only term in the advection velocity which depends upon time variations is in the form $(\tau\dot{\xi})'$, and so there is no effect unless the time variations also occur in conjunction with downstream variations. However, the shear dispersion coefficient has an adjustment proportional to $-(\log\xi)^{\bullet}$, and so the shear dispersion is lessened if the diffusivity κ is decreasing in time or if the flux F is increasing. Since the shear dispersion is predominantly proportional to F^2/κ, this indicates that it is the earlier values of $F(t)$ and $\kappa(t)$ which are important in determining the shear dispersion at any given time. This "memory effect" will be discussed further in Section 6.2.5.

Higher order corrections to the above equations can be calculated, the only difficulty being the enormous complexity of the algebra involved. The above analysis reinforces that ξ and τ are fundamental measures of the local shear dispersion. This is expected since these represent the basic mechanisms of cross–channel diffusion and down–stream advection which combine to give the shear dispersion.

6.2.4 The asymptotic equation in conservative form

Here I rewrite the evolution equation in a conservative form, which can always be done as the total amount of contaminant is a conserved quantity. Hence its one–dimensional density

$$\mathcal{C} = 2bC, \tag{6.2.12}$$

must satisfy a conservation equation

$$\frac{\partial\mathcal{C}}{\partial t} + \frac{\partial\mathcal{F}}{\partial x} = 0, \tag{6.2.13}$$

where $\mathcal{F}$ is the total flux of contaminant past any given cross–section. The evolution of this one–dimensional density gives how the contaminant pulse evolves rather than the cross–sectionally averaged concentration of the contaminant. This is a more relevant quantity in many physical circumstances. The formulation as a conservative equation also provides a further check on the algebra.

Upon multiplying (6.2.11) by $2b$ and rearranging I find the flux is

$$\mathcal{F} = \frac{\xi}{\tau}\Bigg[1 - \frac{2}{105}\tau\left(\frac{\xi}{\tau}\right)' - \frac{1}{17325}\Bigg(4(\xi\xi')' - 41\xi^2(\log\tau)'' - 45\frac{\xi}{\tau}(\xi\tau')' - 33(\log\xi)^{\bullet}\tau\left(\frac{\xi}{\tau}\right)'\Bigg)\Bigg]\mathcal{C} - \frac{2}{105}\frac{\xi^2}{\tau}\left[1 + \frac{1}{165}\left(3\xi' - 41\xi\tau' - 33\xi(\log\xi)^{\bullet}\right)\right]\mathcal{C}' - \frac{4}{17325}\frac{\xi^3}{\tau}\mathcal{C}''. \tag{6.2.14}$$

It can be seen from this how the various coefficients of the flux of the contaminant at any given point depends upon the varying media. More simply, to second order

$$\mathcal{F} = U\left(1 - \frac{2}{105}\tau U'\right)\mathcal{C} - \frac{2}{105}\frac{\xi^2}{\tau}\mathcal{C}', \tag{6.2.15}$$

where $U = F/2b$. Hence the variations in the channel width affect the one–dimensional density in the opposite manner to that of the cross–sectional average C. If the channel is widening, then U is decreasing and the advection velocity of the one–dimensional density is heightened. Both the cross–sectionally averaged concentration and the one–dimensional density are commonly used quantities in channel flows. One must therefore be careful to always define which measure one is dealing with when considering channel flows in varying–width channels.

The correction to the dispersion coefficient in the conservative formulation is qualitatively the same as in the previous non-conservative formulation.

6.2.5 Memory effect

An intrinsic feature of dispersion in channels with varying properties is the memory effect of the dispersion process as discussed by Smith (1983). Consider the case when the only variations occur in the flux with respect to time. The shear dispersion coefficient and its correction, given in conservative form by (6.2.14), can be rewritten to the same order of accuracy as

$$\frac{2}{105}\left(\frac{\xi^2}{\tau} - \frac{\xi\dot{\xi}}{5\tau}\right) = \frac{2}{105}\left[\xi\left(t - \tau/10\right)\right]^2. \tag{6.2.16}$$

This shows the memory effect of the dispersion process—the effective dispersion coefficient at time t is equivalent to the uncorrected dispersion coefficient at the

earlier time of $t - \tau/10$. The effect is similar for a varying channel. Allowing for all the variations in the media, from (6.2.15) the first–order correction to the advection velocity, $U(x,t) = \xi/\tau$, of the one–dimensional density can be rewritten as

$$\frac{\xi}{\tau} - \frac{2}{105}\xi\left(\frac{\xi}{\tau}\right)' = U - \frac{2}{105}\xi U' \simeq U(x - 2\xi/105, t) \qquad (6.2.17)$$

to the same order of accuracy. So the corrected advection velocity at position x along the channel is equivalent to the uncorrected advection velocity a distance $2\xi/105$ upstream from this position.

6.3 Conclusion and further work

6.3.1 Conclusion

This centre manifold approach to shear dispersion has the advantage that the derivation of successive approximations is purely mechanistic once the original approximation has been deduced, and there is no need to resort to heuristic arguments to calculate higher order approximations. This approach has some rigorous support (see Carr (1981)) although, for simplicity and clarity, the rigorous derivation is not included here. I have calculated the approximations to high order and shown that they converge by comparing their behaviour to that of a model function. From this convergence a quantitative estimate for the minimum resolvable length–scale has been obtained.

The application of centre manifold theory to the problem of shear dispersion in channels also provides a systematic and consistent method for investigating the problem of varying cross–sectional area. This was identified by Chatwin and Allen (1985) as an outstanding problem in shear dispersion. In particular I have addressed what changes should be made to the advection-diffusion equation when the cross-sectional area is varying. The usual Taylor model is not valid in this case and so new approximations have been determined for this and other situations of immense practical interest, such as varying flux and varying diffusivity.

6.3.2 Further work

More complex physical processes, such as decaying contaminant, meandering, chemical reactions or other nonlinearities, can be incorporated within the centre manifold framework. The only alteration needed to accommodate these changes is to incorporate the terms in the right–hand side of (6.2.6) which represent the dynamics of the processes. This again shows the power of the centre manifold approach — generalisations or extensions are easily incorporated once the original problem has been formulated.

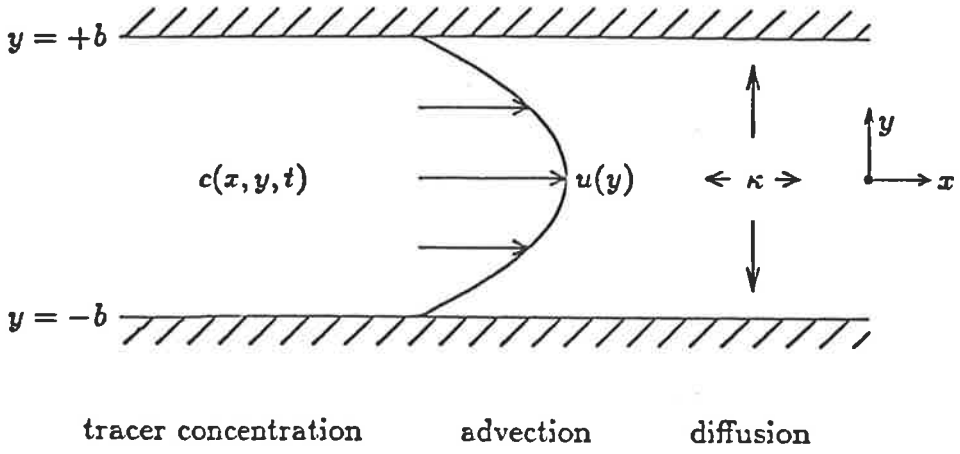

Figure 6.1: A schematic diagram of shear dispersion in a channel of width $2b$.

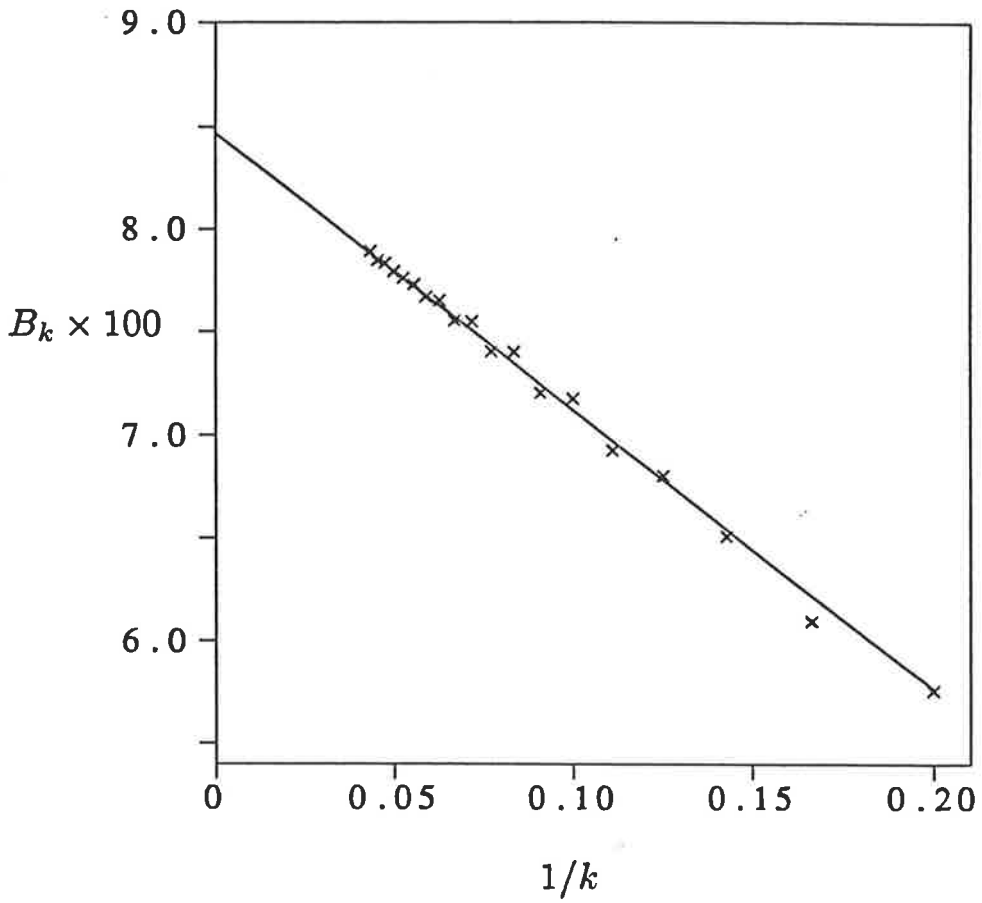

Figure 6.2a: Generalised Domb–Sykes plot to estimate the radius of convergence for channel flow.

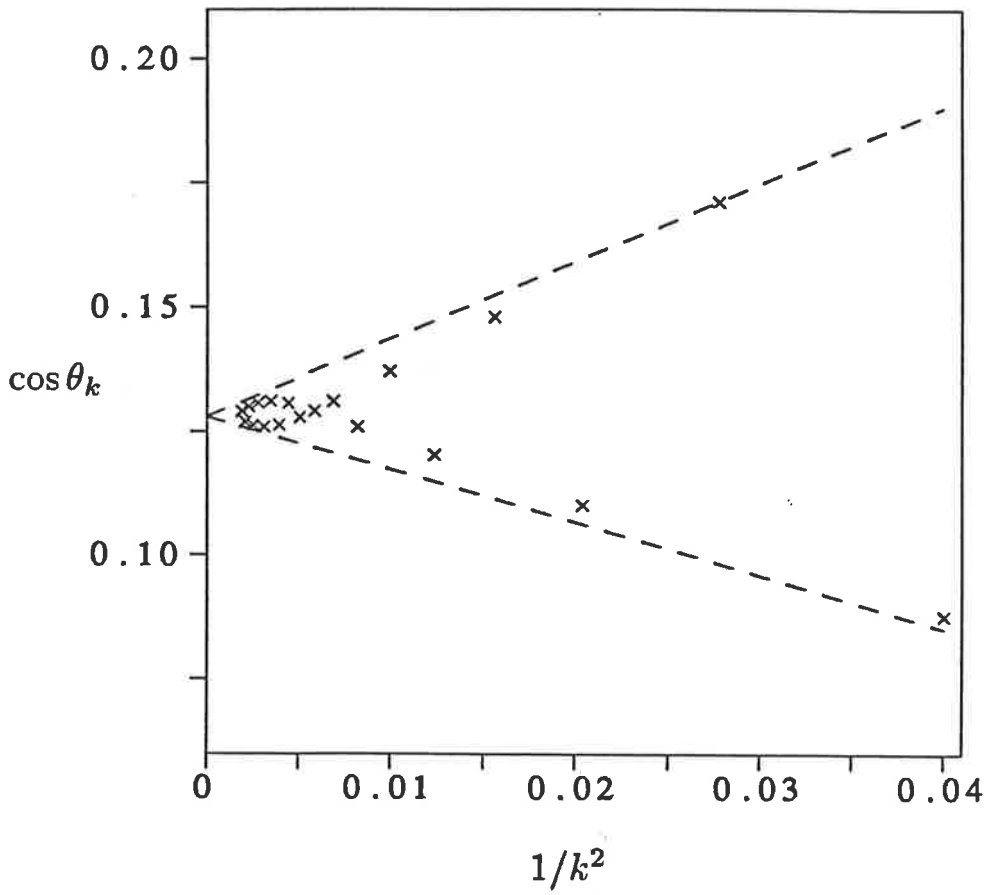

Figure 6.2b: Generalised Domb–Sykes plot to estimate the cosine of the angle from the real axis for channel flow.

CHAPTER 7

SHEAR DISPERSION IN PIPES

7.1 Constant cross–section

7.1.1 Formulation

The analysis of shear dispersion in a circular pipe follows closely the analysis for shear dispersion in a channel presented in Chapter 6. I start by analysing the dispersion of contaminant in a straight circular pipe of constant radius a. See Figure 7.1 for a schematic diagram. The governing equation is the three dimensional advection–diffusion equation

$$\frac{\partial c}{\partial t} + \nabla \cdot (\mathbf{q}c) = \nabla \cdot (\kappa \nabla c). \tag{7.1.1}$$

Here κ is the diffusivity, $c(x, r, \theta, t)$ is the concentration of contaminant and $\mathbf{q}$ is a given velocity profile. The fluid is assumed incompressible and the advection velocity is taken to be solely in the the x direction (along the pipe) but varying radially, that is the velocity field is

$$\mathbf{q} = u(r)\mathbf{i}, \tag{7.1.2}$$

where $\mathbf{i}$ is a unit vector in the direction of the x-axis. This is subject to no flux of contaminant through the pipe walls which gives

$$\frac{\partial c}{\partial r} = 0 \quad \text{on} \quad r = a. \tag{7.1.3}$$

To simplify the analysis it is necessary to choose a velocity profile. I consider an axisymmetric Poiseuille flow given by

$$u(r) = 2U\left(1 - R^2\right), \tag{7.1.4}$$

where $R = r/a$ is a non–dimensional radius. In cylindrical coordinates the governing equation (7.1.1), upon placing the dominant mechanism of cross–pipe diffusion on the left–hand side, becomes

$$\mathcal{L}c = \frac{\partial c}{\partial t} + u(r)\frac{\partial c}{\partial x} - \kappa \frac{\partial^2 c}{\partial x^2}, \tag{7.1.5}$$

where $\mathcal{L}$ is the operator defined by

$$\mathcal{L}c = \kappa \frac{1}{r}\frac{\partial}{\partial r}\left(r\frac{\partial c}{\partial r}\right) + \kappa \frac{1}{r^2}\frac{\partial^2 c}{\partial \theta^2} \quad \text{such that} \quad \frac{\partial c}{\partial r} = 0 \quad \text{on} \quad r = a. \tag{7.1.6}$$

The operator $\mathcal{L}$ has one zero eigenvalue and infinitely many other eigenvalues all of which are strictly negative and given by

$$\gamma_{in} = -\kappa\left(\frac{\mu_{in}}{a}\right)^2 \quad \text{for} \quad i = 1, 2, \ldots, \quad \text{and} \quad n = 0, 1, 2, \ldots \tag{7.1.7}$$

where μ_{in}, $i = 1, 2, \ldots$, $n = 0, 1, 2, \ldots$ are the roots of $J_n'(\mu) = 0$ and $2\pi/n$ is the period of the θ dependence. These eigenvalues have corresponding eigenmodes $\cos(n\theta)J_n(R\mu_{in})$. If it were not for the "nonlinear" right–hand side terms in (7.1.5) all the modes would decay exponentially quickly to zero, leaving the contaminant field to be constant across the pipe. Within the context of centre manifold theory, by including the "nonlinear" right–hand side there is still exponential decay but onto the centre manifold. This centre manifold is reached exponentially quickly in a time which is estimated via the least negative eigenvalue of $\mathcal{L}$. For the axisymmetric case ($n = 0$) this eigenvalue is $\gamma_{10} = -14.684\kappa/a^2$, which was recognized by Taylor (1953b) and expressed in his equation (15). For the non–axisymmetric case ($n > 0$) the least negative eigenvalue is given by $\gamma_{11} = -3.3900\kappa/a^2$. A non–axisymmetric mode has the slowest decay (by a factor of 4) and hence dominates the evolution to the centre manifold.

In a similar manner to the analysis of shear dispersion in a channel in Chapter 6, I do not follow the more rigorous approach of Mercer and Roberts (1990) by choosing not to transform the problem into Fourier space. Hence the following derivation is not directly rigorous — it can be made so by transforming into Fourier space. I now apply the centre manifold procedure by assuming that the concentration c may be described by

$$c = V[r, \theta; C] \tag{7.1.8}$$

where $C(x,t)$ is the cross–sectionally averaged concentration of contaminant and its evolution in time, and indirectly that of c through (7.1.8), is described by

$$\frac{\partial C}{\partial t} = G[C]. \tag{7.1.9}$$

I seek the asymptotic solution of (7.1.5) in the form

$$c = V[r,\theta;C] \sim \sum_{n=0}^{\infty} v_n(r,\theta)\frac{\partial^n C}{\partial x^n} \quad \text{such that} \quad \frac{\partial C}{\partial t} = G[C] \sim \sum_{n=1}^{\infty} g_n \frac{\partial^n C}{\partial x^n}. \tag{7.1.10}$$

Upon this substitution and equating coefficients of terms involving $\frac{\partial^n C}{\partial x^n}$ I obtain the system of equations

$$\begin{aligned} \mathcal{L}v_0 &= 0 \\ \mathcal{L}v_1 &= v_0 g_1 + u(r)v_0 \\ \mathcal{L}v_n &= \sum_{\ell=1}^{n} v_{n-\ell}\ g_\ell + u(r)v_{n-1} - \kappa v_{n-2} \quad n = 2,3\ldots \quad . \end{aligned} \tag{7.1.11}$$

Solving these in succession I obtain the centre manifold to be

$$\begin{aligned} c \sim & C + \frac{Ua^2}{24\kappa}\left(-2+6R^2-3R^4\right)C' \\ & + \frac{U^2a^4}{11520\kappa^2}\left(31-180R^2+300R^4-200R^6+45R^8\right)C'' \\ & + \frac{U^3a^6}{3225600\kappa^3}\big(109+490R^2-3185R^4+4900R^6-350R^8 \\ & \quad +1246R^{10}-175R^{12}\big)C''' + \cdots \end{aligned} \tag{7.1.12}$$

Observe that with the axisymmetric velocity profile (7.1.4) the centre manifold has no θ dependence and hence in the long–term the dispersion will be axisymmetric. The evolution of the cross–sectionally averaged concentration along this centre manifold is, to the first three orders, given by

$$\frac{\partial C}{\partial t} = -UC' + (\kappa + D)\,C'' - \frac{U^3a^4}{2880\kappa^2}C''', \tag{7.1.13}$$

where

$$D = \frac{U^2a^2}{48\kappa}. \tag{7.1.14}$$

These are precisely the approximations obtained by Chatwin (1970) in his equations (4.1). Just one part of the power of this centre manifold approach is the ease with which these and higher order approximations can be calculated.

Calculating higher order corrections to equation (7.1.13) and rewriting the resultant equation in the form

$$\frac{\partial C}{\partial t} = -UC' + (\kappa + D)\, C'' + \frac{\kappa}{a^2} \sum_{n=3}^{\infty} A_n \xi^n \frac{\partial^n C}{\partial x^n} \tag{7.1.15}$$

where $\xi = Ua^2/\kappa$ is the downstream advection distance in a cross–pipe diffusion time $\tau = a^2/\kappa$, I find the first five of the coefficients (A_n) are

$$\begin{aligned} A_3 &= -3.4721 \times 10^{-4}, \\ A_4 &= -1.5888 \times 10^{-5}, \\ A_5 &= 1.1755 \times 10^{-6}, \\ A_6 &= 4.9257 \times 10^{-9}, \\ A_7 &= -3.6895 \times 10^{-9}. \end{aligned} \tag{7.1.16}$$

Using REDUCE I calculate the coefficients up to the 24^{th} order and find that the numerical coefficients approximately follow the pattern of signs $++--++--\cdots$. Using the method outlined in the Appendix of Mercer and Roberts (1990) I obtain the generalised Domb–Sykes plots shown in Figure 7.2(a), (b). Figure 7.2(a) indicates that the radius of convergence (in Fourier space) of the series in (7.1.15) is $R_c = 13.8/\xi$. Furthermore, from Figure 7.2(b), the angle from the real axis of the convergence limiting singularity is $\theta = \pm 106°$. This places the singularity at the position $(-3.9, \pm 13.2)$ in the complex $(ik\xi)$-plane which is in agreement with the branch point found by Stokes and Barton (1990). Also, the predicted nature of the singularity from Figure 7.2(a) is $\nu = 0.521$ which is close to the expected value of $\nu = 1/2$, appropriate for the expected square root behaviour at a branch point (§7.5 in Bender and Orszag (1978)). The convergence of this series implies that some finite truncation of the evolution equation will give a useful approximation

to the evolution of the cross–sectionally averaged concentration, but only if the resolved wave–length scales satisfy

$$L > \frac{2\pi\xi}{R_c} \simeq \left(\frac{Ua^2}{2.2\kappa}\right). \tag{7.1.17}$$

The importance of this result is that it is quantitative. Taylor (1954) argued that $L \gg \xi/4$, his equation (26), and then suggested that $\gg$ would be satisfied if a ratio of $10:1$ existed between the two sides, that is, if $L > 2.5\xi$. However, I have shown that a length–scale approximately one–fifth of this is the actual quantitative limit of resolution for high order Taylor models of shear dispersion in a pipe.

I have used centre manifold theory to derive the well known approximations of Taylor and others as well as high order approximations to the problem of contaminant dispersion in straight pipes. The important question of the validity of a finite truncation of the evolution equations, as used by all workers in this field, has been answered and a minimal length scale where the equations are still valid has been calculated. As well as being supported theoretically (Carr (1981)) the validity of this centre manifold approach is also shown by its agreement with other workers such as Stokes and Barton (1990), Smith (1981) and Chatwin (1970).

7.2 A finite difference numerical scheme

7.2.1 Development

The area of numerical solutions to the pipe dispersion problem is not a new one. Many workers have devoted much time in efforts to accurately calculate contaminant concentrations at both small and large times after release (see Barton and Stokes (1990), Chikwendu (1986), Smith (1987) to name but a few). To accurately model the dispersion process it is important that the numerical scheme matches the evolution equation to a similar order — there is no point in using a high order evolution equation if the numerical scheme is only accurate to a low order. The aim here is to demonstrate a new method of determining an explicit finite difference scheme that matches the evolution equation to a predetermined order

of accuracy, guarantees non–negativity of the mean concentration and is stable. I also investigate the limitations imposed upon the space–time resolution of the numerical scheme when constructing high order approximations to the evolution equation.

To develop the finite difference scheme denote the mean concentration at any time $C(x,t) = C(j\Delta x, n\Delta t)$ by C_j^n where Δx is the spatial step and Δt is the time step. I wish to find an explicit N time–level finite difference scheme with J spatial points: K upstream and L downstream of the current spatial position. An example which is used is drawn in Figure 7.3. The numerical integration scheme is thus

$$C_j^n = \sum_{n'=1}^{N} \sum_{j'=-L}^{K} b_{j'}^{n'} C_{j-j'}^{n-n'}, \tag{7.2.1}$$

where the coefficients b_j^n are to be determined. To guarantee non–negativity of the concentration it is sufficient that all the b_j^n are non–negative provided the initial conditions are non–negative. Since the evolution equation is conservative, so will the numerical scheme, which in conjunction with the non–negativity ensures boundedness and thus guarantees stability. I aim to choose the b_j^n's to satisfy this non–negativity, and to match the evolution equation (7.1.15) to some order of accuracy so that the numerical scheme has the same asymptotic behaviour as the exact system.

For simplicity, and since it is typically small compared to $D\frac{\partial^2 C}{\partial x^2}$, I choose to ignore the downstream diffusion term $\kappa\frac{\partial^2 C}{\partial x^2}$ in (7.1.15). Substituting $C(x,t) \propto \exp(st + ikx)$ I obtain the dispersion relation

$$s = -Uik + D\,(ik)^2 + \frac{\kappa}{a^2} \sum_{n=3}^{\infty} A_n (ik\xi)^n. \tag{7.2.2}$$

Since the general solution of the evolution equation (7.1.15) will be a linear superposition of the Fourier modes $\exp(st + ikx)$ I want the numerical scheme to match the relation (7.2.2) as accurately as possible. I substitute the corresponding form

$$C_j^n = \lambda^n e^{ik\Delta x j} \tag{7.2.3}$$

into equation (7.2.1) and divide by $\lambda^n e^{ik\Delta xj}$ to obtain that the numerical dispersion relation will satisfy

$$1 = \sum_{n'} \sum_{j'} b_{j'}^{n'} \lambda^{-n'} e^{-ik\Delta xj'}. \tag{7.2.4}$$

Using the fact that

$$\lambda = e^{s\Delta t} \tag{7.2.5}$$

where s is the desired function of k given by (7.2.2) I can rewrite the right–hand side of (7.2.4) as a power series in wavenumber k where the coefficients are linear combinations of the b_j^n's. That is

$$1 = \sum_{p=0}^{\infty} \left(\sum_{n} \sum_{j} d_{p_j}^{\ n} b_j^n \right) k^p, \tag{7.2.6}$$

where the $d_{p_j}^{\ n}$ are known from the above analysis and I need to determine the b_j^n to satisfy this equation to some order of accuracy in wavenumber k. For any given space and time steps, Δx and Δt, and any given desired order of accuracy this becomes the straightforward linear programming task of finding a feasible solution to (7.2.6) subject to the non–negativity constraint. In terms of the cross–stream diffusion time, $\tau = a^2/\kappa$, and the corresponding advection distance, $\xi = Ua^2/\kappa$, I determine values for $\Delta x/\xi$ and $\Delta t/\tau$ such that a conservative finite difference scheme can be constructed to a predetermined order of accuracy. Figures 7.4 (a), (b), (c) and (d) show the regions in the $(\Delta x/\xi, \Delta t/\tau)$ plane where feasible solutions could be found for order 2, 3, 4 and 5 methods respectively with $N = 3$, $J = 4$, $L = 1$ and $K = 2$ as shown in Figure 7.3. For an order 2 truncation (the usual Taylor model) the region of feasible solutions is relatively large. Hence a stable, non–negative, finite difference scheme could be easily formulated. The order 3 truncation only marginally reduces the feasible region. For the fourth and fifth order truncations of the evolution equation the feasible region in $(\Delta x/\xi, \Delta t/\tau)$ space is greatly reduced and hence care must be taken when formulating a finite

difference scheme to accurately select the space and time steps so as to ensure a conservative and non–negative scheme. Even though it is desirable to accurately model the dynamics of the dispersion process by including higher order derivative terms in the model equation this comes at a price. The feasible region is greatly reduced and hence the flexibility of the method is reduced. That is not to say that the higher derivative terms should not be included, just that greater care much be taken when formulating the numerical scheme.

It is curious but pleasing that the minimum wavelength resolved by a high order numerical scheme, $L \approx 0.2\xi$ to 0.4ξ, is similar to the minimum wavelength resolved by the centre manifold model, $L \approx 0.45\xi$.

7.2.2 Results

Figure 7.5 shows a plot of the mean concentration, C, versus x for the order 2 approximation (Taylor) and order 5 approximation at various times after a unit pulse release of contaminant at $x = 0$. For the order 5 approximation the markedly non–Gaussian shape of the profile for small to medium times is obvious and for larger times it has a similar shape to the order 2 approximation once the higher order derivative terms are no longer dominant.

By increasing the number of spatial points (increasing J and hence K and L) the feasible region can be substantially increased, especially for the higher order approximations. Figures 7.6 (a), (b), (c) and (d) show the feasible regions in $(\Delta x/\xi, \Delta t/\tau)$ space for order 2, 3, 4 and 5 methods respectively with 3 temporal levels ($N = 3$) as before and 6 spatial points ($J = 6$), 3 upstream ($K = 3$) and 2 downstream ($L = 2$). Comparing these to Figures 7.4 (a), (b), (c) and (d) in which only 4 spatial points were used, it is clear that the feasible region has increased, particularly for the higher order methods (order 4 and 5). This enlargement of the feasible region is due to increased flexibility in approximating the higher derivative terms when using more spatial points. This increase comes at the expense of an increase in the size of the linear programming problem due to the addition spatial

points. The finite difference scheme can be tailored to suit the problem at hand by altering the number of spatial points and finding a feasible solution for given spatial and temporal steps.

7.3 Appropriate initial condition

7.3.1 Introduction

Here I determine the appropriate initial condition to be used for the Taylor model of shear dispersion in a pipe. The theory of centre manifolds, see Carr and Muncaster (1983), states that for any exact solution of (7.1.1)–(7.1.3) (provided that it is sufficiently close to the origin) there exists a solution on the centre manifold that is approached exponentially quickly. Thus for a given initial condition of the exact problem $c(x,r,\theta,0) = c_0(x,r,\theta)$ there exists an initial condition $C(x,0) = C_0(x)$ of (7.1.15) such that the model equation solution is approached exponentially quickly by the exact solution. The obvious choice of $C_0(x)$ is to take the cross–sectionally average of $c_0(x,r,\theta)$ since $C(x,t)$ is defined to be the cross–sectional average of $c(x,r,\theta,t)$. As described in Mercer and Roberts (1990) for the channel case and subsequently by Young and Jones (1991) for the pipe case this leads to errors which do not decay. It is possible to eliminate these errors through refining the choice of $C_0(x)$ by considering the dynamics near the centre manifold.

7.3.2 Analysis

By transforming to Fourier space it is possible to rigorously derive the appropriate initial condition. The full details for the channel case are given in Mercer and Roberts (1990), §2 and will not be repeated here. To proceed for the pipe case a similar analysis is used with allowances for the different geometry. The method consists of projecting a given initial condition onto the centre manifold so that the long–term behaviour on the centre manifold matches that of the exact solution with the given initial condition (see Roberts (1989)). Furthermore, this matching is attained exponentially quickly in time.

On performing the analysis I obtain an expression for C_0 in terms of c_0 and the v_n's,

$$\overline{\left(\sum_{n=0}^{\infty} v_n(r)\frac{\partial^n}{\partial x^n}\right)^2} C_0 = \sum_{n=0}^{\infty} \frac{\partial^n}{\partial x^n}\left(\overline{v_n(r)c_0}\right), \tag{7.3.1}$$

where the overbar denotes the cross–sectional average. Expanding this in the "small" parameter $\frac{\partial}{\partial x}$ and truncating at second order I obtain

$$C_0 = \overline{c_0} + \frac{\partial}{\partial x}\left(\overline{v_1 c_0}\right) + \frac{\partial^2}{\partial x^2}\left(\overline{v_2 c_0} - \frac{\xi^2}{720}\overline{c_0}\right). \tag{7.3.2}$$

From this it can be seen that the usual, and at first inspection the obvious, initial condition for the Taylor model, that $C_0 = \overline{c_0}$, is just the leading approximation to the correct initial condition, the first few asymptotic terms of which are given above. The initial condition can be calculated more accurately by retaining more terms in the expansion of (7.3.1), the only complication being the algebra involved. This agreement holds to the order of the truncation of the asymptotic sums. It has been shown, by Mercer and Roberts (1990) for the channel case and recently by Young and Jones (1991) for the pipe case, that it is possible, by prescribing the correct initial conditions, to predict the observed phenomena of centroid displacement and variance deficit present in shear dispersion. This is not possible using the Taylor model with the usual leading order approximation of using the cross–sectional average as the initial condition; setting $C_0 = \overline{c_0}$ assures only that the total contaminant is correct. Higher order corrections to the Taylor model used in conjunction with the appropriate initial condition enables shear dispersion processes to be modelled more accurately; for example, the $\frac{\partial c_0}{\partial x}$ term in (7.3.2) ensures that the centroid displacement is correctly predicted, while the $\frac{\partial^2 c_0}{\partial x^2}$ terms ensure that the variance deficit is correct. This is contrary to the conclusions of Frankel and Brenner (1989) "that no *systematic* improvement in the asymptotic order of approximation is possible through the incorporation of higher–order gradient terms into the model constitutive equation". Indeed the centre manifold approach used here provides this systematic improvement provided the initial

condition and the higher order gradient terms are both modelled appropriately.

7.4. Appropriate boundary conditions

7.4.1 Introduction

The Taylor model of shear dispersion holds in the interior of a pipe when the contaminant concentration is nearly smooth across the pipe and slowly varying along the pipe. In general the Taylor model need not apply at the ends of the pipe, $x = 0$ (inlet) and $x = L$ (outlet), where end effects may cause transition "boundary layers" to occur. The question that then arises is: what are the boundary conditions at the inlet and outlet to be used with the Taylor model, and its higher order generalisations, so that the solution of the model accurately predicts the exact solution. A similar problem was studied by Smith (1988) and Roberts (1991b) for the shear dispersion of contaminants in channels. The centre manifold approach used by Roberts (1991b) will be used here to determine the appropriate boundary conditions. The approach is to apply centre manifold theory to the "evolution" in the spatial coordinate x, with slow time variations being regarded as a perturbative effect.

7.4.2 Entry condition

As in §7.2 I choose to ignore the downstream diffusion term $\kappa\frac{\partial^2 c}{\partial x^2}$ since typically $\kappa \ll D$ and so equation (7.1.1) may be written

$$u(r)\frac{\partial c}{\partial x} = \kappa\frac{1}{r}\frac{\partial}{\partial r}\left(r\frac{\partial c}{\partial r}\right) + \kappa\frac{1}{r^2}\frac{\partial^2 c}{\partial \theta^2} - \frac{\partial c}{\partial t}. \tag{7.4.1}$$

Assuming initially that there is no contaminant in the pipe and taking the Laplace transform of this equation I obtain

$$\frac{\partial \check{c}}{\partial x} = \frac{\kappa}{u(r)}\frac{1}{r}\frac{\partial}{\partial r}\left(r\frac{\partial \check{c}}{\partial r}\right) + \frac{\kappa}{u(r)}\frac{1}{r^2}\frac{\partial^2 \check{c}}{\partial \theta^2} - \frac{1}{u(r)}p\check{c}, \tag{7.4.2}$$

where transformed quantities are denoted by $\check{}$ and the Laplace transform is defined by

$$\check{f}(p) = \int_0^\infty f(t)e^{-pt}dt. \tag{7.4.3}$$

Equation (7.4.2) takes the form of an evolution equation with x as the "time–like" variable. The true time is represented by the parameter p and, provided the conditions at the pipe entrance are not rapidly varying in time, the parameter p will be small, hence the third term in the right–hand side of (7.4.2) can be thought of as a small perturbation term. This can be incorporated within the framework of centre manifold theory by adjoining the evolution equation

$$\frac{\partial p}{\partial x} = 0. \tag{7.4.4}$$

"Linearly", the evolution (in the time–like variable x) from the entry of the pipe to the interior is governed by (7.4.4) and

$$\frac{\partial \check{c}}{\partial x} = \frac{\kappa}{u(r)} \frac{1}{r} \frac{\partial}{\partial r} \left(r \frac{\partial \check{c}}{\partial r} \right) + \frac{\kappa}{u(r)} \frac{1}{r^2} \frac{\partial^2 \check{c}}{\partial \theta^2} \quad \text{s.t.} \quad \frac{\partial \check{c}}{\partial r} = 0 \quad \text{on} \quad r = a. \tag{7.4.5}$$

For the axisymmetric case the operator on the right-hand side of (7.4.5) has a discrete spectrum, $\lambda = 0, -\alpha_{10}, -\alpha_{20}, -\alpha_{30}, -\alpha_{40}, \cdots$ where the α_{i0} are the eigenvalues of a Sturm–Louiville problem obtained numerically via the NAG routine D02KDF to be $\alpha_{10} = 12.8398/\xi$, $\alpha_{20} = 41.9309/\xi$, $\alpha_{30} = 87.0834/\xi$, $\alpha_{40} = 148.2682/\xi$ etc. For the non–axisymmetric case ($\cos(n\theta)$ variations for $n > 0$) the least negative eigenvalue is $\lambda = -\alpha_{11} = -4.1605/\xi$ (for $n = 1$). Applying centre manifold theory, Carr (1981), I deduce that for sufficiently small p and for all "initial" conditions, $\check{c} = \check{c}^0(r, \theta)$ at $x = 0$, the system will evolve exponentially quickly to the smooth centre manifold parameterised by p and $\check{C}$, where $\check{C}$ is the cross–sectional average of $\check{c}$. This exponential approach is dominated by the slowest linear transient, that is, it is roughly like $\exp(-\alpha_{1n}x)$ for the axisymmetric ($n = 0$) and non–axisymmetric ($n = 1$) cases. Applying similar methods to that used in §7.1 I find the centre manifold to be

$$\begin{aligned} \check{c} = \check{C} &- \frac{\tau}{24} \left(-2 + 6R^2 - 3R^4 \right) p\check{C} \\ &+ \frac{\tau^2}{11520} \left(11 - 120R^2 + 270R^4 - 200R^6 + 45R^8 \right) p^2 \check{C} + \cdots \end{aligned} \tag{7.4.6}$$

on which the evolution takes place according to

$$U\frac{\partial \check{C}}{\partial x} = -p\check{C} + \frac{\tau}{48}p^2\check{C} - \frac{\tau^2}{1920}p^3\check{C} + \cdots \tag{7.4.7}$$

and (7.4.4), where τ is the cross–pipe diffusion time as defined earlier. Equations (7.4.6) and (7.4.7) model the slow spatial evolution into the interior of the pipe in the presence of slow time variations. Since these represent the same class of slowly–varying distributions the above expressions can also be obtained by reversion of (7.1.15) (without the $\kappa C''$ term) and substitution into (7.1.12). The question that must now be answered is: what is the appropriate value of $\check{C}$ to be used at $x = 0$ for (7.4.7) so that (7.4.6) will accurately match the exact solution of (7.4.2) in the interior of the pipe. This is a similar problem to that addressed in §7.3 but here the "time–like" variable is x and the "initial condition" is the entry condition. Applying a similar method to that used in §7.3 I find the Laplace transform of the correct "initial condition" to be $\check{C}(0) = \check{C}^0$ where

$$\left(1 + \frac{\tau}{48}p + \frac{\tau^2}{80}p^2 + \cdots\right) U\check{C}^0 = \overline{u\check{c}^0} + p\overline{uw_1\check{c}^0} + p^2\overline{uw_2\check{c}^0} + \cdots, \tag{7.4.8}$$

where $\check{c}^0(r,\theta)$ is the Laplace transform of the prescribed distribution of contaminant across the pipe entrance and where

$$\begin{aligned} w_1 &= \frac{\tau}{16}\left(1 - 4R^2 + 2R^4\right) \\ w_2 &= \frac{\tau^2}{11520}\left(3 + 60R^2 - 240R^4 + 200R^6 - 45R^8\right). \end{aligned} \tag{7.4.9}$$

The dominant term is just that $U\check{C}^0 = \overline{u\check{c}^0}$ which is the expected heuristic boundary condition, that the inlet flux of contaminant in the model and the full problem are the same, which is often used in shear dispersion problems. In a similar manner to the initial condition in §7.3, there are corrections to this intuitive boundary condition that must be made to ensure that the partial differential equation matches the exact solution when there are time dependencies present; these time dependencies are represented by the terms involving p. Since the corrections involve

terms in p, upon taking the inverse Laplace transform of (7.4.8) I find that there is a memory effect involved. To first order in p I have, in a similar manner to Roberts (1991b)

$$UC^0(t) \sim \frac{48}{\tau}\exp\left(-48t/\tau\right) * \overline{uc^0} + \frac{48}{\tau}\left[\overline{uw_1c^0} - \frac{48}{\tau}\exp(-48t/\tau)\overline{uw_1c^0}\right] \quad (7.4.10)$$

where the convolution $*$ is defined by $f(t) * g(t) = \int_0^t f(\tau)g(t-\tau)d\tau$. Due to the convolution with $\exp(-48t/\tau)$ the boundary condition exhibits a memory of earlier conditions at the entry. The memory decays exponentially on the time–scale of cross–pipe diffusion. Higher order corrections to (7.4.10) may readily be found from (7.4.8).

7.4.2 Exit condition

To perform a similar analysis at the exit I consider the evolution from $x = L$ into the interior of the pipe in the negative x–direction. Therefore $-x$ is the "time–like" variable and in a similar manner to §7.4.1 the equations governing the evolution from the exit of the pipe to the interior is

$$\begin{aligned} -\frac{\partial \check{c}}{\partial x} &= -\frac{\kappa}{u(r)}\frac{1}{r}\frac{\partial}{\partial r}\left(r\frac{\partial \check{c}}{\partial r}\right) - \frac{\kappa}{u(r)}\frac{1}{r^2}\frac{\partial^2 \check{c}}{\partial \theta^2} + \frac{1}{u(r)}p\check{c} \quad \text{s.t.} \quad \frac{\partial \check{c}}{\partial r} = 0 \quad \text{on} \quad r = a \\ -\frac{\partial p}{\partial x} &= 0 \end{aligned} \quad (7.4.11)$$

and $\check{c}$ is finite at $r = 0$. By analogy with §7.4.1 the "linear" operator on the right–hand side has a discrete spectrum of eigenvalues, namely the negative of those in §7.4.1, and hence are all non-negative. Since there are no exponentially decaying modes there is no condition arising from the dynamics of the exact system to indicate how the interior solution and the exit condition are to be matched – the smooth interior distribution holds all the way to the exit. Physically this is expected as (in the absence of along pipe diffusion) the end condition at $x = L$ should have no influence upstream. It is the exponential decay in the the evolution far upstream which produces a smoothly varying interior solution right up to the exit.

However, the Taylor model, namely

$$\frac{\partial C}{\partial t} = -U\frac{\partial C}{\partial x} + D\frac{\partial^2 C}{\partial x^2}, \tag{7.4.12}$$

has a term $D\frac{\partial^2 C}{\partial x^2}$ that introduces an upstream diffusion into the model which is not in the exact dynamics. This is allowable since this equation was derived with the assumption of a sufficiently smooth cross–stream averaged concentration $C(x,t)$ such that the downstream advection dominates. What I do find though is that this term introduces into the model the possibility of exponential transients upstream of the exit which have no physical meaning and must therefore be suppressed. This gives the necessary boundary condition to be used at the exit $x = L$.

Taking the Laplace transform of (7.4.12) I obtain

$$D\frac{\partial^2 \check{C}}{\partial x^2} - U\frac{\partial \check{C}}{\partial x} - p\check{C} = 0. \tag{7.4.13}$$

This is an evolution equation in the "time–like" variable x. For small p the solutions correspond to the slowly varying centre manifold. But for the small p there are two types of solutions of the form $e^{\lambda x}$: one with $\lambda_1 = -p/U + \tau p^2/(48U) + \cdots$, and one with $\lambda_2 = 48/(\tau U) + p/U - \tau p^2/(48U) + \cdots$. Only the first of these is slowly varying and hence corresponds to the desired interior solution. Near the exit the unphysical solution $e^{\lambda_2 x}$ decays exponentially into the interior of the pipe. This gives the possibility of rapid transients near the exit of the pipe which are unphysical and must therefore be eliminated. Hence I require that

$$\frac{\partial \check{C}}{\partial x} = \lambda_1 \check{C} = -\frac{p}{U}\check{C} + \frac{Dp^2}{U^3}\check{C}, \tag{7.4.14}$$

which to the same order in p may be written to the same order of accuracy as

$$\frac{\partial \check{C}}{\partial x} = -\frac{Up}{U^2 + Dp}\check{C}. \tag{7.4.15}$$

On taking the inverse Laplace transform I deduce the exit condition

$$D\frac{\partial C}{\partial x} = -U\exp(-48t/\tau) * \frac{\partial C}{\partial t} \tag{7.4.16}$$

which must hold at the exit $x = L$. This equation is similar to equation (7.3) in Smith (1988). Again, due to the convolution, there is a memory effect of earlier conditions at the exit. It is only for very slow variations in time, that is on a time–scale $t \gg \tau$, that I obtain the exit condition to be $\frac{\partial C}{\partial x} \approx 0$ which is the often used approximation.

In summary, the second order Taylor model of shear dispersion in a pipe should be solved with the entry condition (7.4.10) and the exit condition (7.4.16) to ensure that the model partial differential equation is accurate and consistent with the exact solution. If higher order models of shear dispersion are used then a similar analysis to that used above will yield an extra boundary condition for each order retained (see Roberts (1991b) for an example of this in the third order model of shear dispersion in a channel).

7.5 Varying radius pipe with time dependent flow

7.5.1 Introduction

As noted by Chatwin (1980) the often used Taylor approximation for dispersion problems should not be used when the pipe is not of a constant cross–section. Here I extend the analysis of shear dispersion in a pipe to allow for a varying pipe radius and a varying flux of the fluid. This centre manifold approach thus provides the methodology to appropriately model dispersion with such variations, an outstanding problem according to Chatwin and Allen (1985). The case of a varying pipe radius has applications in many areas of contaminant dispersion, such as: flow through constrictions in pipes which can alter the dispersion of some pollutant in the pipe; or flow in arteries which are of a variable cross–section. The flow in arteries would also affected by variations in the flux of the blood which can alter the dispersion of material in the blood.

7.5.2 General analysis

I consider the radius of a pipe to be given by $r = a(x)$ where $a(x)$ is a slowly varying function and hence its derivatives are small. I take the diffusivity to be

constant in space and time so that the boundary condition becomes

$$\frac{\partial c}{\partial r} - a' \frac{\partial c}{\partial x} = 0 \quad \text{on} \quad r = a(x). \tag{7.5.1}$$

Assuming the flow in the pipe to be quasi–Poiseuille, the axisymmetric stream function is given by

$$\psi = \frac{F(t)}{2\pi} \left(2R^2 - R^4\right), \tag{7.5.2}$$

where $F(t)$ is the flux of the advecting fluid, which for a constant flux reduces to $F = U\pi a^2$. The assumption of a parabolic velocity profile is valid provided the Reynolds number of the flow is small enough and the Peclet number large enough. The case presented here of a slowly varying pipe with a parabolic profile and longitudinal diffusivity included is a realisable one, and hence experiments may be able to verify the results presented here.

Equation (7.1.1) now becomes

$$\mathcal{L}c = \frac{\partial c}{\partial t} + u\frac{\partial c}{\partial x} + v\frac{\partial c}{\partial r} - \kappa\frac{\partial^2 c}{\partial x^2}. \tag{7.5.3}$$

Where $\mathcal{L}$ is the cross–pipe diffusion operator defined in §7.1.1 and u and v are the velocity components in the axial and radial directions respectively, which from the stream function are

$$u = \frac{2F}{\pi a^2}\left(1 - R^2\right) \quad ; \quad v = \frac{2Fa'}{\pi a^2}\left(R - R^3\right). \tag{7.5.4}$$

Applying centre manifold theory, as described in Chapter 6, I assume the concentration c may be described by

$$c = V[r, \theta; C] \sim \sum_{n=0}^{\infty} V^n[r, \theta; C] \quad \text{such that} \quad \frac{\partial C}{\partial t} = G[C] \sim \sum_{n=1}^{\infty} G^n[C] \tag{7.5.5}$$

where all the terms with a total of n space–time derivatives (i.e. of "order" n) are grouped into quantities with superscript n. Upon substitution I obtain the system

of equations

$$\begin{aligned}
&\mathcal{L}V^0 = 0 \quad \text{s.t.} \quad \frac{\partial V^0}{\partial r} = 0 \ \text{ on } \ r = a \\
&\mathcal{L}V^1 = V_t^0 + V_C^0 G^1 + u\frac{\partial V^0}{\partial x} + v\frac{\partial V^0}{\partial r} \quad \text{s.t.} \quad \frac{\partial V_1}{\partial r} = 0 \ \text{ on } \ r = a \\
&\mathcal{L}V^n = V_t^{n-1} + \sum_{\ell=1}^{n}\sum_{p=0}^{n-\ell} V_{C^{(p)}}^{n-\ell}\frac{\partial^p G^\ell}{\partial x^p} + u\frac{\partial V^{n-1}}{\partial x} + v\frac{\partial V^{n-1}}{\partial r} - \kappa\frac{\partial^2 V^{n-2}}{\partial x^2} \\
&\qquad \text{s.t.} \quad \frac{\partial V_n}{\partial r} = a'\frac{\partial V^{n-2}}{\partial x} \ \text{ on } \ r = a \quad n = 2,3,4,\ldots
\end{aligned} \tag{7.5.6}$$

Here, as before, the shear dispersion dynamics fundamentally occur on a time scale $\tau = a^2/\kappa$ and over a length of pipe $\xi = F/\pi\kappa$. The results are presented accordingly; however, the presence of a downstream diffusivity causes some terms to necessarily involve κ explicitly. Note that the longitudinal variations in the pipe radius only affects τ, and that the time variations in the fluid flux only affects ξ (κ is assumed constant).

7.5.3 Correction to the advection velocity

Equations (7.5.6) are solved in succession to give the centre manifold and the evolution of the cross–sectionally averaged concentration along this centre manifold. To second order I obtain the centre manifold to be

$$\begin{aligned}
c &\sim V^0 + V^1 + V^2 \\
&= C + \frac{\xi}{24}\left(-2 + 6R^2 - 3R^4\right)C' - \frac{\kappa\tau'}{8}\left(1 - 2R^2\right)C' \\
&\quad + \frac{(\log\tau)'\xi^2}{1152}\left(7 - 24R^2 + 18R^4 - 4R^6\right)C' \\
&\quad + \frac{\tau\dot{\xi}}{1152}\left(7 - 24R^2 + 18R^4 - 4R^6\right)C' \\
&\quad + \frac{\xi^2}{11520}\left(31 - 180R^2 + 300R^4 - 40R^6 + 45R^8\right)C'',
\end{aligned} \tag{7.5.7}$$

and the evolution of the cross–sectionally averaged concentration along this centre manifold is given by

$$\begin{aligned}
\frac{\partial C}{\partial t} &\sim G^1 + G^2 \\
&= -\left[\frac{\xi}{\tau} - \kappa(\log\tau)'\right]C' + \left[\frac{\xi^2}{48\tau} + \kappa\right]C''.
\end{aligned} \tag{7.5.8}$$

Observe that the effective advection velocity of the cross–sectionally averaged concentration (the local mean velocity $U = \xi/\tau$) is lessened if the pipe is widening and heightened if the pipe is narrowing. Interestingly, this effect is proportional to the diffusivity κ, and so is negligible in many practical situations. This is in direct contrast to the channel flow case as described in Chapter 6 where there is a first order change to the advection velocity even when the mechanism of longitudinal diffusion is omitted.

7.5.4 Correction to the dispersion coefficient

By calculating the evolution equation to the next order I can determine how the shear dispersion coefficient, $D \simeq \xi^2/48\tau$, is altered by the varying flux and the varying pipe radius and I can determine the next correction to the advection velocity of the mean concentration of contaminant. To third order the evolution equation can be written as

$$\begin{aligned}\frac{\partial C}{\partial t} = &-\left[\frac{\xi}{\tau}\left(1+\frac{1}{720}\xi^2(\log\tau)''+\frac{1}{720}\dot{\xi}\tau'\right)-\kappa(\log\tau)'\right]C' \\ &+\left[\frac{\xi^2}{48\tau}\left(1-\frac{1}{15}\xi(\log\tau)'-\frac{1}{15}\tau(\log\xi)^{\bullet}\right)+\kappa\right]C''-\frac{\xi^3}{2880\tau}C'''.\end{aligned} \tag{7.5.9}$$

The shear dispersion coefficient is lessened if the pipe is widening downstream or if the flux is increasing in time. Variations in the flux, with respect to time, only affect the advection velocity in conjunction with spatial variations, due to the $\dot{\xi}\tau'$ term, in a similar manner to the channel flow case see equations (6.2.11) and (6.2.14) in Chapter 6.

7.5.5 The asymptotic equation in conservative form

Since the total amount of contaminant is a conserved quantity its one-dimensional density

$$\mathcal{C} = \pi a^2 C, \tag{7.5.10}$$

must satisfy a conservation equation

$$\frac{\partial \mathcal{C}}{\partial t}+\frac{\partial \mathcal{F}}{\partial x}=0, \tag{7.5.11}$$

where $\mathcal{F}$ is the total flux of contaminant past any given cross–section. Multiplying (7.5.9) by πa^2 and rearranging I find the flux is given by

$$\mathcal{F} = \left[\frac{\xi}{\tau}\left(1 + \frac{\xi}{48}(\log\tau)' - \frac{\xi^2}{720}(\log\tau)'' - \frac{\xi^2}{90}(\log\tau)'^2 - \frac{1}{180}\xi\dot{\xi}\tau'\right) - \kappa(\log\tau)'\right]\mathcal{C} - \left[\frac{\xi^2}{48\tau}\left(1 - \frac{2}{15}\xi(\log\tau)' - \frac{1}{15}\tau(\log\xi)^{\bullet}\right) + \kappa\right]\mathcal{C}' + \frac{\xi^3}{2880\tau}\mathcal{C}''. \tag{7.5.12}$$

So the variations in the pipe radius affect the advection velocity of the one–dimensional density in a different manner to that of the cross–sectionally averaged concentration. Here, for negligible downstream diffusivity $\kappa \to 0$, there is a significant first–order correction to the advection velocity, namely $\frac{\xi}{48}(\log\tau)'$, while for the cross–sectionally averaged concentration there is none, as seen in (7.5.9).

The dispersion coefficient is decreased in a similar manner in both formulations which is similar to the channel flow case described in Chapter 6.

7.6 Conclusion and further work

7.6.1 Conclusion

A formal centre manifold procedure has been adapted to the problem of shear dispersion in pipes. The results obtained are consistent with other methods. As in the case of shear dispersion in channels, this centre manifold approach has the advantage that the derivation of successive approximations is purely mechanistic once the original approximation has been calculated and there is no need to resort to heuristic arguments to calculate higher order approximations as is needed in some other methods. A quantitative estimate for the minimum resolved length–scale has also been determined.

I have presented a new method for the calculation of a conservative finite difference scheme which matches the evolution equation to a predetermined order of accuracy. As the order of the evolution equation is increased the feasible region for such a finite difference scheme is substantially reduced. In contrast to this, as the number of spatial points is increased the feasible region is increased. Hence, if

modelling shear dispersion using a high order evolution equation great care must be taken in choosing the time and spatial steps so as to guarantee a stable non–negative scheme.

The commonly used initial conditions for shear dispersion, simply taking the cross–sectional average, has been shown to be the first approximation to the correct initial condition which, when correctly implemented, greatly improves the Taylor model of shear dispersion. The phenomena of centroid displacement and variance deficit can be resolved if higher order approximations to the evolution equation and the correct initial conditions are used.

In a similar manner the correct entry condition has been derived so that the model accurately predicts the slowly varying and smooth interior contaminant distribution. The correct exit condition has also been derived by considering the dynamics of the Taylor model near the exit.

One of the powerful properties of centre manifold theory in this application to shear dispersion is the ease with which generalisations of the analysis to varying geometries and varying flow properties may be handled. I have derived a consistent and systematic method for tackling the problem, as identified by Chatwin and Allen (1985), of what changes must be made to the evolution equation for the mean concentration when the pipe has a varying cross–sectional area and varying flow properties.

Centre manifold theory provides a consistent basis for the formation of accurate models complete with evolution equation, initial conditions and boundary conditions, even in the presence of physical inhomogeneities.

7.6.2 Further work

As with shear dispersion in channels further physical effects, such as a decaying contaminant, chemical reactions, and other nonlinearities, can be easily incorporated within the centre manifold framework. Although numerical schemes for the calculation of shear dispersion in pipes have been extensively studied this

is still an area open to further development. A method that incorporates not only a high order evolution equation of shear dispersion but also the appropriate initial condition and boundary conditions is still do be developed. By incorporating all these factors a more accurate model of dispersion processes should be able to be determined.

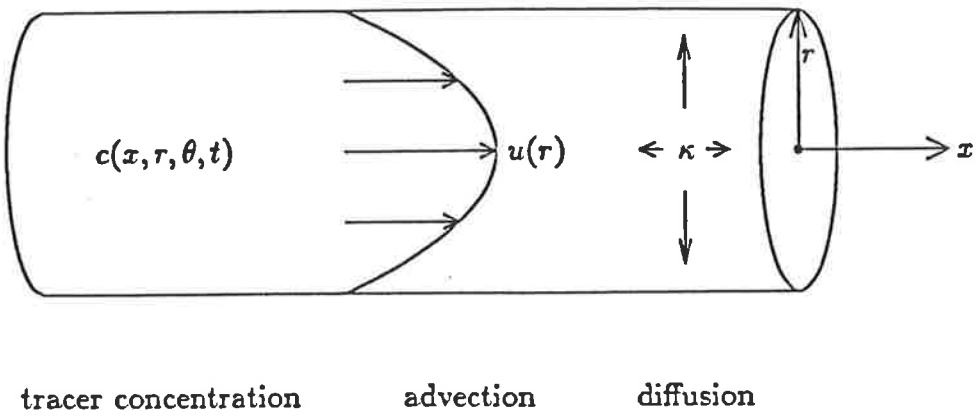

Figure 7.1: A schematic diagram of shear dispersion in a pipe of radius a.

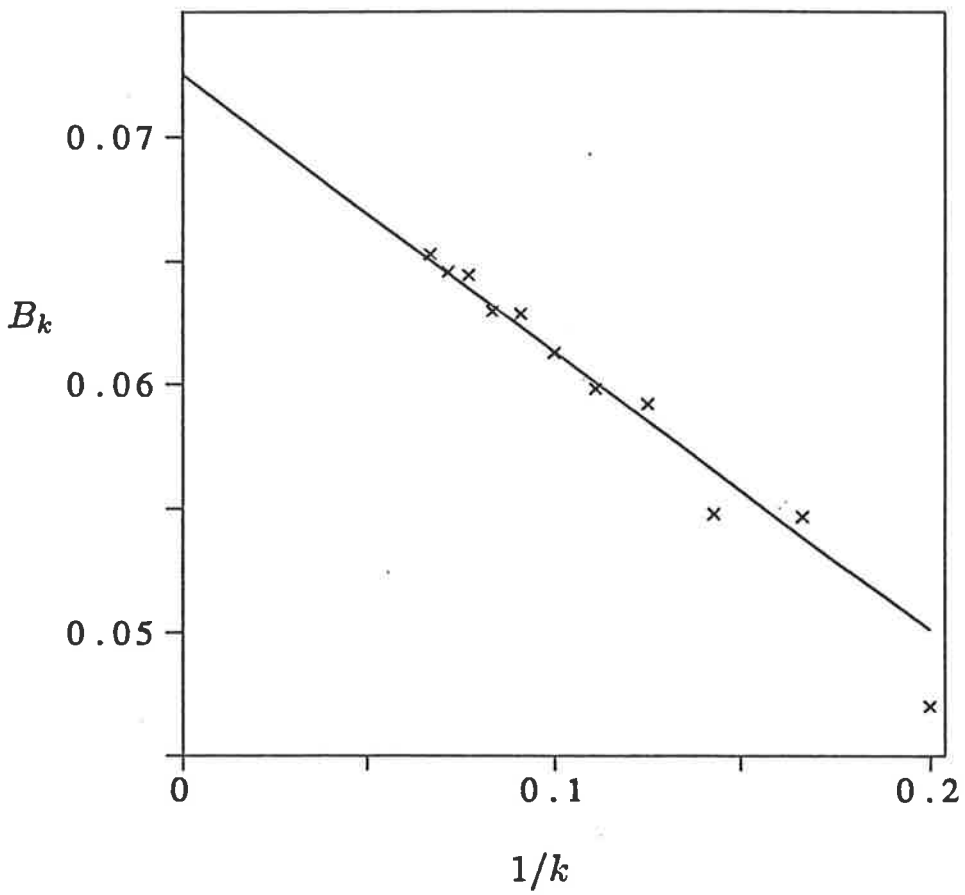

Figure 7.2a: Generalised Domb–Sykes plot to estimate the radius of convergence for pipe flow.

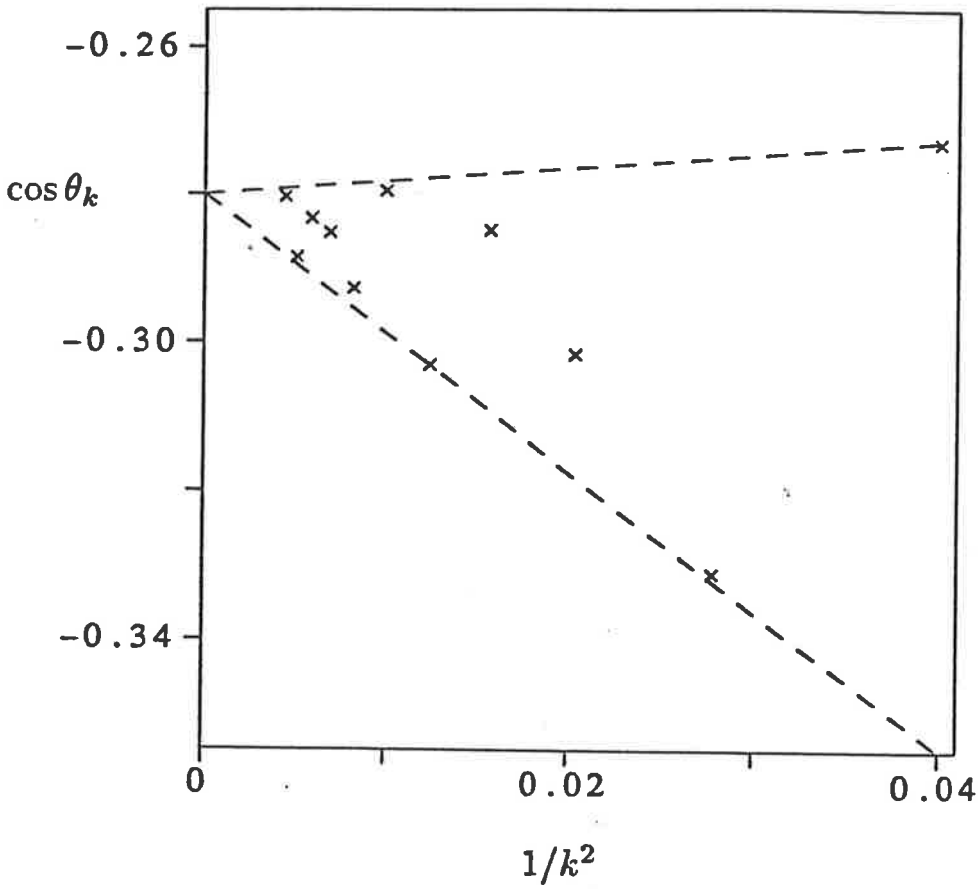

Figure 7.2b: Generalised Domb–Sykes plot to estimate the cosine of the angle from the real axis for pipe flow.

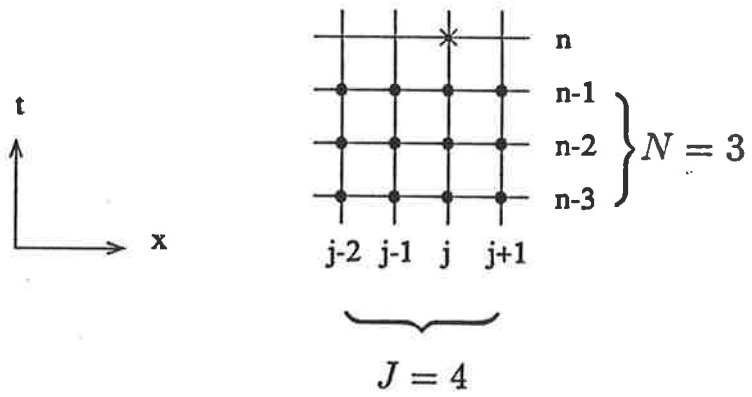

Figure 7.3: Schematic diagram of the finite difference grid using 3 time levels ($N = 3$) and 4 spatial points ($J = 4$), 2 upstream ($K = 2$) and 1 downstream ($L = 1$) of the current spatial position ($\times$).

(a)

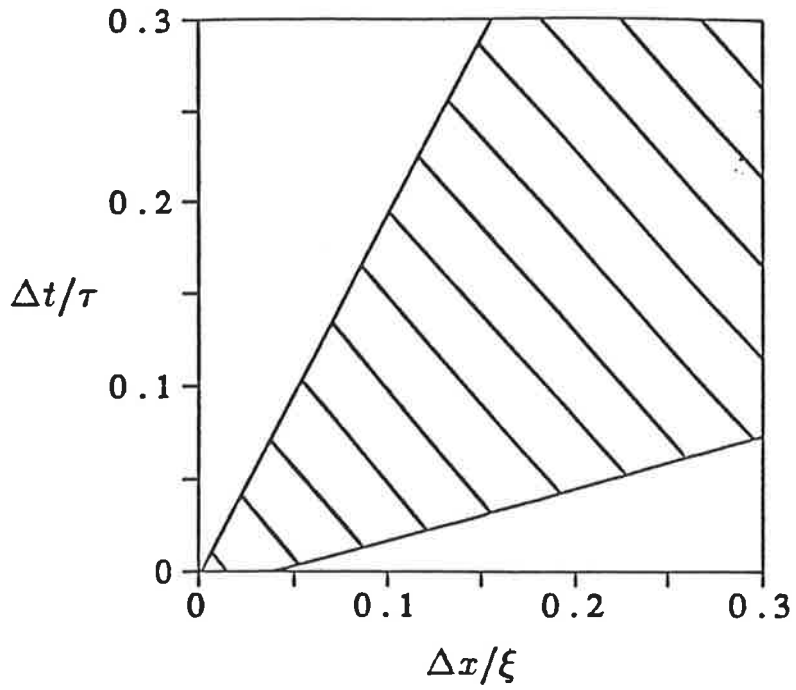

(b)

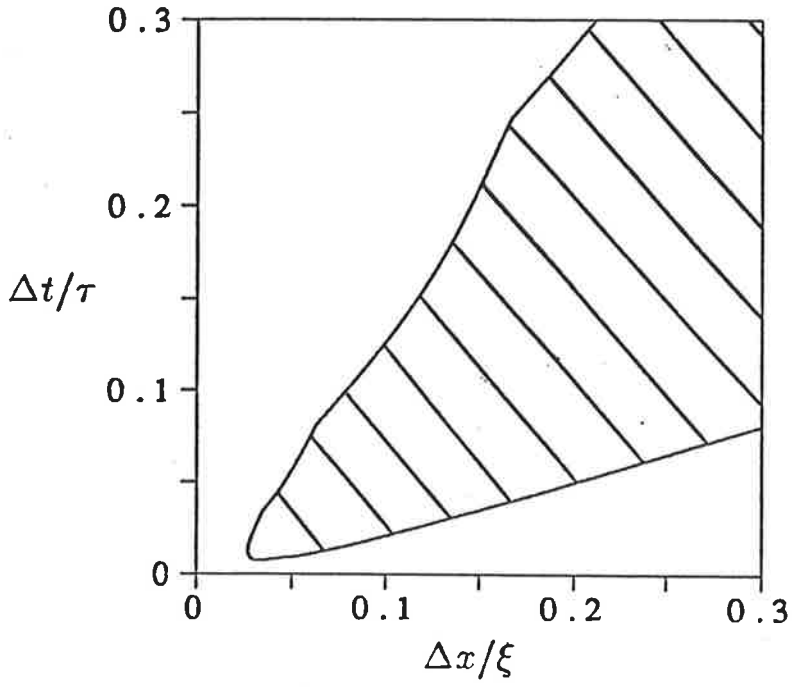

Figure 7.4: (a)–(d) Feasible regions in $(\Delta x/\xi, \Delta t/\tau)$ space for order 2, 3, 4 and 5 methods respectively for the example given in Figure 7.3 with $J = 4$ and $N = 3$.

(c)

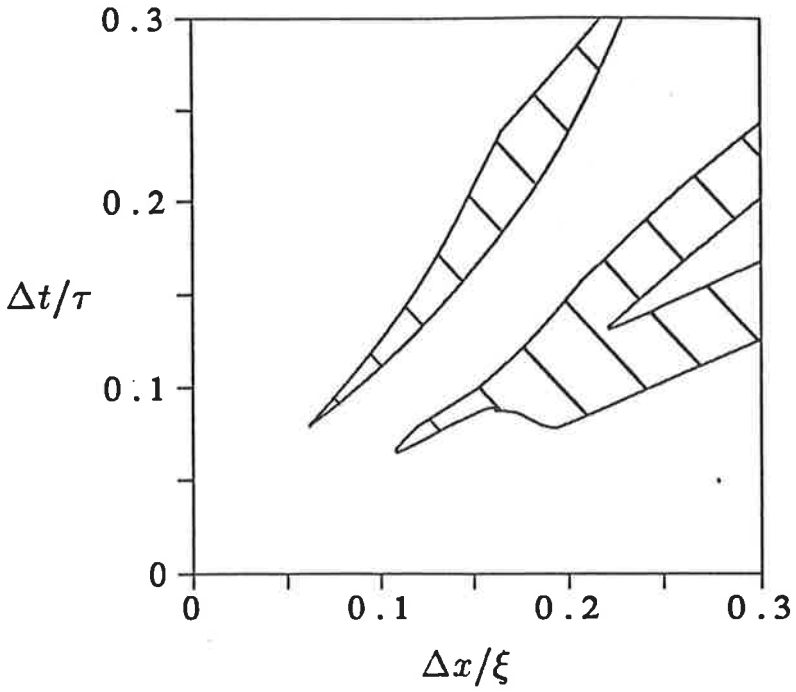
0.3
0.2
$\Delta t/\tau$
0.1
0
0
0.1
0.2
0.3
$\Delta x/\xi$

(d)

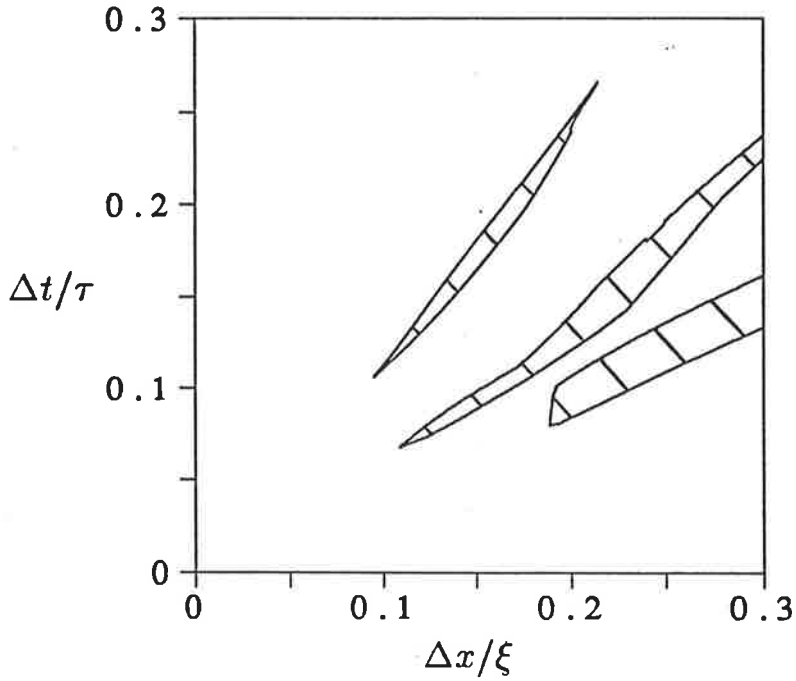
0.3
0.2
$\Delta t/\tau$
0.1
0
0
0.1
0.2
0.3
$\Delta x/\xi$

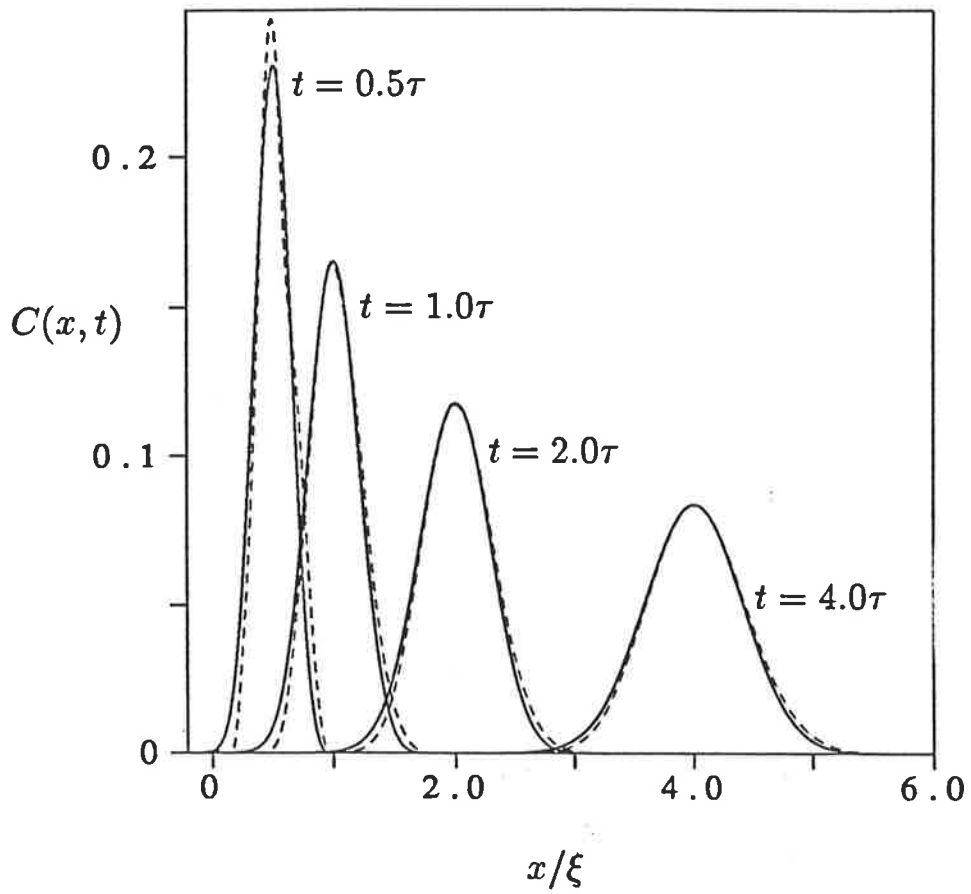

Figure 7.5: Mean concentration profile for order 2 (Taylor) (———) and order 5 (- - - - -) truncations to the evolution equation at $t = 0.5\tau$, 1.0τ, 2.0τ, 4.0τ.

(a)

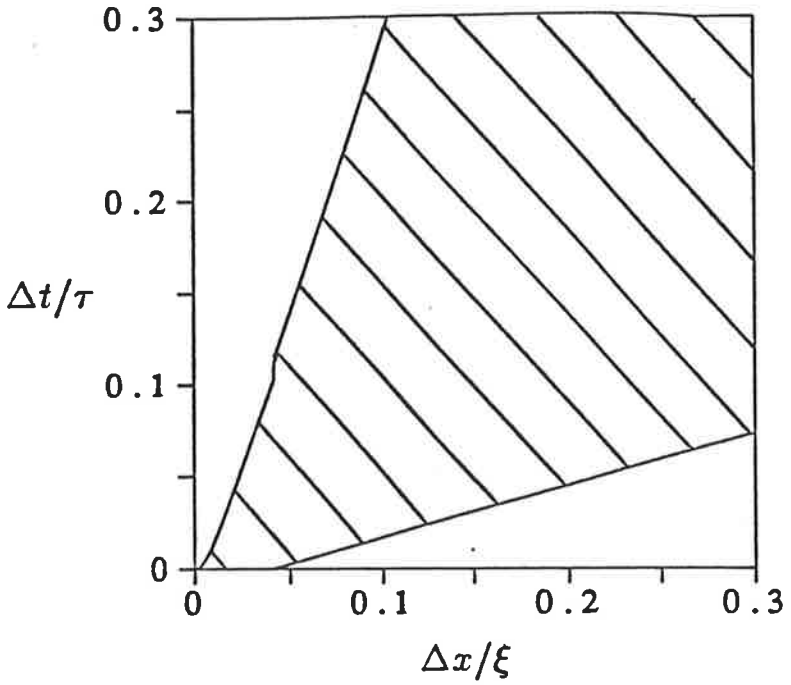

(b)

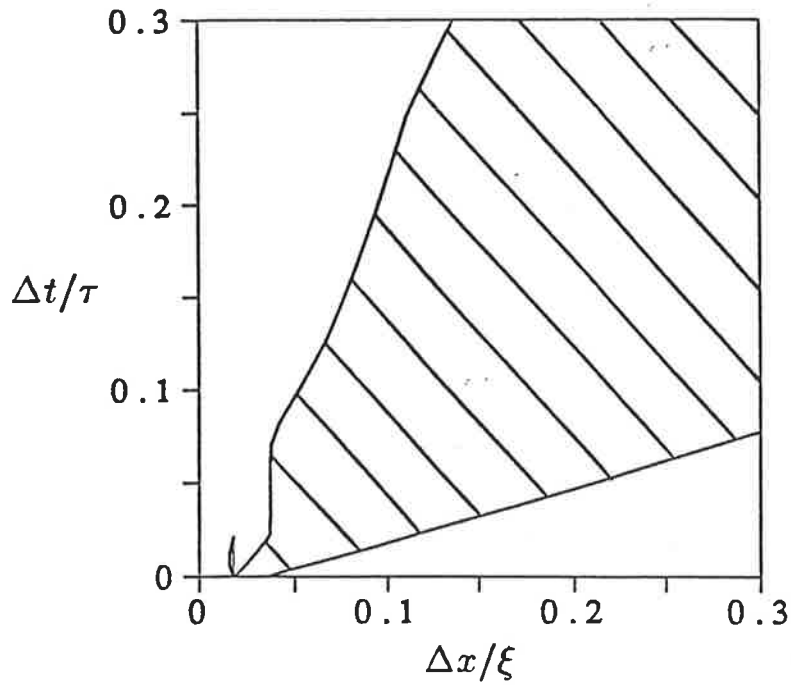

Figure 7.6: (a)-(d) Feasible regions in $(\Delta x/\xi, \Delta t/\tau)$ space for order 2, 3, 4 and 5 methods respectively for $J = 6$ and $N = 3$.

(c)

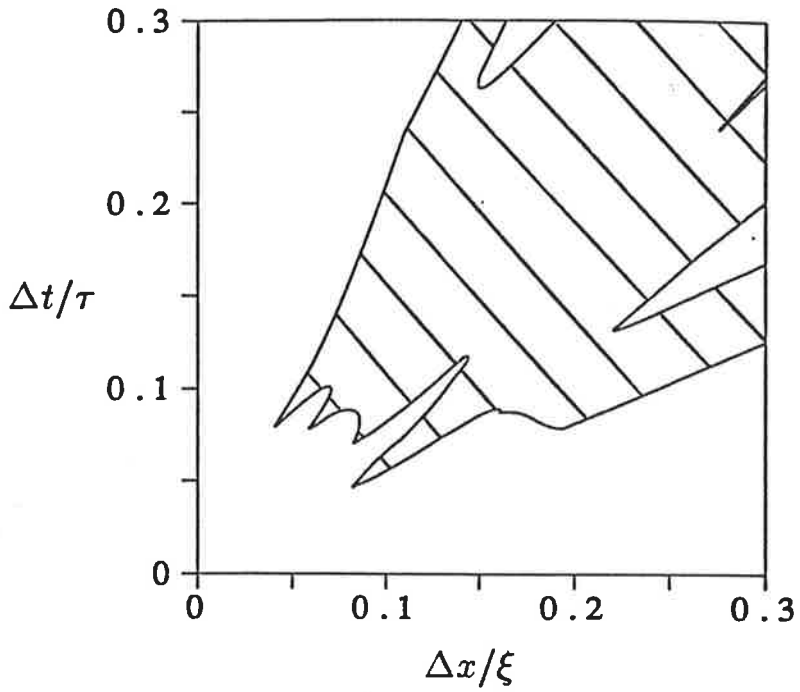
0.3
0.2
0.1
0
$\Delta t/\tau$
0
0.1
0.2
0.3
$\Delta x/\xi$

(d)

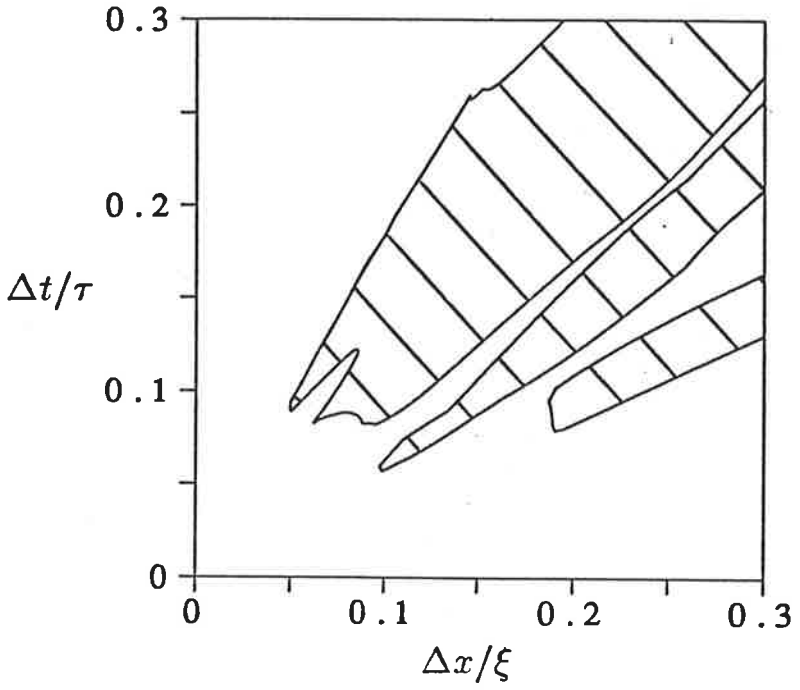
0.3
0.2
0.1
0
$\Delta t/\tau$
0
0.1
0.2
0.3
$\Delta x/\xi$

BIBLIOGRAPHY

Amick C.J. and Toland J.F., 1987 "The semi-analytic theory of standing waves", *Proc. Roy. Soc. Lond.*, **A 411**, 123-137.

Aoki H., 1980 "Higher order calculation of finite periodic standing waves by means of a computer", *J. Phys. Soc. Japan*, **49**, 1598-1606.

Aris R., 1956 "On the dispersion of a solute in a fluid flowing through a tube", *Proc. Roy. Soc. Lond.*, **A 235**, 67-77.

Armbruster D., Guckenheimer J. and Holmes P., 1989 "Kuramoto–Sivashinsky dynamics on the center-unstable manifold", *SIAM J. Appl. Math.*, **49**, 676-691.

Baker, G.R., Merion, D.I. and Orszag, S.A., 1982 "Generalised vortex methods for free surface flow problems", *J. Fluid Mech.*, **123**, 477-501.

Bender C.M. and Orszag S.A., 1978 *Advanced Mathematical Methods for Scientists and Engineers* (McGraw-Hill, New York).

Carr J., 1981 *Applications of centre manifold theory,* Applied Mathematical Sciences, **35**, Springer-Verlag.

Carr J. and Muncaster R.G., 1983 "The application of centre manifolds to amplitude expansions. II. Infinite dimensional problems", *J. Differential Equations*, **50**, 280-288.

Chang H.C. and Chen L.H., 1986 "Growth of a gas bubble in a viscous fluid", *Phys. Fluids*, **29**, 3530-3536.

Chang H.C., 1989 "Onset of nonlinear waves on a falling film", *Phys. Fluids A*, **1**, 1314-1327.

Chatwin P.C., 1970 "The approach to normality of the concentration distribution of a solute in a solvent flowing along a straight pipe", *J. Fluid Mech.*, **43**, 321-352.

Chatwin P.C., 1980 "Presentation of longitudinal dispersion data", *J. Hydraul. Div. Proc. ASCE*, **106**, 71-83.

Chatwin P.C. and Allen C.M., 1985 "Mathematical models of dispersion in rivers and estuaries", *Ann. Rev. Fluid Mech.*, **17**, 119-149.

Chen B. and Saffman P.G., 1979 "Steady gravity-capillary waves on deep water – I. Weakly nonlinear waves", *Stud. Appl. Maths.*, **60**, 183-210.

Chikwendu S.C., 1986 "Application of a slow–zone model to contaminant dispersion in laminar shear flows" *Int. J. Engng. Sci.*, **24**, No. 6, 1031-1044.

Chossat P. and Iooss G., 1985 "Primary and secondary bifurcation in the Couette-Taylor problem", *Jap. J. Appl. Math.*, **2**, 37-68.

Cokelet E.D., 1977 "Steep gravity waves in water of arbitrary uniform depth", *Phil. Trans. R. Soc. Lond.*, **A 286**, 183-230.

Concus P., 1962 "Standing capillary-gravity waves of finite amplitude", *J. Fluid Mech.*, **14**, 568-576.

Concus P., 1964 "Standing capillary-gravity waves of finite amplitude: Corrigendum", *J. Fluid Mech.*, **19**, 264-266.

Crawford D.R., Lake B.M., Saffman P.G. and Yuen H.C., 1981 "Stability of weakly nonlinear deep-water waves in two and three dimensions" *J. Fluid Mech.*, **105**, 177-191.

Davidson T.E., 1990 "Numerical simulation of the water waves generated by a floating body", Ph.D. thesis, University of Adelaide.

De Gance A.E. and Johns L.E., 1978 "The theory of chemically active solutes in a rectilinear flow field", *Appl. Sci. Res.*, **34**, 189-225.

Foias C., Nicolaenko B., Sell G.R. and Temam R., 1985 "Inertial manifolds for the Kuramoto-Sivashinsky", *Comptus Rendus Serie I.*, **301**, 285-288.

Foias C., Nicolaenko B., Sell G.R. and Temam R., 1988 "Inertial manifolds for the Kuramoto-Sivashinsky equation and an estimate of their lowest dimension", *J. Maths. Pures et Appl.*, **67**, 197-226.

Frankel I. and Brenner H., 1989 "On the foundations of generalised Taylor dispersion theory", *J. Fluid Mech.*, **204**, 97-119.

Gill W.N. and Sankarasubramanian R., 1970 "Exact analysis of unsteady convective diffusion", *Proc. Roy. Soc. Lond.*, **A 316**, 341-350.

Gill W.N. and Sankarasubramanian R., 1971 "Dispersion of a non-uniform slug in time-dependent flow", *Proc. Roy. Soc. Lond.*, **A 322**, 101-117.

Goda Y., 1967 "The fourth order approximation to the pressure of standing waves", *Coast. Engng. in Japan*, **10**, 1-11.

Gupta V.K. and Bhattacharya R.N., 1983 "A new derivation of the Taylor-Aris theory of solute dispersion in a capillary", *Water Resources Res.*, **19**, 945-951.

Hwang S.H. and Chang H.C., 1989 "Non-Boussinesq effects on transitions in Hele-Shaw convection", *Phys. Fluids A*, **1**, 924-937.

Kharif C. and Ramamonjiarisoa A., 1988 "Deep water gravity wave instabilities at large steepness", *Phys Fluids*, **31**, 1286-1288.

Kharif C. and Ramamonjiarisoa A., 1990 "On the stability of gravity waves on deep water", *J. Fluid Mech.*, **218**, 163-170.

Laure P. and Demay Y., 1988 "Symbolic computation and equation on the center manifold: application to the Couette-Taylor problem", *Computers and Fluids*, **16**, 229-238.

Longuet-Higgins M.S. and Cokelet E.D., 1976 "The deformation of steep surface waves on water. I. A numerical method of computation.", *Proc. Roy. Soc. Lond.*, **A 350**, 1-26.

Longuet-Higgins M.S., 1978a "The instabilities of gravity waves of finite amplitude in deep water. I. Superharmonics.", *Proc. Roy. Soc. Lond.*, **A 360**, 471-488.

Longuet-Higgins M.S., 1978b "The instabilities of gravity waves of finite amplitude in deep water. II. Subharmonics.", *Proc. Roy. Soc. Lond.*, **A 360**, 489-505.

MacKay R.S. and Saffman P.G., 1986 "Stability of water waves", *Proc. Roy. Soc. Lond.*, **A 406**, 115-125.

Marchant T.R. and Roberts A.J., 1987 "Properties of short-crested waves in water of finite depth", *J. Austral. Math. Soc.*, **B 29**, 103-125.

Marchant T.R., 1988 Personal Communication

McLean J.W., 1982 " Instabilities of finite-amplitude water waves", *J. Fluid Mech.*, **114**, 315-330.

Mercer G.N. and Roberts A.J., 1990 "A centre manifold description of contaminant dispersion in channels with varying flow properties", *SIAM J. Appl. Math.*, **50**, 1547-1565.

Mercer G.N. and Roberts A.J., 1992a "Standing waves in deep water: their stability and extreme form", *Phys. Fluids A*, **4**, 259-269.

Mercer G.N. and Roberts A.J., 1992b "The high order evolution equation for contaminant dispersion in pipes and a corresponding finite difference scheme", in Computational Techniques and Applications : CTAC-91, eds B.J. Noye, B. Benjamin and L. Colgan (in press).

Mercer G.N. and Roberts A.J., 1992c "A complete model of shear dispersion in pipes", *Phys. Fluids A*, submitted.

Mielke A., 1988 "Saint-Venant's problem and semi-inverse solutions in nonlinear elasticity",*Arch. Rat. Mech. Anal.*, **102**, 205-229.

Mielke A., 1991 *Hamiltonian and Lagrangian flows on center manifolds*, Lecture Notes in Mathematics 1489, (Springer-Verlag, Berlin).

Oats D.I. and Roberts A.J., 1992 "Modelling the dynamics of the Kuramoto-Sivashinsky equation – an invariant manifold approach", preprint.

Okamura M., 1984 "Instabilities of weakly nonlinear standing gravity waves", *J. Phys. Soc. Japan*, **53**, 3788-3796.

Pagitsas M., Nadim A. and Brenner H., 1986 "Multiple time scale analysis of macrotransport processes", *Physica*, **135A**, 533-550.

Penny W.G. and Price A.T., 1952 "Finite periodic stationary gravity waves in a perfect fluid, Part 2", *Phil. Trans. Roy. Soc. London*, **A 244**, 254-284.

Powell M.J.D., 1972 *A FORTRAN program for non-linear systems of equations*, in Numerical Methods for Non-linear Algebraic Equations P. Rabinowitz ed.

Pullin D.I., 1982 " Numerical studies of surface-tension effects in nonlinear Kelvin-Helmholtz and Rayleigh-Taylor instability", *J. Fluid Mech.*, **119**, 507-532.

Rayleigh, J.W.S., 1915 "Deep water waves, progressive or stationary, to the third order of approximation", *Proc. Roy. Soc. Lond.*, **A 91**, 345-353.

Renardy Y., 1989 "Weakly nonlinear behaviour of periodic disturbances in two-layer Couette-Poiseuille flow", *Phys. Fluids A*, **1**, 1666-1676.

Roberts A.J., 1981 "The behaviour of harmonic resonant steady solutions to a model differential equation", *Q. J. Mech. Appl. Math.*, **34**, 287-310.

Roberts A.J., 1983a "A stable and accurate numerical method to calculate the motion of a sharp interface between fluids", *IMA Journal of Applied Mathematics*, **31**, 13-35.

Roberts A.J., 1983b "Highly nonlinear short-crested water waves", *J. Fluid Mech.*, **135**, 301-321.

Roberts A.J., 1988 "The application of centre manifold theory to the evolution of systems which vary slowly in space", *J. Aust. Math. Soc. B*, **29**, 480-500.

Roberts A.J., 1989 "Appropriate initial conditions for asymptotic descriptions of the long term evolution of dynamical systems", *J. Aust. Math. Soc. B*, **31**, 48-75.

Roberts A.J., 1991a "Planform selection in convection – an embedded centre manifold", *J. Austral. Math. Soc.*, **B**, to appear.

Roberts A.J., 1991b "Boundary conditions for approximate differential equations", *J Aust. Math. Soc.*, **B**, to appear.

Roberts A.J., 1992 "The invariant manifold of beam deformations. Part 1. the simple circular rod", *J. Elasticity*, to appear.

Rottman J.W., 1982 "Steep standing waves at a fluid interface", *J. Fluid Mech.*, **124**, 283-306.

Saffman P.G. and Yuen H.C., 1979 "A note on numerical computations of large amplitude standing waves", *J. Fluid Mech.*, **95**, 707-715.

Saffman P.G., 1985 "The superharmonic instabilities of finite-amplitude water waves", *J. Fluid Mech.*, **159**, 169-174.

Schwartz L.W. and Whitney A.K., 1981 "A semi-analytic solution for non-linear standing waves in deep water", *J. Fluid Mech.*, **107**, 147-171.

Smith R., 1981 "A delay-diffusion description for contaminant dispersion", *J. Fluid Mech.*, **105**, 469-486.

Smith R., 1983 "Longitudinal dispersion coefficients for varying channels", *J. Fluid Mech.*, **130**, 299-314.

Smith R., 1987 "Diffusion in shear flows made easy: the Taylor limit", *J. Fluid Mech.*, **175**, 201-214.

Smith R., 1988 "Entry and exit conditions for flow reactors", *IMA J. of Appl. Maths*, **41**, 1-40.

Stokes A.N. and Barton N.G., 1990 "The concentration distribution produced by shear dispersion of solute in Poiseuille flow", *J. Fluid Mech.*, **210**, 201-221.

Tabjbakhsh I. and Keller J.B., 1960 "Standing surface waves of finite amplitude", *J. Fluid Mech.*, **8**, 442-451.

Tanaka M., 1985 "The stability of steep gravity waves. Part 2", *J. Fluid Mech.*, **156**, 281-289.

Taylor G.I., 1953a "An experimental study of standing waves", *Proc. Roy. Soc. Lond.*, **A 218**, 44-59.

Taylor G.I., 1953b "Dispersion of soluble matter in a solvent flowing through a tube", *Proc. Roy. Soc Lond.*, **A 219**, 186-203.

Taylor G.I., 1954 "Conditions under which dispersion of a solute in a stream of solvent can be used to measure molecular diffusion", *Proc. Roy. Soc Lond.*, **A 225**, 473-477.

Tsai W-T. and Yue D.K.P., 1987 "Numerical calculation of nonlinear axisymmetric standing waves in a circular basin", *Phys. Fluids*, **30**, 3441-3447.

Tsai W-T., Yue D.K.P. and Yip K.M.K., 1990 "Resonantly excited regular and chaotic motions in a rectangular wave tank", *J. Fluid Mech.*, **216**, 343-380.

Vanden-Broeck J.-M. and Schwartz L.W., 1981 "Numerical calculation of standing waves in water of arbitrary uniform depth", *Phys. Fluids*, **24**, 812-815.

Vinge T. and Brevig P., 1981 "Breaking waves on finite water depths: a numerical study", The Ship Research Institute of Norway, Report R-111.81.

Virnig J.C., Berman A.S. and Sethna P.R., 1988 "On three–dimensional nonlinear subharmonic resonant surface waves in a fluid: Part II – experiment", *J. Appl. Mech.*, **55**, 220-224.

Young W.R. and Jones S., 1991 "Shear Dispersion", *Phys. Fluids A*, **3** 1087-1101.

Zakharov V.E., 1968 "Stability of periodic waves of finite amplitude on the surface of a deep fluid.", *Zh. Prikl. Mekh. Fiz.*, **2**, 86, (Translated in *J. Appl. Mech. Tech. Phys.*, **2**, 190-194).